**Synthesis and Study of Physical and Photocatalytic Properties of
Silver Chloride of Different Morphologies**

Hasan Daupor

**A Thesis Submitted in Partial Fulfillment of the Requirement for the
Degree of Doctor of Philosophy in Chemistry
Prince of Songkla University
2015**

Thesis Title   Synthesis and Study of Physical and Photocatalytic Properties of Silver Chloride of Different Morphologies

Author   Mr. Hasan Daupor

Major Program   Chemistry

Major Advisor :

....
(Assoc. Prof. Dr. Sumpun Wongnawa)

Examining Committee :

....Chairperson
(Assoc. Prof. Dr. Apisit Songsasen)

....Committee
(Assoc. Prof. Dr. Sumpun Wongnawa)

....Committee
(Assoc. Prof. Dr. Sumetha Suwanboon)

....Committee
(Asst. Prof. Dr. Pongsaton Amornpitoksuk)

....Committee
(Dr. Uraiwan Sirimahachai)

The Graduate School, Prince of Songkla University, has approved this thesis as partial fulfillment of the requirements for the Doctor of Philosophy Degree in Chemistry

....
(Assoc. Prof. Dr. Teerapol Srichana)
Dean of Graduate School

This is to certify that the work here submitted is the result of the candidate's own investigations. Due acknowledgment has been made of any assistance received.

....Signature

(Assoc. Prof. Dr. Sumpun Wongnawa)

Major Advisor

....Signature

(Mr. Hasan Daupor)

Candidate

I hereby certify that this work has not been accepted in substance for any degree, and is not being currently submitted in candidature for any degree.

....Signature

(Mr. Hasan Daupor)

Candidate

ชื่อวิทยานิพนธ์	การสังเคราะห์ การศึกษาสมบัติทางกายภาพ และโฟโตคะตะลิสต์ของซิลเวอร์คลอไรด์ที่รูปร่างแตกต่างกัน
ผู้เขียน	นายฮาซัน ดอปอ
สาขาวิชา	เคมี
ปีการศึกษา	2557

บทคัดย่อ

ได้ทำการสังเคราะห์สารประกอบซิลเวอร์คลอไรด์ (Silver chloride, AgCl) โดยวิธีการแลกเปลี่ยนไอออนแบบดัดแปลง 2 วิธีที่ ส่งผลให้เกิดรูปร่างที่แตกต่างกัน คือ urchinlike ซึ่งได้จากการใช้สารไทเทเนียมเตตระคลอไรด์ (Titanium tetrachloride, $TiCl_4$) และซิลเวอร์ไนเตรต (Silver nitrate, $AgNO_3$) เป็นสารตั้งต้น แต่เมื่อเปลี่ยนมาใช้สารอลูมิเนียมคลอไรด์ (Aluminium chloride, $AlCl_3$) เป็นสารตั้งต้น ร่วมกับสารไวนิลอะซิเตทมอนอเมอร์ (Vinyl acetate monomer, VAM) เป็นสารควบคุม จะเกิดรูปร่างที่หลากหลายได้ดังนี้ concave cube, octapods, Rubik's cube, flower-like, octahedron, hexapods with sharp tips, hexapods with square tips, hexapods with dagger-like pods, flower-like of zeolite shape โดยสารประกอบซิลเวอร์คลอไรด์ที่สังเคราะห์ได้จาก 2 วิธีนี้ จะมีส่วนของโลหะเงิน (metallic Ag, Ag^0) เกิดขึ้นจากการที่ไอออนเงิน (Silver ion, Ag^+) บางส่วนถูกรีดิวซ์ด้วยความร้อนที่เกิดขึ้นในกระบวนการสังเคราะห์ โดยไม่ได้ใช้สารรีดิวซ์ใด ๆ ซึ่งจะเรียกว่า "Ag/AgCl" รายละเอียดต่าง ๆ กล่าวโดยสรุปได้ดังนี้

ในการสังเคราะห์สารประกอบ Ag/AgCl ที่มีรูปร่างแบบ urchinlike นั้น ก่อนที่จะมีตะกอนของ AgCl เกิดขึ้น จะมีสารประกอบไทเทเนียมไดออกไซด์ (Titanium dioxide, TiO_2 อสัณฐาน (amorphous phase) และ/หรือรูไทล์ (rutile phase) เกิดขึ้นด้วย เนื่องจากเป็นการทำปฏิกิริยาไฮโดรไลซีสที่รุนแรง ของสารตั้งต้นไทเทเนียมเตตระคลอไรด์ จึงส่งผลให้พื้นผิวของอนุภาค AgCl เกิดผลึกลักษณะเหมือนเส้นขน ขนาดนาโนเมตร (nanohairs) สามารถมองเห็นได้ชัดเจนภายใต้กล้องจุลทรรศน์อิเล็กตรอนแบบส่องผ่าน (TEM) ลักษณะรูปร่างที่เป็นขนรอบ ๆ ผิวอนุภาคนี้ จึงถูกจัดไว้ในสารประกอบที่มีรูปร่างคล้ายหอยเม่น หรือ urchinlike Ag/AgCl

สำหรับการสังเคราะห์สารประกอบ Ag/AgCl ให้เกิดเป็นรูปร่างแบบ flower-like นั้น ได้พิสูจน์โดยการทดลองว่า flower-like Ag/AgCl นั้น เกิดขึ้นจาก cubic seeds ที่มีการโตในทิศทาง ⟨111⟩ มากกว่าทิศทาง ⟨110⟩ และไม่สามารถโตไปในทิศทาง ⟨100⟩ เนื่องจากมีสารควบคุม VAM เกิดพันธะกับ Ag^+ อยู่ จึงเกิดเป็นรูปร่าง concave cube, Rubik's cube และ

flower-like โดยอัตราส่วนความเข้มของกราฟ XRD ของระนาบ (111) เทียบกับระนาบ (220) มีค่าสูงขึ้นตามลำดับ เมื่อทำการศึกษาความเข้มข้นของสาร VAM, CH$_3$COOH และอุณหภูมิใน การสังเคราะห์ ที่มีผลต่อการเกิดรูปร่างพบว่า รูปร่างจะเปลี่ยนไปจากเดิม ดังนี้ hexapod with sharp tips ได้เกิดขึ้นมาจาก octahedral seed สังเกตได้จากปลายของแท่งมีความแหลมคม เหมือนมุมของรูปทรง octahedron ที่ได้ยื่นออกมา โดยการโตไปในทิศทาง ⟨100⟩ ของ octahedral seed เช่นเดียวกับ hexapod with dagger-like pods แต่ในทางตรงกันข้าม hexapod with square pod จะเกิดจากการโตของ cubic seed ไปในทิศทาง ⟨100⟩ เนื่องจาก สังเกตเห็นว่าลักษณะของปลายแต่ละแท่งนั้น ไม่เรียวแหลมแต่จะเป็นหน้าสี่เหลี่ยมแบน ซึ่งเป็น ลักษณะของด้านทั้งหกของ cubic seed

โลหะเงิน (Ag^0) ที่ได้ตรวจพบด้วยเครื่อง XPS ในสารประกอบ Ag/AgCl จะ ช่วยในการดูดกลืนแสงวิสิเบิล และเมื่อนำไปศึกษาประสิทธิภาพในการสลายสีย้อม orange G ด้วยแสงยูวีและวิสิเบิล พบว่า ทั้ง urchin-like Ag/AgCl และ flower-like Ag/AgCl สามารถสลาย สีย้อมได้ดีกว่า commercial AgCl, simple AgCl และ Degussa P25 อีกทั้งยังสามารถนำ กลับมาใช้งานซ้ำได้อีกประมาณ 3-4 ครั้ง โดยไม่ต้องผ่านการฟื้นฟูใหม่ (regeneration) และ พฤติกรรมในการสลายสีนั้นจะเป็นไปตามปฏิกิริยาอันดับหนึ่งเทียม (pseudo-first order kinetic)

Thesis Title   Synthesis and Study of Physical and Photocatalytic Properties of Silver Chloride of Different Morphologies

Author   Mr. Hasan Daupor

Major Program   Chemistry

Academic Year   2014

Abstract

In this work, AgCl particles were synthesized from two different methods of modified ion-exchange reaction. First, an urchinlike Ag/AgCl was obtained by using $TiCl_4$ and $AgNO_3$ as starting materials. In the second method, replacement of chloride source by $AlCl_3$ together with controlling the morphology by VAM produced AgCl of various morphologies: concave cube, octapod, Rubik's cube, flower-like, octahedron, hexapod with sharp tips, hexapod with square tips, hexapod with dagger-like pod, flower-like of zeolite shape. AgCl synthesized from both methods had metallic Ag on its surface resulting from partial Ag^+ ions being reduced by heating in the synthesis process without using any reducing agents. AgCl mixed with metallic Ag is often designated as "Ag/AgCl". The details of syntheses are given as follows.

In the synthesis of urchinlike Ag/AgCl, before precipitation of AgCl, amorphous and rutile TiO_2 were also obtained because of the forced hydrolysis of $TiCl_4$ precursor. The drastic hydrolysis reaction might affect the growth of nanohairs on the AgCl surface which can be seen clearly from TEM images. The near spherical kernel covered with countless tiny hairs was classified into the urchinlike group of nanostructure shapes.

For the synthesis of flower-like Ag/AgCl, it was envisaged that starting from cubic seed the growth along the $\langle 111 \rangle$ direction was larger than the $\langle 110 \rangle$ direction and the growth of $\{100\}$ facet was blocked by the bonding of oxygen of VAM to Ag^+ ion at the center of this face. As a result, concave cube, Rubik's cube, and flower-like were obtained as evidenced from the orderly increasing XRD peak intensity ratios of $(111)/(220)$. Various synthesis parameters were varied, i.e., the

concentration of CH_3COOH, the amount of VAM, and the reaction temperatures. It was observed that the hexapod with sharp tips and hexapod with dagger-like pod grew from octahedral seed as evidenced from the sharp tips of octahedral vertex that grew along the ⟨100⟩ directions. On the contrary, hexapod with square pods grew from cubic seed along ⟨100⟩ directions which showed the square top facet supporting the growth habit of six cubic {100} facets.

The presence of metallic Ag as detected by XPS enhanced absorption of visible light as shown by the absorption spectra from DRS technique. The photocatalytic activity on orange G dye under UV and visible light irradiation indicated that both urchinlike and flower-like Ag/AgCl were better than commercial AgCl, simple AgCl, and Degussa P25. Moreover, the urchinlike and flower-like Ag/AgCl could be reused around 3-4 times with no need for regeneration. The behavior of this dye degradation followed pseudo-first order kinetic.

Acknowledgements

Hasan Daupor

Contents

Content (cont.)

List of Figures

List of Figures (Cont.)

List of Tables

List of Schemes

List of Publications and Proceedings

Publications

Paper I   **Daupor, H.,** and Wongnawa, S. 2014. Urchinlike Ag/AgCl photocatalyst: Synthesis, characterization, and activity. *Applied Catalysis A: General*, **473**, 59-69.
            Impact Factor (2014): 3.674
            (Reprinted with permission from Elsevier)

Paper II   **Daupor, H.,** Wongnawa, S. 2015. Flower-like Ag/AgCl microcrystals: Synthesis and photocatalytic activity. *Materials Chemistry and Physics*, **xxx**, 1-12.
            Impact Factor (2015): 2.129
            (Reprinted with permission from Elsevier)

Proceedings

Paper I   **Daupor, H.,** Wongnawa, S. Metal ion doped TiO_2: preparation, characterization and photocatalytic study. The Sixth Thailand Material Science and Technology Conference (MSAT 6), Miracle Grand Convention Hotel, Bangkok, Thailand, August 26–27, 2010, 298–300.

Paper II   **Daupor, H.,** Wongnawa, S. Ag/AgCl photocatalytic activity on orange G dye under visible light irradiation. Pure and Applied Chemistry International Conference (PACCON 2014), Centara Hotel and Convention Centre, Khon Kean, Thailand, January 8–10, 2014, 393–396.

1. Introduction

1.1 Background and Rationale

The degradation of the dissolved organic compounds in water using photocatalysis has attracted much attention because it is easy to handle, inexpensive, stable and effective (Fujishima et al., 2000). Many photocatalysts have been attempted for the degradation of pollutants in wastewater. Among the various metal oxides semiconductors, TiO_2 mediated heterogeneous photocatalysis has been shown to be potentially advantageous as it may proceed at ambient conditions and lead to the complete mineralization of many organic pollutants to harmless products of CO_2, H_2O and mineral acids (Konstantinou and Albanis, 2004). TiO_2 is the most preferable material for the photocatalytic process due to its high photosensitivity, non–toxic nature, large band gap and stability (Hoffmann et al., 1995). However, there are still basic problems to be solved for improving the photocatalytic activity of TiO_2. The semiconductor TiO_2 has wide band gap energy (≥ 3.2 eV), it is excited only by UV light ($\lambda < 388$nm) to eject electrons from valence band to conduction band. But UV light constitutes only about 3-5% of the solar spectra. Practically, this factor strongly limits the use of solar spectra as a light source (Logar et al., 2010). In addition, the electron–hole recombination rate is high in TiO_2 particles resulting in a low efficiency of photocatalysis (Devi and Reddy, 2011).

Therefore, this practically limits the use of sunlight or visible light as an irradiation source in photocatalytic reaction on TiO_2. To overcome these limitations of TiO_2 as a photocatalyst, numerous studies have been recently performed to enhance electron-hole separation and to extend the absorption range of TiO_2 into the visible range including doping different metals such as Pt, Pd, Ru, Au, and Ag, so as to efficiently extend photoresponse from UV to visible light (Li and Li, 2002; Qi et al., 2005). The deposition of noble metals on the surface is not only to act as a trap to capture the photoinduced electron and hole leading to the reduction of electron-hole recombination in photocatalytic process but also to increase the absorption ability for visible range due to the surface plasmon resonance (SPR) effect of noble metal (Sakthivel et al., 2004). Some noble metals such as Pt, Pd, Rh, and Au may be too expensive to be useful in wide scale applications. Thus, the research on Ag modified photocatalyst shows more significant practical value. Metal nanomaterials, especially,

Ag and Au nanoparticles (Jakob et al., 2003) have been extensively studied over the past decades due to their unique SPR properties in the visible region which are useful for catalysts, surface plasmonics, surface-enhanced Raman scattering, nonlinear optics, chemical and biological sensing, and cancer therapies (Noguez, 2007; Ghosh and Pal, 2007). The SPR can dramatically amplify the absorption of visible light which opens up new opportunities for the deployment of photocatalysts for environmental clean-up.

Many physical properties of nanostructure are strongly dependent on morphologies, therefore, synthetic control of the morphology has been an important synthetic magic in the field of materials chemistry to help fine tuning several properties such as electronic, optical, and catalytic properties of semiconductor nanocrystals (El-Sayed, 2001). The intrinsic properties of semiconductor nanostructures can be tailored by controlling their size, shape, composition, crystallinity, and structure. Particular emphasis has recently been placed on the control of shape, because in many cases it allows one to fine tune the properties with a greater versatility than can be achieved otherwise (Westcott et al., 1999). Shape control has been in the limelight recent years in the researches of noble metals and other inorganic materials. The shape also controls the facet and thus surface structure of a metal nanocrystal, as well as the catalytically active sites, such as corners, edges, steps, etc. (Lim and Xia, 2011). Several metals and shapes have been reported thus far, for example, Au spheres (X. Dong et al., 2009), Ag plates (Luo et al., 2011), Pd cubes (Niu et al., 2008), and Ag rods (Jana et al., 2001). In addition to these simple shapes, classes of flower–like or star–shaped structures have also been synthesized, such as, Au star (Hao et al., 2007), nanoflowers of Pd, Pt, and Ag (Xia et al., 2009), and so on. Both SPR effect and morphology of materials are essential to application in heterogeneous catalysis.

Silver chloride (AgCl) is photosensitive material extensively used in photographic films and optical devices. On absorbing a photon, AgCl particle generates an electron and a hole, and subsequently the photogenerated electron combines with an Ag ion to form an Ag metal atom. Ultimately, a cluster of Ag atoms is formed within AgCl particle upon repeated absorption of photons. Due to this instability under sunlight, AgCl is provided the very basis for chemical photography.

Recently, the application in photocatalysis with plasmonic photocatalysts (Ag/AgCl) having stronger absorption and activity under visible light has attracted scientists' attention all over the world and becomes a hotspot in the field of photocatalysis (Lou et al., 2011). A variety of morphologies of AgCl have been reported, for example, Ag/AgCl core–shell nanowires were synthesized from oxidation reaction of Ag nanowires and $FeCl_3$ at room temperature. The oxidation reaction was explained based on the lower redox potential of Fe^{3+} ions than that of Ag species resulting in the migration of electrons from Ag nanowires to Fe^{3+} ions to form the AgCl nanowires. This oxidation process was also attempted with other metal chlorides such as $CuCl_2$ solution to fabricate a novel nanoplate/nanowire Ag/AgCl (Bi and Ye, 2009). Uniform heart-like AgCl was fabricated in the presence of ethylene glycol (EG) and polyvinyl pyrrolidone (PVP) under heating at 140 ℃ for 7 h. Heart-like morphology arose from the merge of four cubes by oriented–attachment (Liao et al., 2012). Ion-exchange reaction between NaCl with Ag_2WO_4 microrods (as the template) produced rod–like morphology of Ag/AgCl with rough surfaces (Chen et al., 2014). Cubic Ag/AgCl (Han et al., 2011) and spherical Ag/AgCl (Lou et al., 2011) are generally synthesized for decomposition of organic pollutants.

Many recent efforts have focused on 3-dimensional structures of AgCl semiconductor materials. Lou and co-workers presented a wet chemical oxidation approach to synthesize AgCl concave cube using $NaClO_2$ as an oxidizer for Ag plate immersed in NaCl solution at room temperature. (NaCl was source of Cl^- ions.) The AgCl concave cube with high-index facets was shown to have higher photocatalytic activity than the cubic with six smooth {001} facets in the decomposition of methyl orange (MO) under visible light irradiation because of the existence of a large number of atomic step, edges, and kinks accompanied to the high-index facets. AgCl concave cube was formed by preferential overgrowth along ⟨111⟩ and ⟨110⟩ directions when the reaction time or NaCl concentration was increased. Interestingly, concave cube grew only along ⟨111⟩ directions with disappearing of {100} facets to form flower-like AgCl at high NaCl concentration (Lou et al., 2012). Furthermore, at even higher concentration of $NaClO_4$, NaCl, and citric acid, 3D AgCl hierarchical superstructure was formed by preferential growth along the ⟨111⟩ directions of cubic seeds (Lou et al., 2012). Up to date, the flower-like octagonal

4

AgCl microstructures with preferential growth along the ⟨111⟩ directions have been synthesized only via the hydrothermal method. Branch-breaking phenomenon of large dendrite crystal, which composed of sub-branch, generated their fragmentation, assembly, dissolution, and recrystallization to form small flower-like octagonal crystals (Li et al., 2013). However, the report of flower-like Ag/AgCl with more exotic and urchinlike Ag/AgCl morphology has not yet appeared.

Most of the researches about Ag/AgCl photocatalyst used the photon energy to reduce some part of Ag ions in AgCl to metallic Ag particles (Peng Wang et al. 2008). On the other hand, there are some reducing agents added during the synthesis process such as ethylene glycol (Jiang and Zhang, 2011a), sodium borohydride (An et al., 2011), ascorbic acid (Ma et al., 2013), to reduce Ag^+ ion to metallic Ag particles also appeared. Polyvinyl pyrolidone (PVP) (Nguyen and Vu, 2012) and polyvinyl alcohol (PVA) (Choi et al., 2010), as controlling agents, were widely used by many researchers but vinyl acetate monomer (VAM), similar to what found with PVP, has not been reported for controlling the AgCl synthesis. In this thesis, we introduced two modified ion–exchange reaction for alternative method to synthesize Ag/AgCl using different reagents from those mentioned above. The first method employed $TiCl_4$ which might have some effect on the growth of nanohairs *via* forced hydrolysis of $TiCl_4$ precursors as found in the work by Wang et al. (Wang et al., 2011) to form an urchinlike Ag/AgCl. In the second method, $AlCl_3$ as a chloride ion source and using vinyl acetate monomer (VAM) acted as controlling agent for preparing the flowerlike Ag/AgCl and its related morphologies including concave cube, Rubik's cube, octahedrons, hexapods, and octapods. The Ag^+ ions of these two methods are prone to easy reduction to Ag^0 under reaction condition. The factors influencing the morphologies of the Ag/AgCl samples and their related mechanisms have been systematically investigated. The photocatalytic performance of the urchinlike and flowerlike Ag/AgCl crystals has been evaluated using orange G dyes as the model substances under UV and visible-light irradiation.

1.2 Objectives

The objectives of this research concentrate on the different morphologies of Ag/AgCl particles which are strongly dependent on many physical properties. The aims of this study referring to the proposal presentation are as follows:

1.2.1 To investigate the effect of additive reagents (VAM in this work) on controlling the morphology.

1.2.2 To characterize the physical properties of the as-prepared Ag/AgCl powders using XRD, XPS, BET, TGA-DSC, SEM-EDS, TEM, and DRS techniques.

1.2.3 To evaluate the photocatalytic activity for orange G degradation of the as-prepared Ag/AgCl compared with commercial AgCl, simple AgCl, and also Degussa P25 TiO_2 catalyst and their recyclability.

1.2.4 To study the optimum conditions for synthesizing Ag/AgCl powder with different morphologies *via* modified ion-exchange reaction**.** The result from this entire work was splitted into two parts each of which has been published as follows.

Paper I. The urchinlike Ag/AgCl and formation process published in *Applied Catalysis A: General.*

Paper II. The flower-like Ag/AgCl and related morphologies including concave cube, Rubik's cube, octapod, hexapod published in *Materials Chemistry and Physics.*

2. Principles and literature reviews

In order to discuss inorganic materials in some details in the later chapters of this thesis it is important to cover the background of crystallography, crystal growth, application of powder X-ray diffraction, AgCl heterogeneous photocatalyst, and so on. All these topics are given below.

2.1 Crystal lattice

Single crystals and crystalline solids are built up of a regularly repeated arrangement of atoms, ions, or molecules in three dimension; this arrangement can be represented the manner of repetition by an array of points, the array being called a **lattice** and the points **lattice points**. A set of lattice points that is repeated by translation and show its full symmetry of the crystal structure is defined as the **unit cell** (Hammond, 1990). **Single crystal materials** comprise a high order of atomic or molecular dimensions or regular geometric periodicity, throughout the entire volume of the material, whereas **polycrystalline material**s comprise an agglomeration of individual microcrystalline unit or **grain**. The regions where neighbouring grains meet or mark the interface between two misaligned portions of the bulk crystal are referred to as **grain boundaries**. Within each grain the atoms are arranged in a regular manner, just like a small crystal, but the orientation of the atomic planes in each grain is different from that in the neighbouring grains. Two-dimensional representations of single crystal and polycrystalline materials are shown in Figure 1a, and 1b, respectively (Neamen, 2003). For example, the Ti–B–N nanocomposite, which consists of nanocrystalline grain about 5 nm in size from high resolution transmission electron microscope (HRTEM), was observed by Lu (Lu et al., 2005), as shown in Figure 1c.

(a)   (b)   (c)
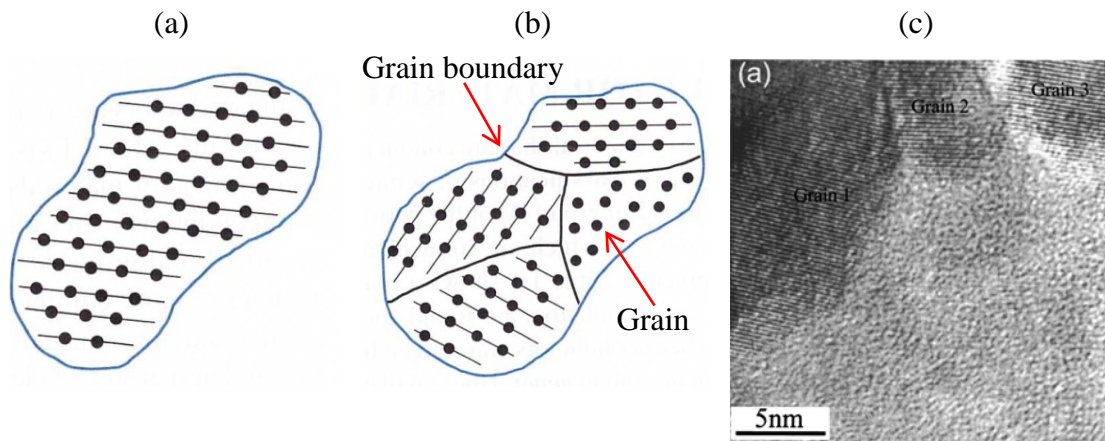
Figure 1 (a) Schematic of single crystal, (b) polycrystalline (Neamen, 2003), and (c) HRTEM image example of the nanocomposite Ti–B–N (Lu et al. 2005).

Seven geometric crystal systems and fourteen unique Bravais lattices, named after the French physicist Auguste Bravais in 1845, describe the position, direction, and structural planes of most crystalline materials. Based on the fourteen Bravais lattice, the different shapes and sizes can be described in terms of three cell edge lengths or axial distances (three lattice constants) as shown in Figure 2a, a, b, c, or lattice vectors a, b, c, and the angle between them, α, β, γ, where α is the angle between b and c, β the angle between a and c, and γ the angle between a and b (Weller, 1994). In the unit cell of AgCl (Figure 2b), face center cubic system (FCC), whole three edges of cell, a, b and c are equal in length and the three angle of the cell α, β and γ are all equal to 90º. AgCl contains Ag^+ ions at the corners and face center positions with Cl^- ions at the edge centers and body center. The value of unit cell content, Z, is 4 i.e. 4 ($Ag^+ Cl^-$) that can be countable as follows (Huheey et al., 1993; Akhmetov and Rosinkin, 1983):

- The eight Ag^+ ions at corners count as 1 atom ($\frac{1}{8} \times 8 = 1$).

- The face center Ag^+ ions have 6 ions countable as $\frac{1}{2}$ each per 1 ion ($\frac{1}{2} \times 6 = 3$) giving a total of 1+3=4 Ag^+ ions.

- For Cl^- ions, there are 12 ions at the edge centers countable as $\frac{1}{4}$ per 1 ion ($\frac{1}{4} \times 12 = 3$).

- The body center has 1 ion, giving a total of 1+3=4 Cl^- ions.

(a)   (b)
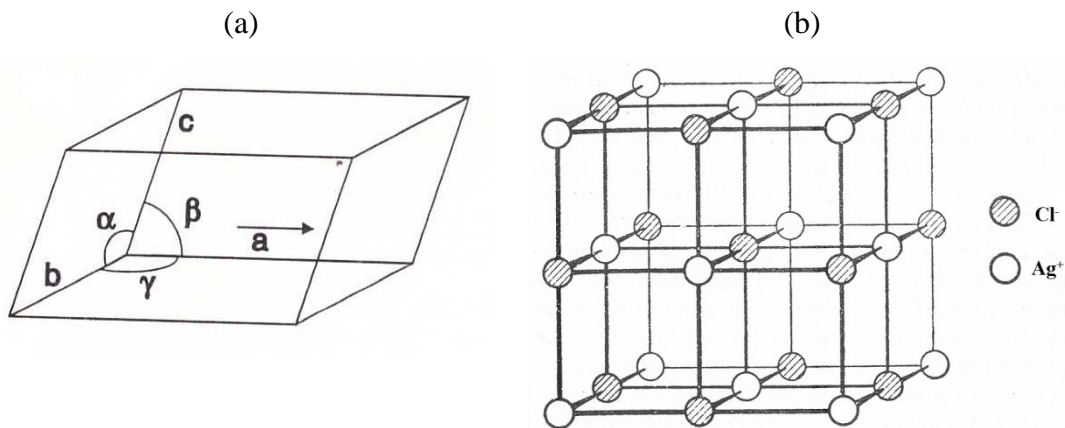
Figure 2 (a) General three-dimensional unit cell definition (Weller, 1994). (b) Face center cubic unit cell of AgCl crystal (Modified from Akhmetov and Rosinkin 1983).

To visualize the face–centered arrangement, consider only the Ag^+ ions or the Cl^- ions (this will require extensions of the sketch of the lattice). There are six Cl^- ions about each Ag^+ ion and six Ag^+ ions about each Cl^- ion. That is 6 coordination number (C.N.) of both ions in the AgCl lattice. So that, most simple ionic compounds with such formulations crystalize as 1:1 with all elements of symmetry found in an octahedron are present (West, 1984).

2.2 Crystal growth

The overall shape or form of a crystal is known as the **morphology**. The external point symmetry of the crystal obviously underlies on the identical unit cell. For example, the crystals grew to form as cubes belonging to the cubic system. However, a crystal from the cubic system may not grow or form with the external shape of a cube; the unit cells may stack up to form, say, an octahedron, or a rhombic dodecahedron as shown in the models constructed from unit cells (Figure 3) (Glusker et al., 1994)
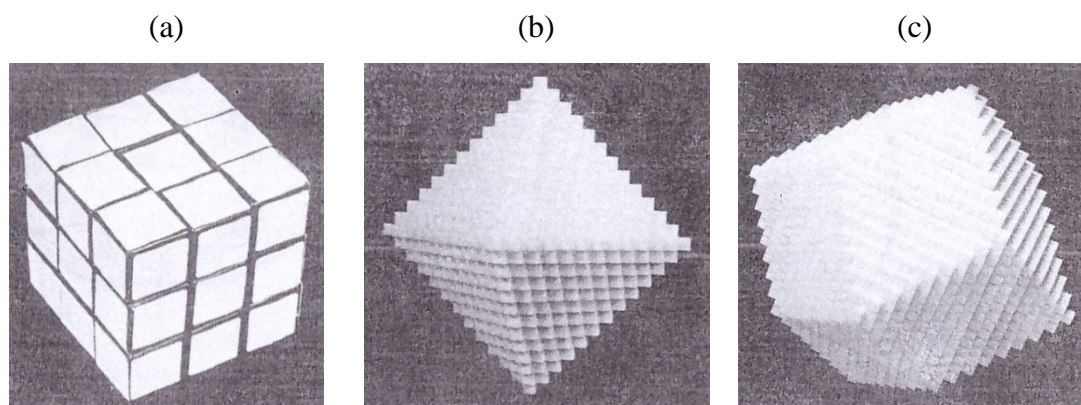
Figure 3 Stacking of cubic unit cell to form (a) a cube, (b) an octahedron and (c) a rhombic dodecahedron. Note that the cubic unit cells in all three models are in the same orientation (Glusker et al., 1994).

2.2.1 Nucleation and growth

Crystal growth involves a phase change from liquid or gas to a solid, such as the precipitation of a solute from solution or the formation of a solid from condensation of a gas. This occurs through two processes: **nucleation** of the product and its subsequent **growth.** In the initial stage of crystallization, that is nucleation, submicroscopic nucleus is formed by several molecules have approached to each other in appropriate orientation and have formed a stable aggregate. After that, the growth process continues to adsorb and align further material on the surface of this nucleus, giving larger particle at the expense of smaller ones sometime according to the **Ostwald ripening** or **coarsening**, and the formation of a crystal was driven by the reduction of surface energy (Zeng, 2006; Cao, 2004).

Some examples of nucleation seed and Ostwald ripening, Kim et al, 2010, studied the growth process of AgCl nanocrystals at 1:2 precursor molar ratio of $AgNO_3$: HCl. The majority of AgCl particles included a number of small nanoparticles with a few percent of large particles as shown in Fig. 4a, and the magnification of the red square part and yellow arrows of Figure 4b, respectively, indicating that, large nanoparticles grow at the expense of small ones. These results clearly showed Ostwald ripening process. In addition, different **nucleation seeds** (between Ag and AgCl seeds) occur at high molar ratio of $AgNO_3$: HCl. AgCl

nanocubes had wide particles size distribution implying that nucleation and growth process are inhomogenous throughout the whole solution (Ohzeki and Hosoya, 2007; Kim et al., 2010).
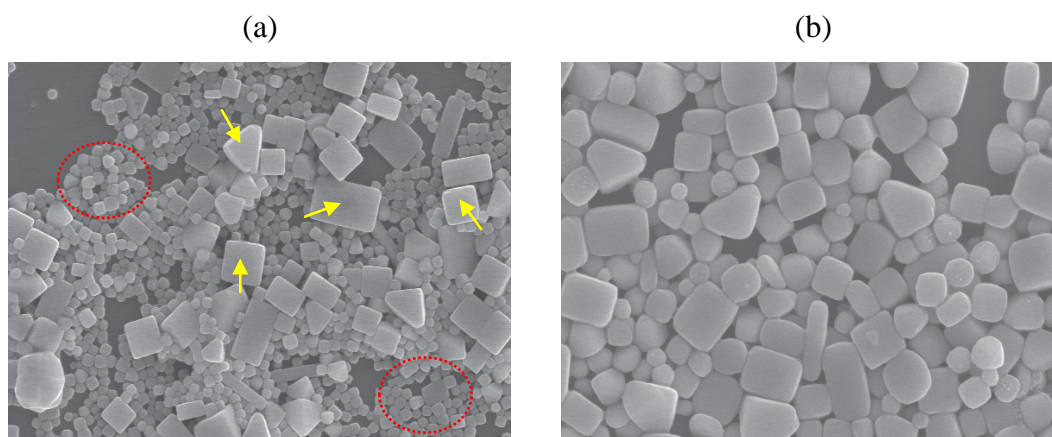
Figure 4 Ostwald ripening process in the nanocubic AgCl synthesis (modified from Kim et al., 2010).

Jiang and Zhang, 2011, synthesized Ag/AgCl by an ion-exchange reaction between aqueous solution of NaCl and AgNO$_3$ in ethylene glycol containing polyvinyl pyrolidone (PVP) under microwave irradiation. In the initial stage, rapid nucleation process produced a large amount of small irregular cubic seed particles whose nuclei grow to form regular nanocubes (step II). After that, the quasi-triangular pyramids Ag/AgCl where surface cracking occurs indicated that cubic crystals attached to each other through oriented attachment. In addition, the partial AgCl was reduced to generate Ag nanograins on their surface (step III). In the last step, the shape of triangular pyramids become rounded through an Ostwald ripening process as shown in Figure 5 (Jiang and Zhang, 2011).
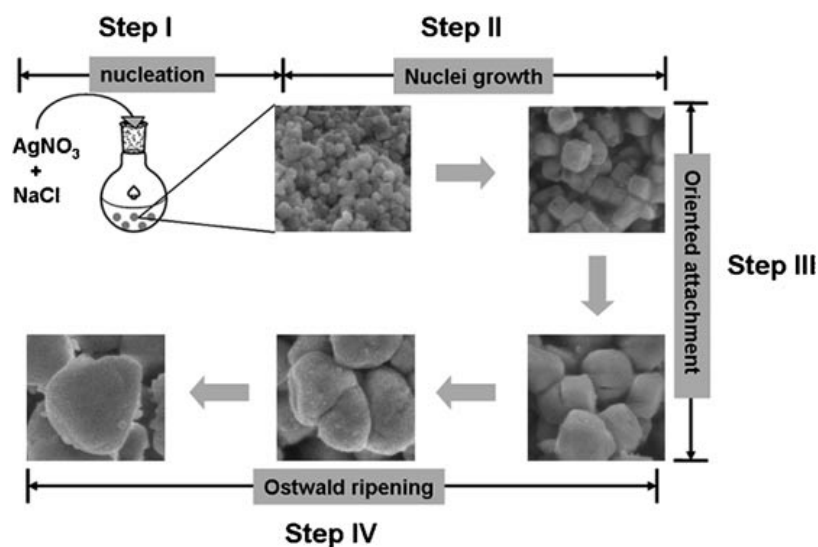
Figure 5 Schematic illustration of the formation process of the Ag/AgCl triangular pyramids (Jiang and Zhang 2011).

Zaizhu Lou et al, 2012, described that the insufficient supply of Ag^+ from Ag plate and stirring related to diffusion rate (V_1) will be decreased. Meanwhile, the excess Cl^- adsorbed on the surface of AgCl cubic seeds, the growth rate (V_2) is driven to be larger than diffusion rate. So, Ag^+ ions added on the sites of AgCl cubic seeds (corners, edges, and sides) are different. Under this system, Ag^+ ions will react to adsorb on the corners and edges of AgCl cubic seeds. Finally, AgCl overgrow along ⟨111⟩ and ⟨110⟩ directions and formed AgCl concave cubes as shown in Figure 6 (Lou et al., 2012; Lou et al., 2013).
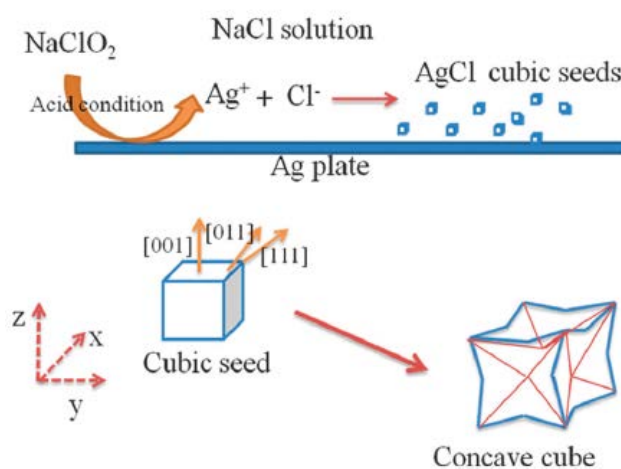
Figure 6 Growth mechanisms of concave cubic AgCl growth along ⟨111⟩ and ⟨110⟩ directions of cubic seed (Lou et al., 2012).

2.2.2 Crystallographic orientation

Crystals are classified as being either **isotropic** or **anisotropic** depending on the equivalency of their crystallographic axes. Anisotropic crystals are composed of a complex crystal lattice orientation that has varying electric properties depending upon the direction of the impinging light ray. As a result, the reflective index will vary with direction when light passes through an isotropic crystal, giving rise to direction-specific trajectories and velocities (Brandon and Kaplan, 1999). Now, we introduce what are essentially shorthand notations for describing directions and planes in crystals.

2.2.2.1 Indexing lattice directions-zone axis symbols

The steps for determining the zone axis symbol for any direction are as follows (West, 1984):

(1) The direction whose symbol is to be determined must pass through the origin of the unit cell.

(2) Write down the co-ordinates of a point-any point-in the interested direction in term of fractions of the length a, b, and c, respectively; the line also passes through $2a, 2b, 2c; 3a, 3b, 3c$, etc.

(3) Arrange the numbers (a, b, c) to be the set of smallest possible integers, by division or multiplication throughout by a common factor and insert them into $[uvw]$ brackets without commas. For example, $\left[\frac{1}{2}\frac{1}{2}0\right]$ are the same directions, but conventionally $[110]$ is used.

(4) Use the bar or minus sign referring to a co-ordinate in the negative sense along to that axis such as $[1\bar{1}0]$ pronounced **"one bar-one oh"**

(5) Group the set of equivalent directions are written with the general symbol $\langle uvw \rangle$.

2.2.2.2 Indexing lattice plane–Miller indices

In 1893 British crystallographer W.H. Miller devised a systematic approach that is related to the geometry of the unit cell. Miller developed a system of describing the orientation of crystallographic planes inside a crystal lattice by a set of

integers that are symbolized by (hkl). The Miller indices came to be useful tools for predicting structural properties of materials. The Miller index algorithm is created by establishing a Cartesian coordinate system, $x, y,$ and z or $a, b,$ and $c,$ and then placing the unit cell at origin $(0,0,0)$. The method for obtaining Miller indices is straightforward (West, 1984):

(1) Set the origin of the unit cell at 000.

(2) Determine the value of intercepts of the crystal plane in terms of lattice constants.

(3) Take the reciprocals of each index and reduce them to the lowest terms.

(4) The three numbers are enclosed in curved brackets, (hkl).

(5) Use the symbol $\{hkl\}$ for indicating the sets of planes that are equivalent. For example, the sets $(100), (010)$ and (001) are equivalent in cubic crystals and may be represented collectively as $\{100\}$.

(6) For the negative axis, the bar signs on the axis planes that are recorded from the opposite side of the origin. For example, the Miller index $\{\bar{2}\bar{1}\bar{1}\}$ pronounced **"bar–two, bar–one, bar–one"**

Actually, when a crystal plane lies parallel to an axis its intercept on that axis is infinity, the reciprocal of which is zero. For example, the face which intersects the x-axis only and is parallel to the y and z-axes, has Miller index (100); the side and the top faces, which intersect the y and z-axes, are (010) and (001), respectively.

2.2.2.3 Zone axis symbols and Miller indices in cubic and octahedral crystals of AgCl

Zone axis symbols and Miller indices may be used to express the symmetry of crystals. This applies to crystals in all the seven systems, but the principles are best explained in relation to cubic crystals because it relates directly with this thesis work. Consider Figure 7a in the cubic system, the exes are crystallographically equivalent and interchangeable, so also are all these six direction symbols. The positive and negative directions of the cubic crystal axes x, y, z can be

14

expressed by three direction symbols as followed (Lou et al. 2013), (Lou, Huang, Qin, et al. 2012):

- The ⟨100⟩ can be expressed by the direction symbols as [100], [$\bar{1}$00], [010], [0$\bar{1}$0], [001], [00$\bar{1}$].

- The diad axis edge-to-edge directions are expressed as ⟨110⟩, of which there are twelve or six pairs of variants. These are [110], [$\bar{1}\bar{1}$0]; [1$\bar{1}$0], [$\bar{1}$10]; [101], [$\bar{1}$01]; [011], [0$\bar{1}$1]; [10$\bar{1}$], [$\bar{1}$0$\bar{1}$], [01$\bar{1}$], [0$\bar{1}\bar{1}$].

- Similarly, the triad axis (corner-to-corner) direction are ⟨111⟩, of which there are four pairs of variants, namely, [111], [$\bar{1}\bar{1}\bar{1}$]; [11$\bar{1}$], [$\bar{1}\bar{1}$1]; [1$\bar{1}$1], [$\bar{1}$1$\bar{1}$]; [1$\bar{1}\bar{1}$], [$\bar{1}$11]

- A similar concept can be applied to Miller indices. With the origin at the center, the six faces of a cube are (100), ($\bar{1}$00), (010), (0$\bar{1}$0), (001), (00$\bar{1}$). These are expressed collectively as planes 'of the form' {100}.

For cubic systems, the [uvw] direction is always perpendicular to the (hkl) plane of the same indices, but this is only sometimes true in non-cubic systems. For example, the direction [111] is perpendicular to the plane (111). In high-index facets, such as (222) and (333) reflecting planes refer to second and third-order reflections from the (111) lattice planes, respectively, as well as (200) reflecting planes can be referred to second–order reflections from the (100) lattice planes (Fahlman, 2007).

In addition, an **octahedral AgCl crystal seed** produced hexapod AgCl preferential overgrowth along ⟨100⟩ directions and described crystallographic orientation of octahedral seed by Gatemala and co-workers as shown in Figure 7b. For the octahedral seed, it is comprised of usually eight-face of {111} facet which contains; (111), ($\bar{1}\bar{1}\bar{1}$), (11$\bar{1}$), ($\bar{1}\bar{1}$1), (1$\bar{1}$1), ($\bar{1}$1$\bar{1}$), (1$\bar{1}\bar{1}$), and ($\bar{1}$11). In the directions, a number of the family ⟨100⟩, ⟨110⟩ and ⟨111⟩ are equal to be found in cubic seed (Gatemala et al., 2014) because an octahedron comes from the cubic slide off, that is in the same direction.
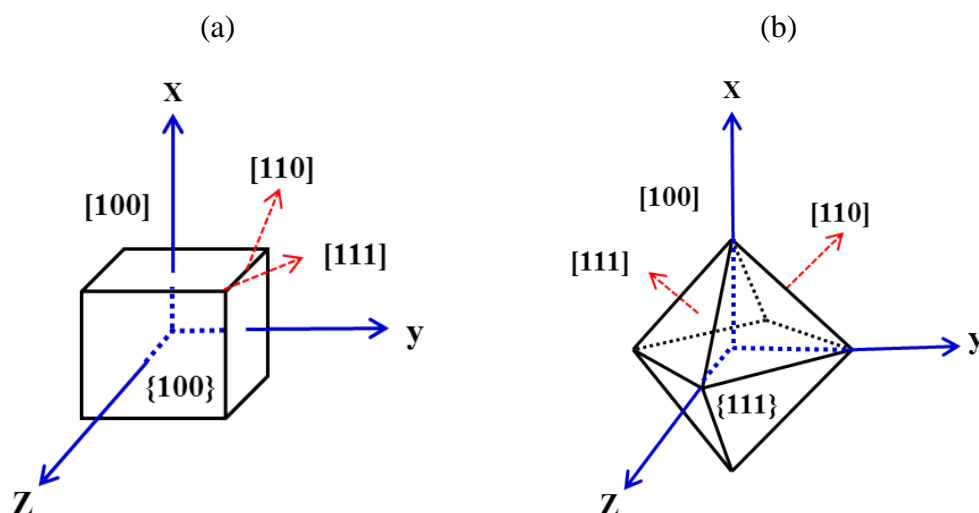
Figure 7 The crystallographic orientation of (a) cubic AgCl crystal (modified from Lou et al., 2012; Lou et al., 2013), and (b) Octahedral AgCl crystal (modified from Gatemala et al., 2014).

2.2.3 Surface structure and reactivity

The ease to nucleation of product phases also depends on the actual surface structure of the reacting phase. From a consideration of crystal structure it can be shown that in most crystal the structure cannot be the same over the entire crystal surface. For example, MgO with the rock salt structure formed perfect cubes as in Figure 8a. Each cubic face has (100) type and hence anions and cations alternate at the corners of a square grid (Figure 8b). In the same crystal, cubooctahedron and octahedron of MgO have different surface structures which all corners are absent to reveal {111} faces shown in Figure 8c and 8e, respectively. In these orientations, the {111} planes of MgO contain alternate layers of Mg^{2+} and O^{2-} ions (Figure 8d and 8f); hence a {111} surface will be either a complete layer of Mg^{2+} ions or a complete layer of O^{2-} ions (West, 1984). This is obviously very different to the structure of the {100} surfaces.

(a)

100

(c)

111   100

(e)

111

(b)

{100} face

Mg   O   Mg O
O   Mg O   Mg
Mg   O   Mg O
O   Mg O   Mg

(d)

{111} face

Mg   Mg
Mg   Mg   Mg
Mg   Mg
Mg   Mg   Mg
Mg   Mg

(f)

{111} face

O   O
O   O   O
O   O
O   O   O
O   O
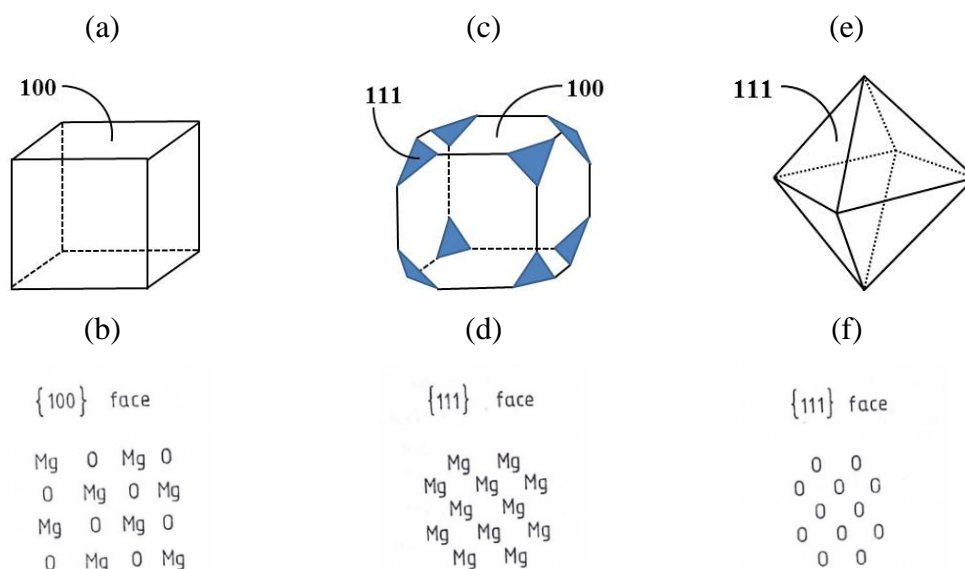
Figure 8 Surface structure of MgO crystal displaying (100) and {111} surfaces (West, 1984).

In solid, different crystal planes (facets) on the surface have different surface energy (γ). From the Density Functional Theory (DFT) calculations, the surface energy (γ_{AgCl}) of AgCl {100}, {110} and {111} facets with a clean surface was estimated to be 0.308, 0.511, and 1.046 $J\,m^3$, respectively. Hence, the {100} facets of AgCl is the preferred site during the growth process since growing along this direction of low energy leads to higher stability crystals. With excess Cl⁻ in solution or Cl⁻ maximum adsorption (high concentration of NaCl), the surface energy of AgCl {100}, {110} and {111} facets is reduced to 0.350, -0.181, and -0.273 $J\,m^3$, respectively. The surface energy of {111} and {110} facets is reduced rapidly to lower than that of {100} facets. We can predict that the growth of {111} and {110} facets are more preferred and fast and the growth of {100} facets will be restricted. In addition, since the surface energy of {111} facets is lower than that of {110} facets, we can expect to see the faster growth along the ⟨111⟩ than the ⟨110⟩ directions of AgCl cubic seeds. Therefore, Ag^+ ions that are oxidized from Ag plates by $HClO_4$ prefer to react with Cl⁻ on the lowest surface energy of {111} facets of cubic seeds to form concave cubes and hierarchical structure by preferential growth along the ⟨111⟩ directions (Lou et al., 2012; Dong et al. 2012).

Table 1 Surface energy of AgCl {100}, {110}, and {111} of clean surface (γ_{AgCl}) compared to Cl⁻ adsorbed (γ_{Cl^-}) (Ma et al., 2012).

Surface energy, γ ($J\ m^3$)	Facets		
	{100}	**{110}**	**{111}**
γ_{AgCl}	0.308	0.511	1.046
γ_{Cl^-}	0.350	–0.181	–0.273

2.2.4 Additive reagents

It is well–known that the normal morphology of NaCl is as cubes presenting {100} faces (Figure 9a), but if carbonyldiamine (urea, CH₄N₂O) is added to the solution the crystals that form are octahedral in which each face is a {111} face. The crystal growth started with the cube with its corners sliced off i.e. NaCl crystal has both {100} and {111} surfaces. When only the {100} faces are allowed to grow, the corners of the cube completed to give (b). The carbonyldiamine, clearly, must act to reduce the growth rate of {111} faces of NaCl compared to the growth rate of the {100} faces so that, the {100} faces grow out of the crystal, only the {111} faces are left. This indicated that the carbonyldiamine acted to influence the reactivity of the {111} surfaces and is not to be incorporated into the crystals (Glusker et al., 1994).

(a)   (b)
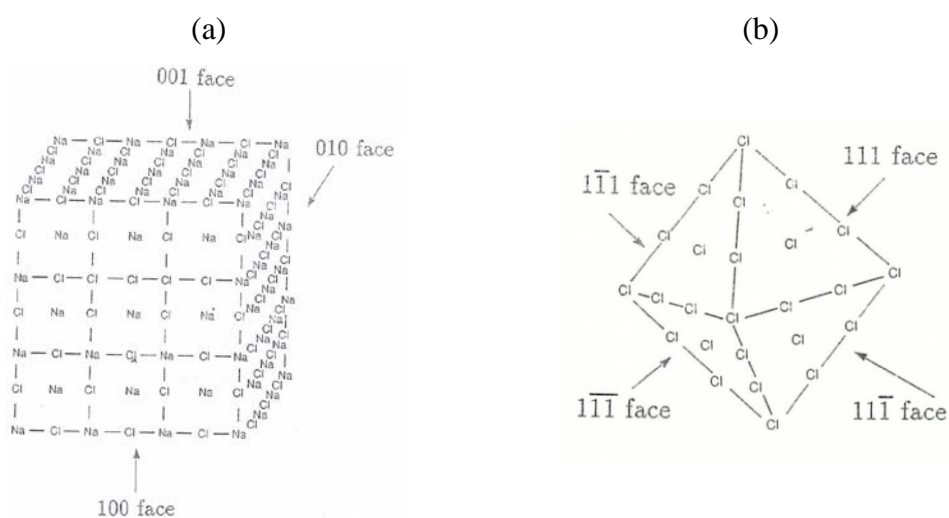
Figure 9 Crystals of cubic symmetry in the form of (a) a cube and (b) an octahedron (Glusker et al., 1994).

Polyvinylpyrrollidone, PVP, non-ionic surfactant, has an easily polarized functional group '–C=O' in its repeated unit, which 'O' is negative charge. As we know, PVP is often used as "capping reagent" in nanomaterial fabrication because the oxygen atoms of PVP can bond preferentially to {100} facets of FCC metallic Ag and therefore PVP has been used to reduce the growth rate of Ag on {100} facets. Because the Ag atoms on {100} faces of both metallic Ag and AgCl have similar periodicity, PVP is able to use for inhibiting AgCl {100} faces (Chiu et al., 2012).

Chen et al, 2014, synthesized hierarchical Ag/AgCl nanocrystals via precipitation between the solid porous PVP–Ag^+ precursor and NaCl solution. The bonding formation was observed with stretching vibration at 2400 cm^{-1} due to the complex of Ag^+----^-O=C from pyrrollidone ring. In the solid PVP–Ag^+ precursor obtaining from freeze–drying route showed the strongest XRD diffraction peak of (220) planes. Compare it to the diffraction peak of $AgNO_3$ as the standard data it was found that the strongest diffraction peak is (211) planes. This indicated that $AgNO_3$ crystals in the PVP–Ag^+ precursor prefer to grow on the orientation along [220] directions because of the effects of PVP molecules (Chen et al., 2014).

2.3 Nanotechnology

Nanotechnology is the characteristic structural features isolate between atoms and bulk materials; i.e. particles are in the range of about 1 to 100 nm, which displays physical attributes substantially different from those bulk materials. In the case of a single bulk material divided into multiples clusters, surface area increasing geometrically as more new surface is created. For example, a cube of some materials that is 1 m on each side has surface area equal to 6 m^2. If this cubic were broken perfectly into smaller cubes that are 1 cm on each side, the collective surface area increases to 600 m^2. For cubes with 1 mm edges, the surface are expands to 6000 m^2. This trend was illustrated in Figure 10. Such materials can be designed to exhibit novel and significantly improved physical, chemical and biological properties (Hornyak et al., 2009).
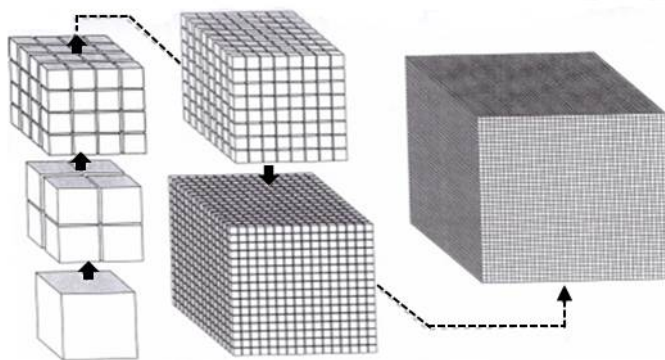
Figure 10 A visual image of the concept of collective surface area (Hornyak et al., 2009).

2.4 Synthesis method

For the fabrication of nanoparticles, a small size is not the only requirement. For any practical application, the processing conditions need to be controlled in such a way that resulting nanoparticles have the following characteristics: (i) identical size of all particles or uniform size distribution, (ii) identical shape and morphology, (iii) identical chemical composition and crystal structure that are desired among different particles and within individual particles, and (iv) individually dispersed or monodispersed, i.e. no agglomeration (Kelsall et al., 2005). There are a number of techniques developed for fabricating the inorganic materials, but in this part we will describe only some methods in the following sections.

2.4.1 Sol-gel method

The sol-gel method is a versatile process used in making various inorganic materials. In a typical sol-gel process, a colloidal suspension, or a sol, is formed from the hydrolysis and polymerization reactions of the precursors, which are usually inorganic metal salts or metal organic compounds such as metal alkoxides or metal chlorides. Complete polymerization and loss of solvent leads to the transition from the liquid sol into a solid gel phase (Tseng et al., 2010). For the synthesis of TiO_2 route base-catalyzed, the reaction between $TiCl_4$ and diluted NH_3 solution formed the white precipitate. The synthesis can be described by the following chemical reaction (Kanna, 2002):

$$TiCl_4 + 4NH_4OH \longrightarrow TiO_2 + 4NH_4Cl + 2H_2O \tag{1}$$

NH$_4$OH most likely dissociates to NH$_3$ and H$_2$O than NH$_4^+$ and OH$^-$. In this synthesis of TiO$_2$, sol-gel method can be explained in term of hydrolysis and the condensation reaction as (Tseng et al., 2010; D. Chen et al., 2014; Burda et al., 2005);

The hydrolysis reaction

$$TiCl_4 + 4H_2O \rightleftharpoons Ti(OH)_4 + 4H^+ + 4Cl^- \tag{2}$$

The condensation reaction

$$Ti(OH)_4 \rightleftharpoons TiO_{2\,(s)} + 2H_2O \tag{3}$$
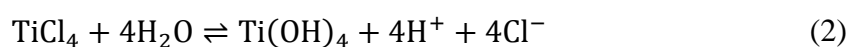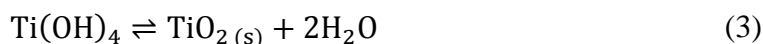
2.4.2 Ion–exchange reaction

In one of the most famous reactions in chemistry, addition of colorless aqueous solution of AgNO$_3$ to an equally colorless solution of NaCl or HCl produces white precipitate of AgCl by replacing of Cl$^-$ ions on other anions according to the equation (Dong et al., 2012):

$$AgNO_{3\,(aq)} + NaCl_{(aq)} \longrightarrow AgCl_{(s)} + NaNO_{3\,(aq)} \tag{4}$$

$$AgNO_{3\,(aq)} + HCl_{(aq)} \longrightarrow AgCl_{(s)} + HNO_{3\,(aq)} \tag{5}$$
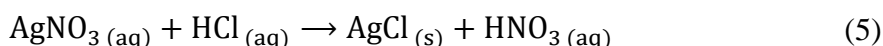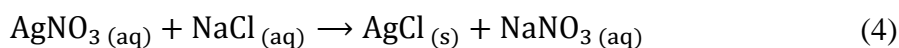
Usually, cubic AgCl crystal will be obtained from the common prepared methods. Several studies synthesize to change the morphology of AgCl crystal using some polymeric agents such as PVP as mention above. For instance, other types of halides and silver sources were used, some examples are:

Wang et al., 2011, synthesized core–shell nanorod of Ag$_8$W$_4$O$_{16}$/AgCl by ion-exchange reaction between incubated Ag$_8$W$_4$O$_{16}$ in NaCl solution. The partial Ag$^+$ ions dissolve in the aqueous solution of NaCl and subsequently react with Cl$^-$ ions according to equation (Wang et al., 2011):

$$Ag_8W_4O_{16} \rightarrow 8Ag^+ + 4WO_4^{2-} \tag{6}$$

$$Ag^+ + Cl^- \rightarrow AgCl \tag{7}$$
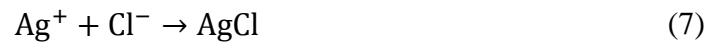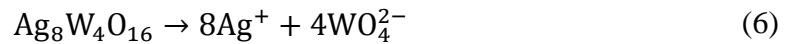
Because the morphology of precursor plays important role in determining the morphology of AgCl, silver molybdate (Ag_2MoO_4) was used to prepare microrod, irregular ball, and hollow spherical AgCl through the ion-exchange process as follows (Wang et al., 2010):

$$Ag_2MoO_4 + 2HCl \rightarrow 2AgCl + MoO_3 + H_2O \tag{8}$$
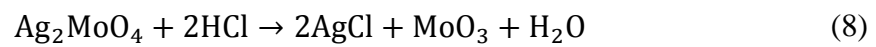
AgCl can be prepared to form Ag/AgCl by directly reducing AgCl with $NaBH_4$ ethanol solution. The color of nanocubic AgCl suspension changes to dark grey after adding $NaBH_4$ solution, indicating that Ag^+ ions were reduced to metallic Ag^0 and deposited on AgCl nanocubes (Cui et al., 2014):

$$BH_4^- + AgCl + 2H_2O \rightarrow Ag + BO_2^- + Cl^- + 8H^+ \tag{9}$$
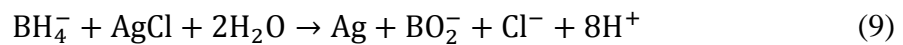
Metallic Ag nanoparticles can be oxidized by H_2O_2 containing HCl solution to form Ag^+ ions, eq. (10), and subsequently combined with Cl^- ions to produce AgCl powder (Li and Ding, 2010):

$$2Ag + H_2O_2 + 2H^+ \rightarrow 2Ag^+ + 2H_2O \tag{10}$$
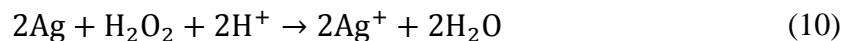
2.5 Applications of powder X-ray diffraction (XRD)

The X-ray wavelength commonly employed is the characteristic K_α radiation, $\lambda = 1.5418$ Å, emitted by Cu target. When crystal diffracts X-ray, it is the atoms or ions which act as secondary point sources and scatter the X-rays (Figure 11a); in the optical grating, it is the lines scratched or ruled on the glass surface which cause scattering. The resulting image is due to a combination of reflected beams from many parallel lattice planes. A characteristic diffraction pattern is observed on the photographic plate (see Figure 11b) (Turton, 2000).

(a)   (b)
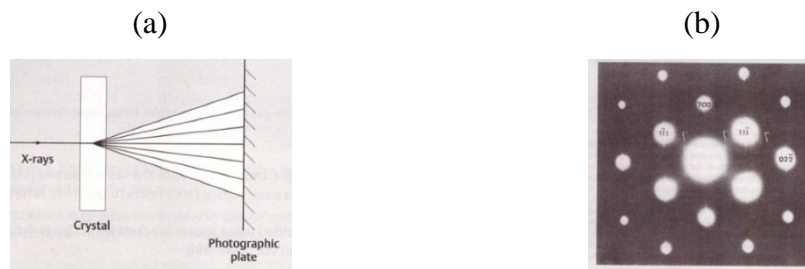
Figure 11 (a) Schematic representation of the experimental set-up for studying diffraction of X-ray by a crystal. (b) An example of a diffraction pattern from SiGe crystal (Turton, 2000).

In the diffractometer, the angle (d spacing) and intensities of the high–angle reflected beams serve as a 'fingerprint' for the crystal structure. Therefore, the unknown crystalline materials can be identified by comparing the XRD pattern with a database of Joint Committee on Powder Diffraction Standards (JCPDS), which lists an invaluable reference source (Kelsall et al., 2005).

2.5.1 Inter planar distance (d-spacing)

Let us consider the reflection from two parallel planes within the crystal, as shown in Figure 12. We can see from the diagram that the ray which is reflected from plane B travels slightly further than that which is reflected from plane A. The extra distance travelled by the ray reflected from plane B is equal to the sum of the distance from U to V and from V to W.
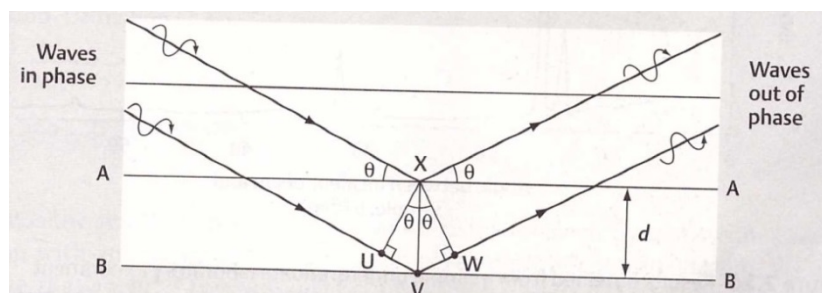
Figure 12 The Bragg construction used to explain the reflection of X-rays from a crystal (Turton, 2000).

The two-dimensional array of lattice points is shown in Figure 13. This array of points may be divided up into many different sets of rows and for each set there is a characteristic perpendicular distance, d, between pairs of adjacent rows.

Using basic trigonometry we find that this distance is equal to $2d \sin\theta$, where θ is the angle between the incident beam and the reflection plane and d is the separation of the atomic planes or interplanar d-spacing. This is known as the Bragg condition and is expressed by the relation (Turton, 2000):

$$n\lambda = 2d_{hkl} \sin\theta \qquad (11)$$

Where λ is the wavelength, n the order of reflection, d_{hkl} the lattice plane spacing, and θ is the angle of reflection to the plane.

Moreover, interplanar d-spacing can be obtained from HRTEM image and separated two distinct of d-spacing values as area A and B in Ag/AgCl nanoparticle (Figure 13). The large particles of area A are 2.78 Å which are the diffraction pattern of AgCl [200] layer. In area B, the d-spacing of small particles is 2.38 Å corresponding to the diffraction pattern of metallic Ag [111] layer. Two different d-spacings suggested that metallic Ag was reduced from the outer surface of AgCl able to introduce on their surface (Choi et al., 2010).
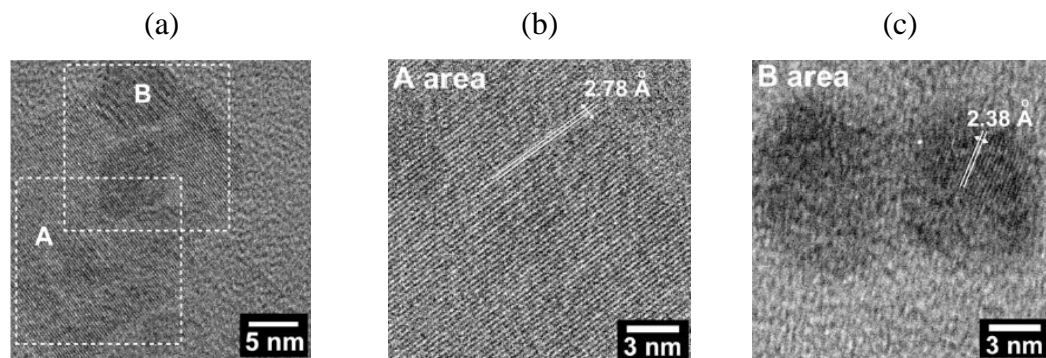
Figure 13 (a) HRTEM image of Ag/AgCl nanoparticles. (b) and (c) HRTEM images of AgCl and metallic Ag (Choi et al 2010).

2.5.2 Particle size and crystal size

X–ray powder diffraction may be used to measure the average crystal size in powdered sample. The lines in a powder diffraction pattern are of finite breadth but if the particles are very small the lines are broader than usual. The

broadening increases with decreasing particle size. The broadening β due to crystallite grain size D arises from the limited number of diffractions planes within the diffracting object and is given by the Scherrer equation (Shukla et al., 2003):

$$D = \frac{K\lambda}{\beta \cos\theta} \qquad (12)$$

where D is the thickness of the crystal (in angstroms), K the Plank's constant, λ the X-ray wavelength, θ is the Bragg angle, and β the line broadening obtained from the extra peak width at half the peak height (FWHM) such as strongest lines for the anatase TiO_2, rutile TiO_2, and AgCl are (101), (110), and (200), respectively.

There is a large different between the size evaluated by XRD, TEM, BET and SEM. The size values provided by XRD and TEM correspond to the size of the grains giving an average **crystallite size**. The individual grains aggregate to form big size or **particle size** were determined by BET surface area. Many particles size agglomerate that is **aggregate size** and visible in the SEM image as shown in Figure 14 (Baiju et al. 2007; Khoshkhoo et al., 2013).
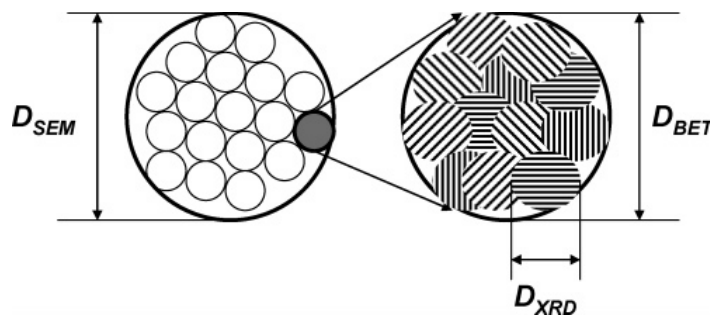
Figure 14 Schematic representation of the average crystallite size, average particle size, and average aggregate size correspond to XRD, TEM, BET, and SEM, respectively (Baiju et al., 2007).

2.5.3 Peak intensities

Preferred orientation changes the relative integrates intensities of the peaks observed in the diffraction pattern, and reflects the presence of important microstructural features which affect the material properties. The ratios of peaks intensity of X-ray diffraction peaks can be applied to describe the facets growth along once direction. For cubic AgCl with flat {100} facets, the weak peak intensity ratio of its (111)/(200) and (220)/(200) are 0.08 and 0.1, respectively. When prolong the reaction time of the synthesis to 1 h, 4 h, and 8 h, the peak intensity ratio of both (111)/(200) and (220)/(200) are 0.28, 0.12; 0.16, 0.26; 0.24, 0.30, respectively, based on the stronger X-ray diffraction peak indicating concave cubic AgCl preferential growth along ⟨111⟩ and ⟨110⟩ directions of cubic seeds (see Figure 6) (Lou et al., 2012).

2.6 Heterogeneous photocatalyst

The semiconducting materials absorbed a photon that must be at least as large as their band gaps giving the electron enough energy to enter the conduction band and leaving behind a hole in the valence band (Falhlman, 2007)

Electronic calculations showed that the valence band or HOMO of AgCl is non–bonding of doubly degenerate $3p_x$ and $3p_y$ lone pair electron and conduction band or LUMO is a sigma anti-bonding ($\sigma^*[5s(Ag)]$). The HOMO-LUMO electronic transition is a charge transfer (CT) type of lone pair electron in non-bonding to sigma anti-bonding ($n[3p_{x,y}(Cl)] \rightarrow 5s(Ag)$) as shown in Figure 15 (Glaus and Calzaferri, 1999).
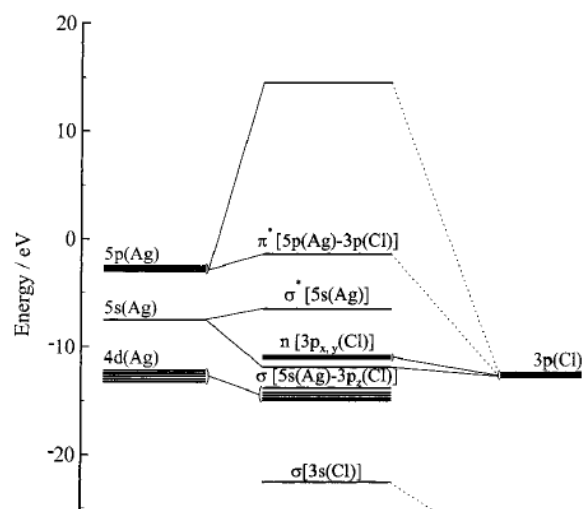
Figure 15 Molecular orbital diagram of AgCl molecule (Glaus and Calzaferri, 1999).

In the field of photocatalytic AgCl, it is known as *Ag/AgCl* formation and always reduced by light irradiation for generating metallic Ag nanoparticles (Wang et al., 2008; Wang et al., 2009) which are highly active under visible light. On the other hand, AgCl can be reduced by some reagents such as ethylene glycol (Jiang and Zhang 2011), sodium borohydride (An et al. 2011), and ascorbic acid (Ma et al., 2013). For the photocatalytic mechanism, metallic Ag nanoparticles can absorb visible light by surface plasmon resonance (SPR) leading to electron-hole separation (Eq. (13)). A fraction of SPR-mediated energetic electrons are injected into the conduction band of AgCl and trapped by O_2 molecules in solution which subsequently could form superoxide ions $(\cdot O_2^-)$ and reacted with organic pollutant (Eq. 14, 15). Whereas the holes are transferred to the surface of AgCl and subsequently combined with Cl^- ions to form Cl^0 atoms (Eq. 16) which are active species for decomposition of dye molecules and can return to Cl^- ions again (Eq. 17, 18) (Dong et al., 2012; An et al., 2011).

$$Ag\,NPs + h\nu \rightarrow Ag\,NPs^{\ominus} + Ag\,NPs^{\oplus} \tag{13}$$

$$Ag\,NPs^{\ominus} + O_2 \rightarrow \cdot O_2^- \tag{14}$$

$$\cdot O_2^- + organics \rightarrow degradations\ products \tag{15}$$

$$Ag\,NPs^{\oplus} + Cl^- \rightarrow Cl^0 \tag{16}$$

$$Cl^0 + organics \rightarrow degradation\ products + Cl^- \tag{17}$$

$$Cl^0 + OH^- \rightarrow Cl^- + \cdot OH \tag{18}$$
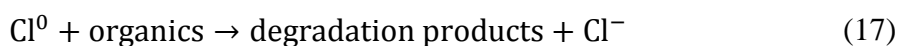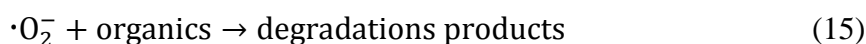
2.7 Surface plasmon resonance effect (SPR)

A variety of metals have been used to generate surface plasmon resonance or SPR. Gold (Au) and silver (Ag) particles are dominated because of their stability at small sizes and strong SPR absorption bands in the visible region (Jones et al., 2011). Especially, Ag metal, it has unique properties. Metallic Ag nanostructures can serve as antennas to convert light into localized electric fields (E-fields) or as waveguides to route light to desired locations with nanometer precision. When the oscillating electric field from incident light interacts with the delocalized electrons of a metal, the oscillating electromagnetic field of the light induces a collective coherent oscillation of the free electrons of the metal. This electron oscillation around the particle surface causes a charge separation with respect to the ionic lattice, forming a dipole oscillation along the direction of the electric field of the light as shown in Figure 16 (Willets and Duyne, 2007).
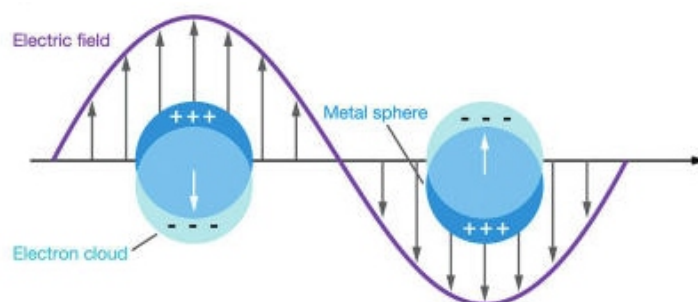
Figure 16 Schematic diagrams illustrating a surface plasmon resonance (Willets et al., 2007).

SPR effect brings several significant benefits to the photocatalysis such as Ag nanoparticles can be tailored to fall in the visible range or the near-UV range, it responses to a visible light suitable for the large-band gap photocatalysts (e.g., ZnO, TiO_2, AgCl), a short distance between the photoexcited electrons and holes and the surface is useful to materials presenting poor electron transport. These increase the redox reaction rate and the mass transfer, enhancing the concentration of charge carriers (Zhang et al., 2013).

2.8 Orange G (OG) dye

Azo dyes are among the most notorious widespread environmental pollutants associated with textile, cosmetic, food colorants, printing, and pharmaceutical industries (Pinheiro et al., 2004). Orange G or acid orange 10 is one of a synthetic azo dyes (monoazo dye class), which are characterized by the presence of one azo bond (–N=N–). The maximum absorption spectrum of orange G dye at 480 nm (λ_{max}) could be assigned to the n–π^* transition of the chromophore (–N=N–) group. The weak band at 310-330 nm could be attributed to the π–π^* transition related to the aromatic ring attached to the –N=N– group in the dye molecule (Muthukumar et al., 2007; Khataee et al., 2009). Orange G dye shows only two colors in aqueous solution, brilliant orange in neutral and acidic pH or red in pH greater than 9. A possible degradation pathway of orange G dye, in the presents of titanium-chromium oxide composite, occurred mainly by 3 pathways; hydroxylation of aromatic ring, desulfonation, and oxidative cleavage of azo bond are given in Figure 17 (Meetani et al., 2011).
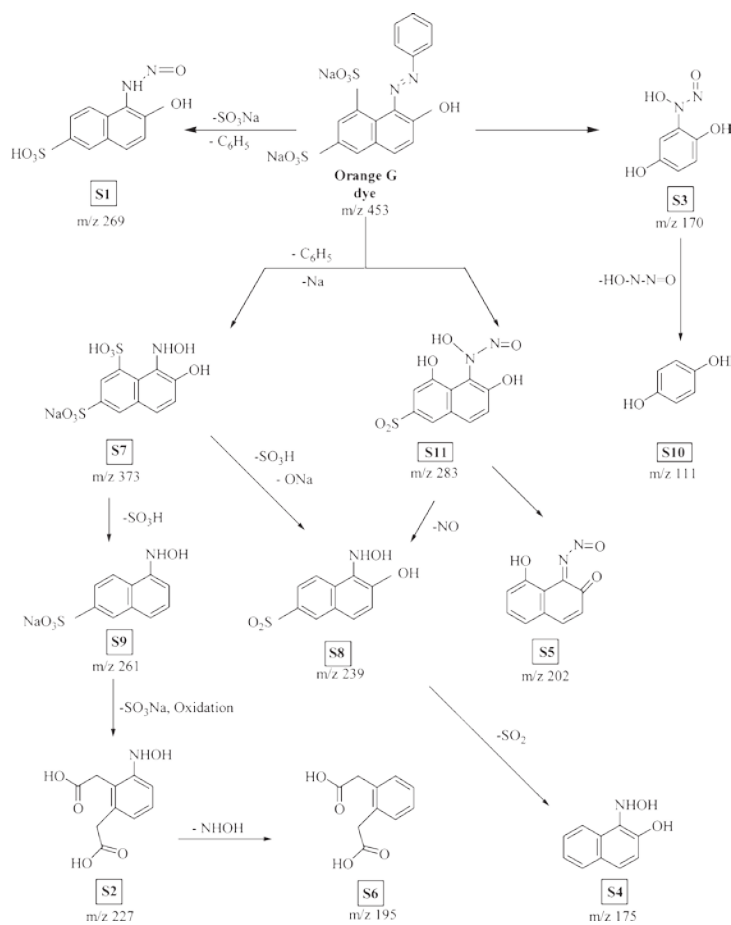
Figure 17 Schematic diagram of various intermediate formations of orange G dye as a result of photocatalytic degradation (Meetani et al., 2011).

The sulfonyl group was directly attacked by a photo-induced radical ($H^\bullet$) resulting to the formation of innoxious ions (SO_4^{2-}). These are formed by the cleavage of C–S bond to form $SO_3^{\bullet-}$, followed by the reaction with hydroxyl anions (OH^-). The reaction can be represented in reaction (19)–(21), where Φ replaces any alkyl, aryl or a part of dye structure as follows (Lachheb et al., 2002):

$$OH^- + p^+ \longrightarrow OH^\bullet \tag{19}$$

$$\Phi - SO_3^- + OH^\bullet \longrightarrow \Phi - OH + SO_3^{\bullet-} \tag{20}$$

$$SO_3^{\bullet-} + OH^- \longrightarrow SO_4^{2-} \tag{21}$$

For the oxidative cleavage of azo bond involve the cleavage in the vicinity of the azo bond which leads to the formation of N_2 as one of the mineralization products. These can be presented as the chemical reaction as Eq. 22 and Eq. 23. The carboxyl radicals react with a valence band hole through the photo–Kolbe decarboxylation reaction, which produces CO_2 as another mineralization product. This reaction can be presented as Eq. 24;

$$\Phi–N=N–\Phi' + H^\bullet \longrightarrow \Phi-N=N^\bullet + \Phi–H \tag{22}$$

$$\Phi–N=N^\bullet \longrightarrow \Phi^\bullet + N{\equiv}N \tag{23}$$

$$\Phi–COO + h_{VB}{}^+ \longrightarrow \Phi^\bullet + CO_2 \tag{24}$$
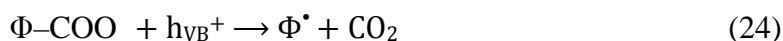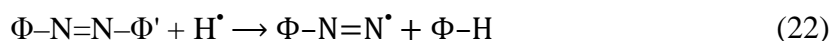
Subsequently, radical $\Phi^\bullet$ will generate methyl radicals, which will be oxidized to methanol, then to formaldehyde and eventually to formic acid and finally decomposes via the photo-Kolbe reaction into CO_2 and $H^\bullet$ as shown in Eqs. (25)-(31).

$$CH_3{}^\bullet + OH^\bullet \longrightarrow CH_3OH \tag{25}$$

$$CH_3OH + OH^\bullet \longrightarrow H_2O + {}^\bullet CH_2OH \tag{26}$$

$${}^\bullet CH_2OH \longrightarrow H–CHO + H^\bullet \tag{27}$$

$${}^\bullet CH_2OH + OH^\bullet \longrightarrow CH_2(OH)_2 \longrightarrow H–CHO + H_2O \tag{28}$$

$$H–CHO + OH^\bullet \longrightarrow H–CO^\bullet + H_2O \tag{29}$$

$$H–CO^\bullet + OH^\bullet \longrightarrow H–COOH \tag{30}$$

$$H–COOH + h_{VB}{}^+ \longrightarrow H^+ + CO_2 + H^\bullet \tag{31}$$
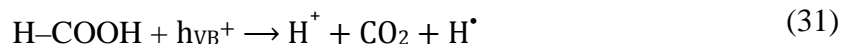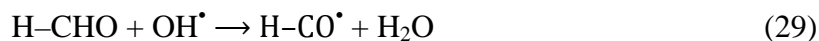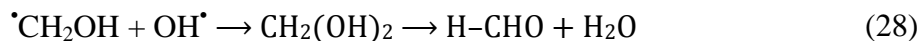
Hence, the degradation pathway starting from hydroxylation of aromatic ring, followed by desulfonation and oxidative cleavage of azo bond leads to the complete mineralization of orange G dye at the end of the reaction.

3. Results and discussions

In the preparation, silver halides precipitated from Ag^+ ions and halides ions (Br^-, Cl^-, I^-) immediately. Generally, it is difficult to control the morphology of AgCl because of the high reaction rate between Ag^+ and Cl^- ions (Han et al., 2011). In this work, we have concentrated on many effects and succeeded in preparation of silver chloride (AgCl) with different morphologies such as urchinlike, concave cube, octapod, Rubik's cube, flowerlike, hexapod, the details of which are given as follows.

3.1 Urchinlike Ag/AgCl

Many researchers have synthesized titanium dioxide (TiO_2) by sol-gel method using titanium tetrachloride ($TiCl_4$) as titanium sources (Wang et al., 2011; Klosek and Raftery, 2001). In the presence of diluted ammonium hydroxide base-catalyst, a white precipitation of TiO_2 will be formed. However, from **Paper I**, when diluted ammonium hydroxide solution was evaporated under reflux at 100 ℃ for 2 h the clear colorless solution was obtained (see Figure 18a) even though there were white solid precipitated during drastic reaction. After one week, this colorless solution yielded the white precipitation of amorphous TiO_2 with trace amount of rutile TiO_2 (Figure 18b) as shown by the diffraction pattern with 2θ = 27.4, 36.1, 41.2, 44.0, 53.9, 56.5, 62.6, 68.7, 70.3 corresponding to (110), (101), (111), (210), (211), (220), (002), and (301) of rutile TiO_2 (Melghit et al., 2009). No anatase phase TiO_2 was detected. In the same condition, if small amount (less than 5 mL) of $AgNO_3$ solution, which had been refluxed from 1 g of $AgNO_3$ dissolved in 80 mL of NH_4OH, was slowly added to neat $TiCl_4$ liquid, a large amount of white solid formed with some small yellow areas at the surface. This solid would turn to white solid of amorphous TiO_2 with some small amount of rutile TiO_2 mixed in (Figure 18c), if let standing in air. In addition, we noticed that besides the peaks of TiO_2, another two of AgCl diffraction peaks were observed in this pattern, they were (200) diffraction peak at 2θ = 32.24°, and (220) diffraction peak at 2θ = 46.25°, respectively. When the amount of $AgNO_3$ in ammonia solution was increased to *ca.* 7 mL the light yellow colloid was obtained

32

(Figure 18d). If larger amount (e.g. 10 mL) was added the colloid formed but rapidly dissolved and white powder of AgCl began to precipitate in the clear light yellow solution (Figure 18e). When the addition reached 80 mL the clear light yellow solution completely disappeared and the clear colorless solution with purple-gray powder of urchinlike Ag/AgCl was obtained as shown in Figure 18f and g. The color change of this AgCl product from white to purple-gray during the filtration and rinsing could be because of the presence of metallic Ag nanoparticles. The clear colorless, filtered out from the white powder of Ag/AgCl, was left standing at room temperature for about 1 week it precipitated to give amorphous TiO$_2$ (Figure 18h). In the un-refluxed AgNO$_3$ solution, the product yielded different result as the amorphous TiO$_2$ was obtained as the major product with a trace of AgCl (Figure 18i).

(a)	(b)	(c)
(d)	(e)	(f)
(g)	(h)	(i)
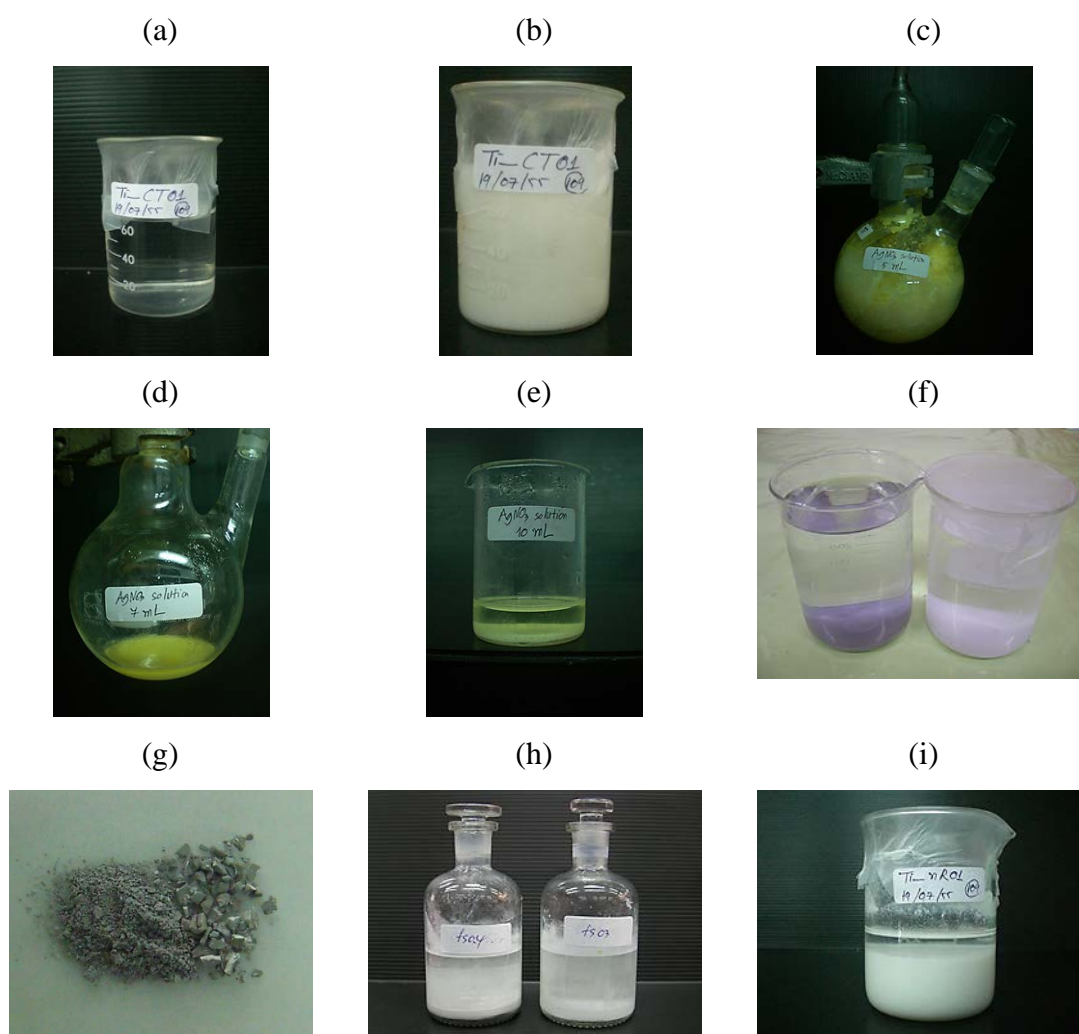
Figure 18 The images of various kinds of the powder precipitation.

Urchinlike morphology may be generated by $TiCl_4$ which has some effect on the growth of nanohairs *via* forced hydrolysis of $TiCl_4$ precursors as found in the work by Wang et al (Wang et al., 2011). The nanohairs on the surface may play an important role here as "the hook and loop fastener" that helps binding small particles together to form the larger ones. As a result, the overall morphology of the urchinlike Ag/AgCl particles aggregated into a nearly spherical shape as observed from SEM images (Figure 19a, b) which were different from the sizes as seen from TEM images (Figure 19c, d) due to the disruption by ultrasonic during the sample preparation for TEM technique.

(a)   (b)

(c)   (d)
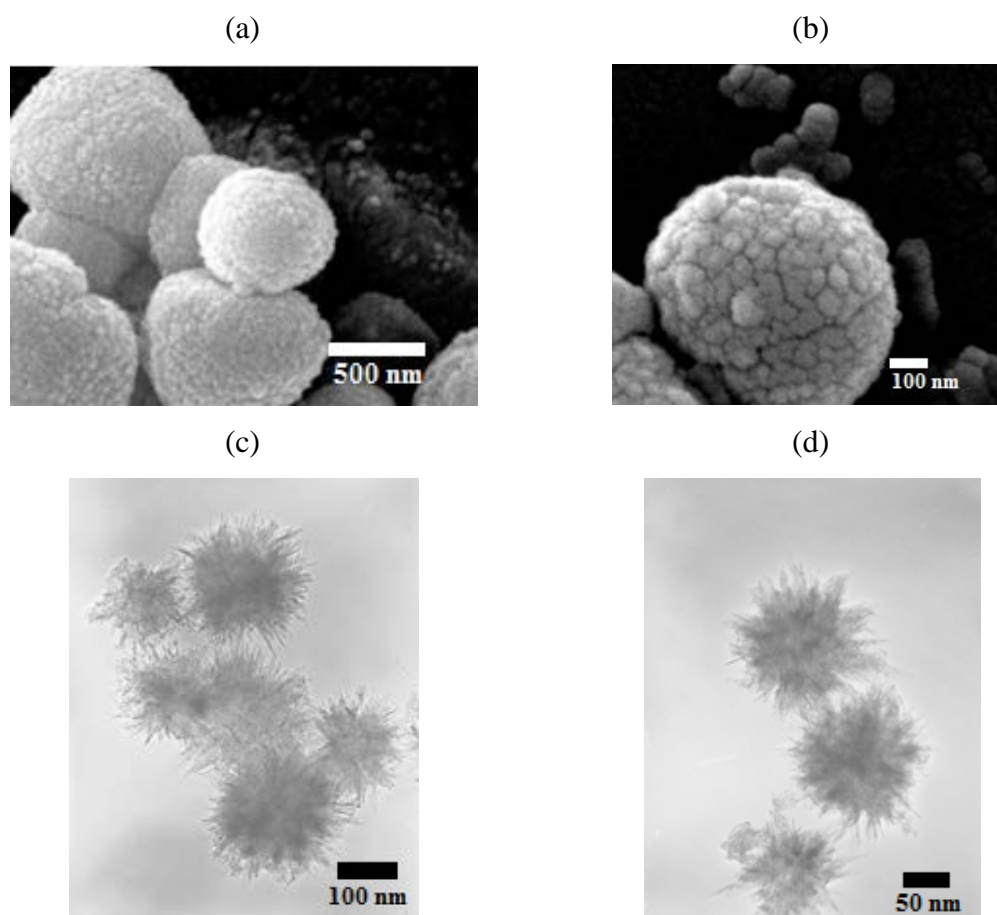
Figure 19 The particle morphologies are: (a), (b) agglomeration of urchinlike from SEM image (c) and (d) TEM image of urchinlike.

The possible chemical reactions may be as follows:

$$AgNO_{3(aq)} + TiCl_{4(l)} \longrightarrow AgCl_{(s)} + TiCl_3(NO_3)_{(aq)} \qquad (32)$$
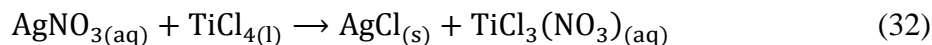
3.2 Growth process: concave cube, octapod, Rubik's cube AgCl, flowerlike

In a typical synthesis from **Paper II**, the bluish purple powder of flower-like AgCl (Figure 20) were synthesized *via* ion-exchange reaction of $AgNO_3$ and $AlCl_3$ as precursors with temperature 100 ºC and may be simply expressed as follows:

$$AlCl_{3\ (aq)} + 3H_2O_{\ (l)} \rightarrow Al(OH)_{3\ (s)} + 3HCl_{\ (aq)} \qquad (33)$$

$$AgNO_{3\ (aq)} + HCl_{\ (aq)} \rightarrow AgCl_{\ (s)} + HNO_{3\ (aq)} \qquad (34)$$

(a)   (b)
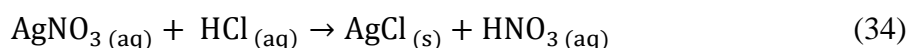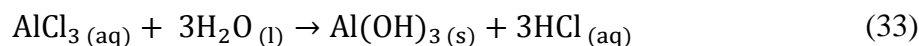
Figure 20 The images of two kinds of the powder (a) the commercial AgCl powder and (b) the flower-like Ag/AgCl powder.

To understand the growth behavior of the flowerlike AgCl microcrystal from concave cubic through Rubik's cube assisted by vinyl acetate monomer (VAM), it was necessary to investigate its growth mechanism. This can be proved by the SEM and XRD results. The diffraction peaks of different morphologies hardly changed but their intensities were enhanced. Similar results had been observed by other researchers (Zhou et al., 2011). This result was useful on examining the relative intensities of the diffraction peaks relevant to the measure of degree of

orientation. In cubic AgCl crystals system, generally, the XRD intensity of (111) is lower than that of (220) peak (Zhu et al., 2012). The relative intensity between (111)/(220) and (222)/(311) was calculated to study its relationship among the different AgCl microstructures as shown in Table 2.

A series of experiments were performed with 30 mL of $AlCl_3$ of different concentrations while keeping the concentration of VAM and CH_3COOH solutions unchanged (10 mL of VAM and 80 mL of 8.72 M CH_3COOH). Starting from 0.75 M of $AlCl_3$ solution, some cubic crystals of size 2.4-2.7 µm were formed with concave face at the center of six {100} facets in SEM image (Figure a, Table 2). Referring to the ratio I_{111}/I_{220} of concave cubes of 1.03 (in Table 2), which was greater than the value 0.86 of standard powder sample of face center cubic AgCl (JCPDS Card file no. 31-1238). It is worth noting, this value of the AgCl concave cubes was the smallest among all the microstructures indicating the lowest value of I_{111}. One can see that the concave cube has not yet started to grow along ⟨111⟩ directions. The population along ⟨111⟩ directions was still low. When 1.25 M $AlCl_3$ solution was used the concave face became more distinct and the cube looked as though it was about to be partitioned into eight smaller cubes by three intersecting planes. The intersected point at the center of the concave face now appeared as a tiny cavity (Figure b, Table 2). The size of the crystal at this point was about 5.0-6.5 µm. Figure c in Table 2 shows when 1.75 M $AlCl_3$ was used, each side face-the {100} face-of the concave cubic AgCl was seen as though it was partially cut by a saw into four pieces. In 3D view, the concave cubic now turned into a shape like the Rubik's cube-the first to be observed. The size of Rubik's cube was about 7.0-7.5 µm. The ratio I_{111}/I_{220} of concave cube grew to octapods and Rubik's cubes was 1.23 indicating that all eight corners or {111} facets gradually grew but not for the edges of cube or {110} facets. At the highest concentration of $AlCl_3$ solution (2.5 M), AgCl crystals grew only along ⟨111⟩ directions to form flower-like AgCl structures and {100} facet disappeared completely as shown in Figure d of Table 2. The size of 3D microflowers were about 15–22 µm. The growth of {111} facet was clear seen in flower-like Ag/AgCl samples where its intensity became obviously stronger than the (220) peak intensity. These implied that AgCl microstructures grew along the ⟨111⟩ direction very well and might have generated overgrowth directions (H. Wang et al. 2012). The I_{111}/I_{220} value (1.49)

of the flower-like AgCl was the largest due to the extra growth along this direction as further shown in the SEM image of different magnifications in Figure 20. As the crystals grew larger, other high-index facets would be affected similarly. Therefore, as shown the ratio I_{222}/I_{311} in Table 2, the relatively slightly stronger (222) reflection than (311) could be seen attributable to the abundance of {222} facet which was a stepped surface composed of {111} terrace (Tran and Lu 2011). For the comparison, under normal condition, the peak intensity of (222) facet is lower than (311) facet of face centre cubic AgCl (JCPDS Card file no. 31-1238).

(a) **(b)**

(c) **(d)**
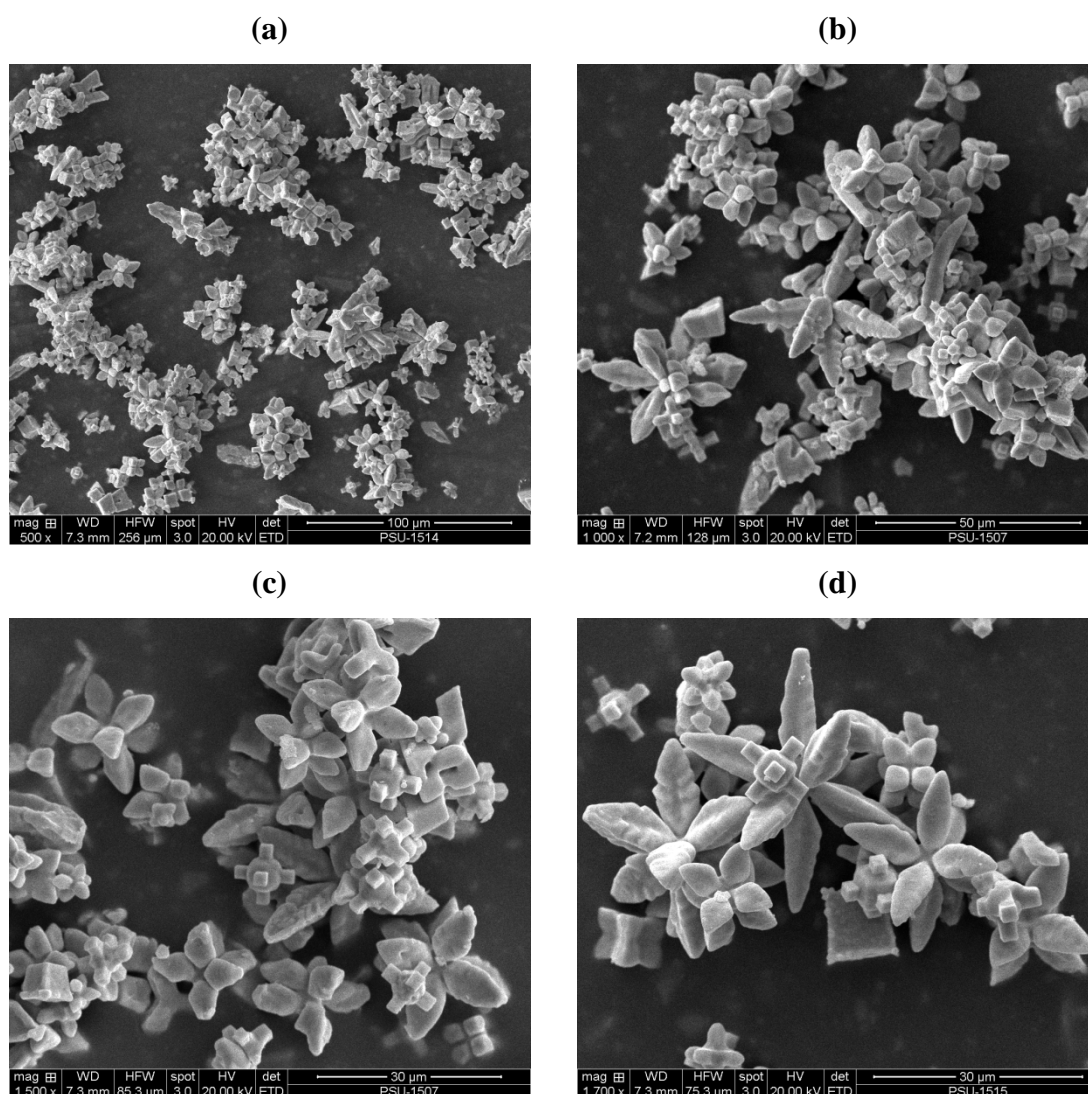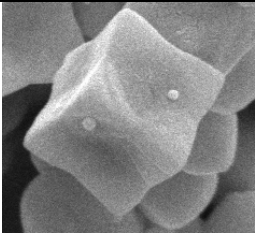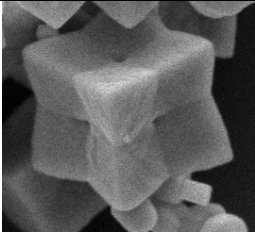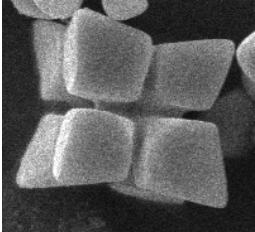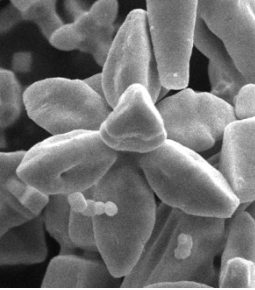
Figure 21 Flower-like Ag/AgCl with different magnifications.

Table 2 Summary of the growth process of flower-like Ag/AgCl and their peak intensity ratios**.**

Sample	Morphology	Peak intensity ratio	
		(111)/(220)	(222)/(311)
JSPDS Card file no. 31-1238	–	0.86	0.95
Concave cubes	(a)	1.03	–
Octapods	(b)	1.23	–
Rubik's cubes	(c)	1.23	–
Flowerlikes	(d)	1.49	1.41

The effect from increasing concentration of $AlCl_3$ as displayed in Table 2 indicated that the Cl^- ion play a critical role in controlling the morphologies of AgCl growth to form the flower-like octapod AgCl structure. The product obtained with 2.5 M $AlCl_3$ was chosen for further studies because of its intricate shape that seemed to be fully developed as much as it could be. Along the growth process, the disappearance of the mass at the center of {100} facets of Rubik's cube possibly was due to the presence of VAM, which could interact more strongly with the {100} sides than with the {111} ends. VAM could serve to reduce the driving force for cubic formation through its selective interaction with the {100} planes. The selective adsorption of VAM on the {100} facets would lead to preferential addition of Ag and Cl atoms to the {111} facets. Therefore, the Rubik's cube could readily grow into a longer petal as long as tens of micrometers because its side surfaces were tightly passivated by VAM molecules, similar to what has been found with PVP (Wang 2000), (Chen et al., 2014). VAM acted as a capping agent to Ag^+ ions and is selectively adsorbed on the six {100} facets of cubic seed. The presence of VAM impeded the growth of the AgCl cubic seeds along ⟨100⟩ directions, and thus octapod flowerlike AgCl microcrystals were obtained.

Based on the above experimental results and analysis, we proposed the whole morphology evolution process of the flower-like AgCl as follows: The combination of Ag^+ and Cl^- produced AgCl cubic seeds (Scheme 1: a → b). This cubic seed then grew into the concave cubic shape with a molecule of VAM associated on the {100} facet via electrostatic interaction (Scheme 1c). The presence of VAM blocked further growth along the {100} facet but no other directions-especially the ⟨111⟩ direction (Scheme 1: c → d). At still higher $AlCl_3$ concentration, growth in the ⟨111⟩ direction was immense and swelled in 3D but the growth along the ⟨100⟩ direction was completely halted, as a result, a Rubik's cube was formed (Scheme 1: d → e), and finally into the flower-like shape (Scheme 1f).
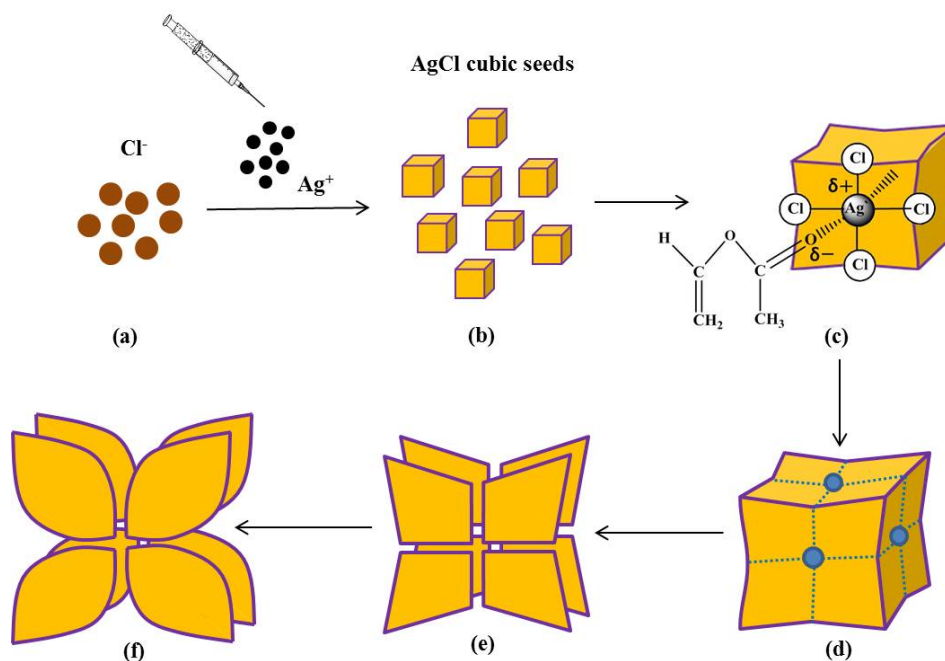
Scheme 1 Crystal growth of flowerlike AgCl in the presence of VAM.

The influence of the acetic acid solution can be attributed to the different interaction between anion and Ag^+ ion. Considering CH_3COO^- and Cl^- competed for coordination with Ag^+ during the growth process, the adsorption rate of Cl^- on the different planes of AgCl nuclei may be affected by the CH_3COO^- (Ni et al., 2004), which favor the slower growth of the {100} faces. Using acetic acid may pose another effect: the etching process by acetic acid solution. Acidic etching of flower-like Ag/AgCl particles may cause the irregular shapes and rough surface. At high concentration of acetic acid solution, the drastic etching process of flower-like structure became severe such that it finally collapsed the flower-like microstructures (Zhao and Yu, 2007) as shown in the subsequent topics.

3.3 Hexapods with depressing of the {111} and octahedron

To investigate the effects of temperature, CH₃COOH concentrations, and amount of VAM were used. At room temperature and 50 ℃, similar irregular particles were obtained and no crystals could be found (see Figure in **Paper II**). By further increasing the temperature to 70 ℃, some hexapods began to appear (Figure 22a) which possibly produced with depressing of the {111} facet of octahedron similar to that of reported Ag_2O nanocrystals (Lyu et al., 2010). Moreover, when the reaction temperature increased to 100 ℃ in the absence of both VAM and CH₃COOH, complete octahedron shapes with an average size of 3.5-5.0 μm (Figure 22b-d) were obtained.

(a)   (b)

(c)   (d)
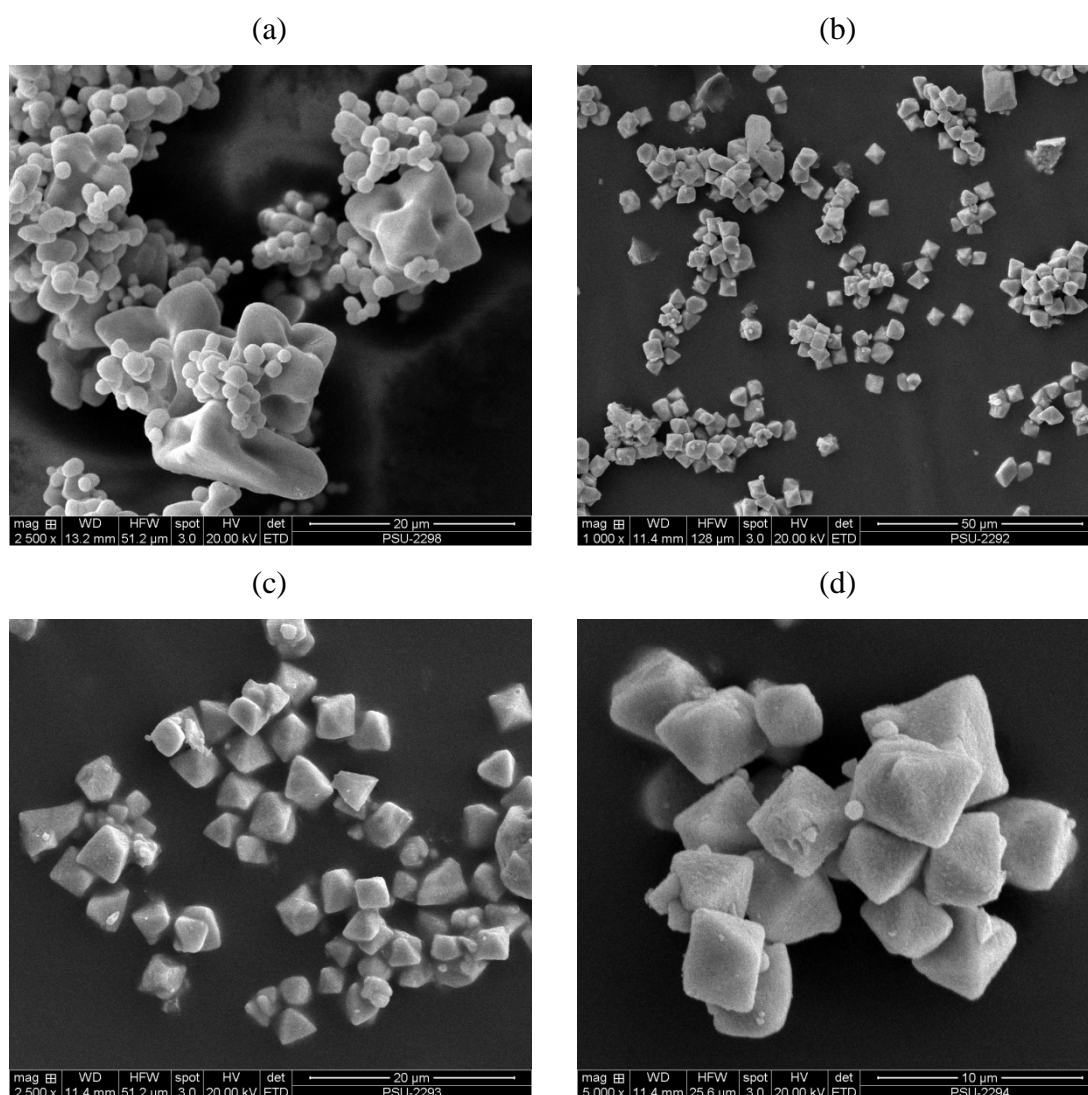
Figure 22 Hexapods with depressing of the {111} and octahedral shape.

3.4 Hexapods flower–like with sharp tips

On the addition of 10 mL of VAM but without CH_3COOH solution, the octahedron shapes could develop to hexapod flower-like structures with an average size of 10-12 μm as shown in Figure 23. Hexapod of flower-like AgCl grew from octahedron seeds along the ⟨100⟩ directions (Gatemala et al., 2014). Each leg of hexapod points to the vertex of an octahedron as shown in Figure 23d. This indicates that the morphologies of the AgCl crystals were controlled under the coorporation of the heat treatment and the additive reagents.

(a)   (b)

(c)   (d)
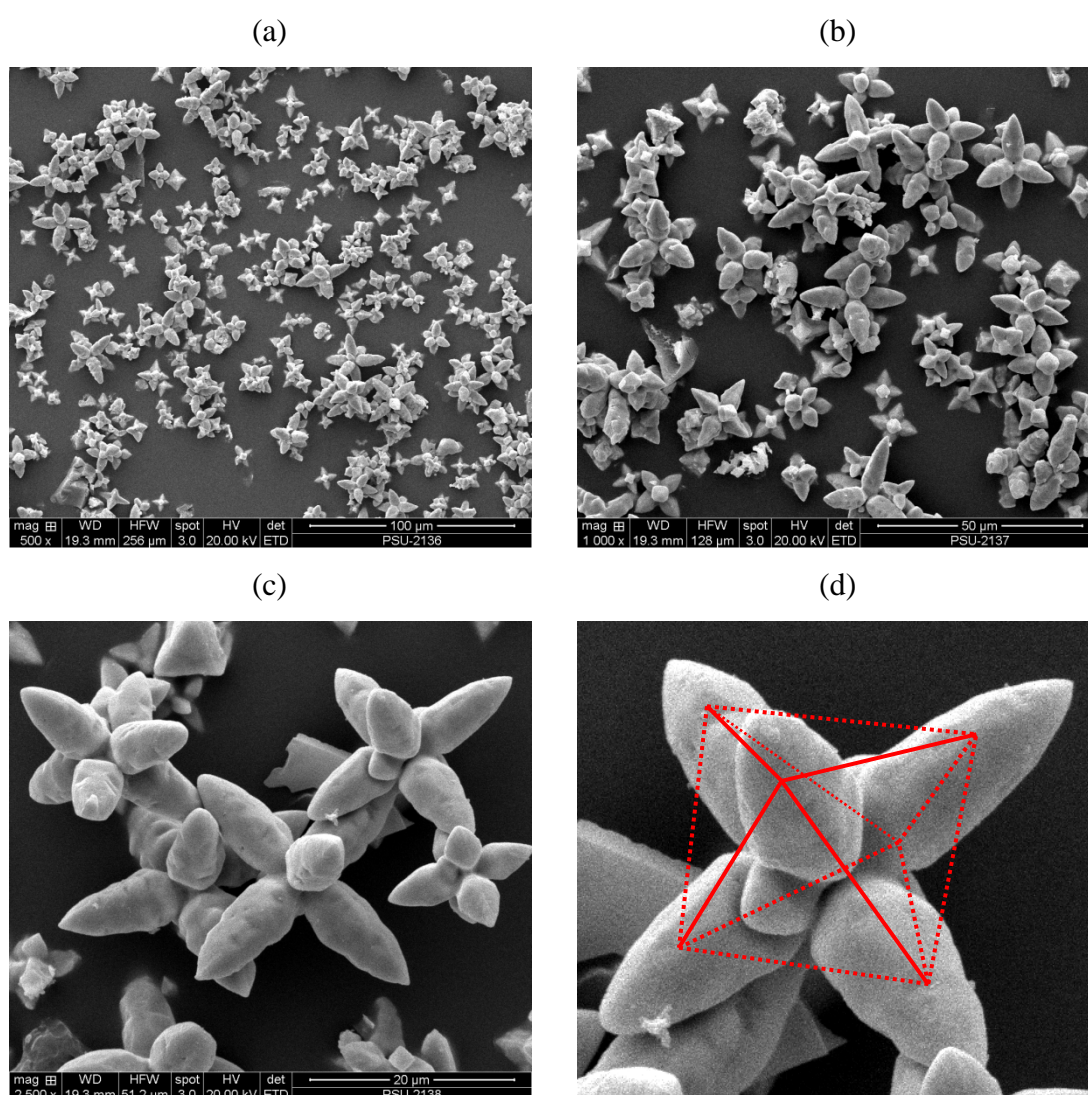
Figure 23 Hexapods flower-like with sharp tips**.**

3.5 Hexapods with small square pod and cactus-like shape

It is interesting that the changes in the reaction solution compositions resulted in different morphologies of the flowerlike Ag/AgCl. The hexapods with square tips with the average pod length of 5 μm and width of about 1 μm (Figure 24) were changed from hexapods with sharp pointed tips displayed in Figure 23 by reducing the concentration of 80 mL of 4.36 M CH$_3$COOH. The top facet of the pod is square of {100} facets as shown in Figure 24d supporting the expected growth habit of six cubic {100} facets of cubic seed. Some of the hexapods (in red circle, Figure 24b) have several pods grew out from the same site similar to the shape of flower-and cactus-like nanostructures found in ZnO and CdS (Kharissova and Kharisov, 2010).

(a) (b)

(c) {100} (d)
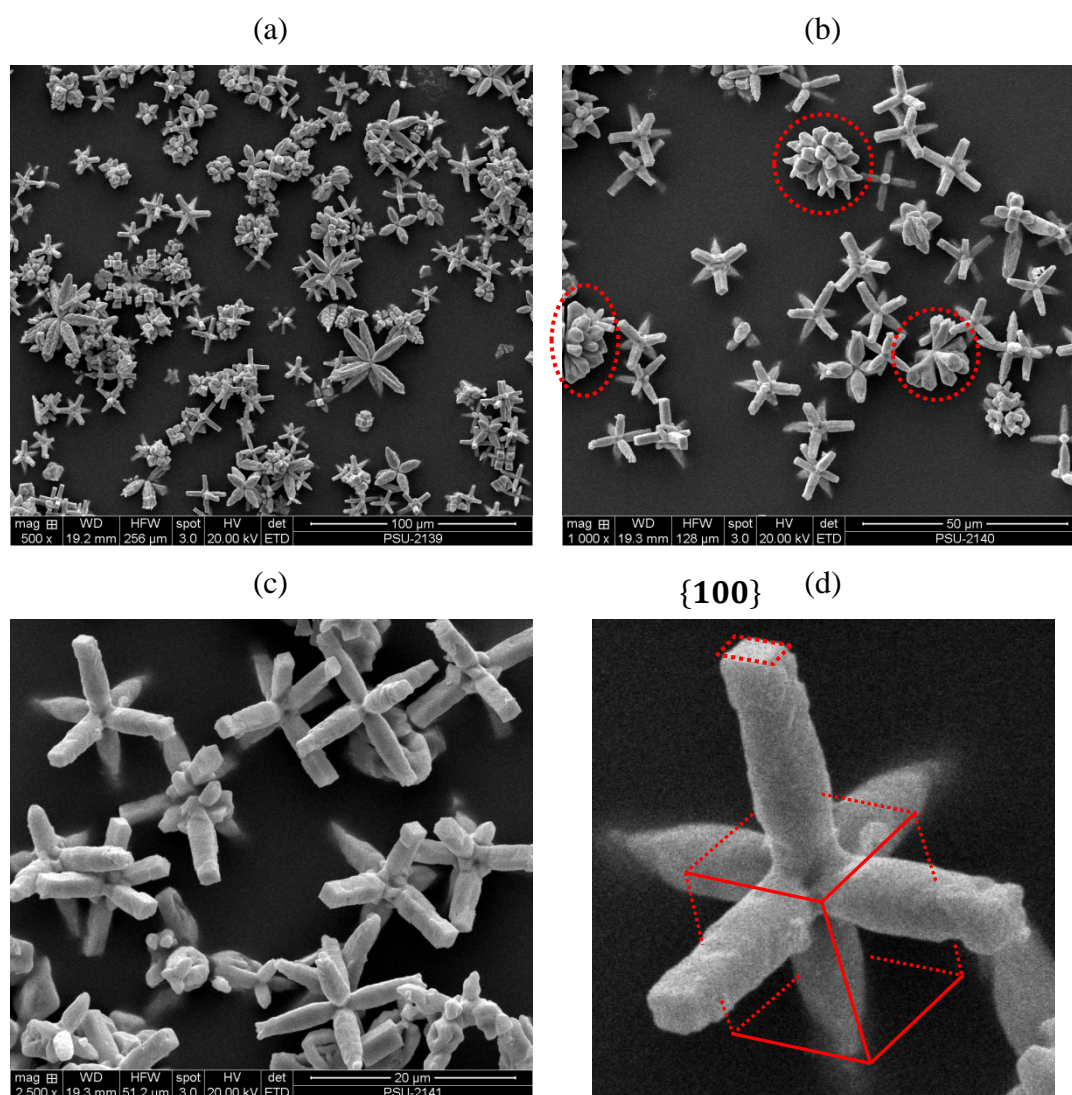
Figure 24 Hexapod flower-like with small square tips and cactus-like morphologies**.**

3.6 Hexapods with dagger-like pod

On further increasing the concentration of CH₃COOH to 13.07 M, hexapod with dagger-like pods were formed having mean diameter of 7 μm and length of 21 μm as shown in Figure 25a and b. In addition, a small amount of Rubik's cube-shaped coexisted with these hexapods. When the CH₃COOH concentration was increased to 16.34 M, the microflowers broke down remarkably. As shown in Figure 25b and d, these hexapod microstructures began to grow in almost every direction and the state of being highly ordered and controllable shape has been lost. More of dagger-like shape appeared at the expense of the microflowers. Clearly, this condition led to the collapse and breaking apart of the flower-like microstructure.

(a)   (b)

(c)   (d)
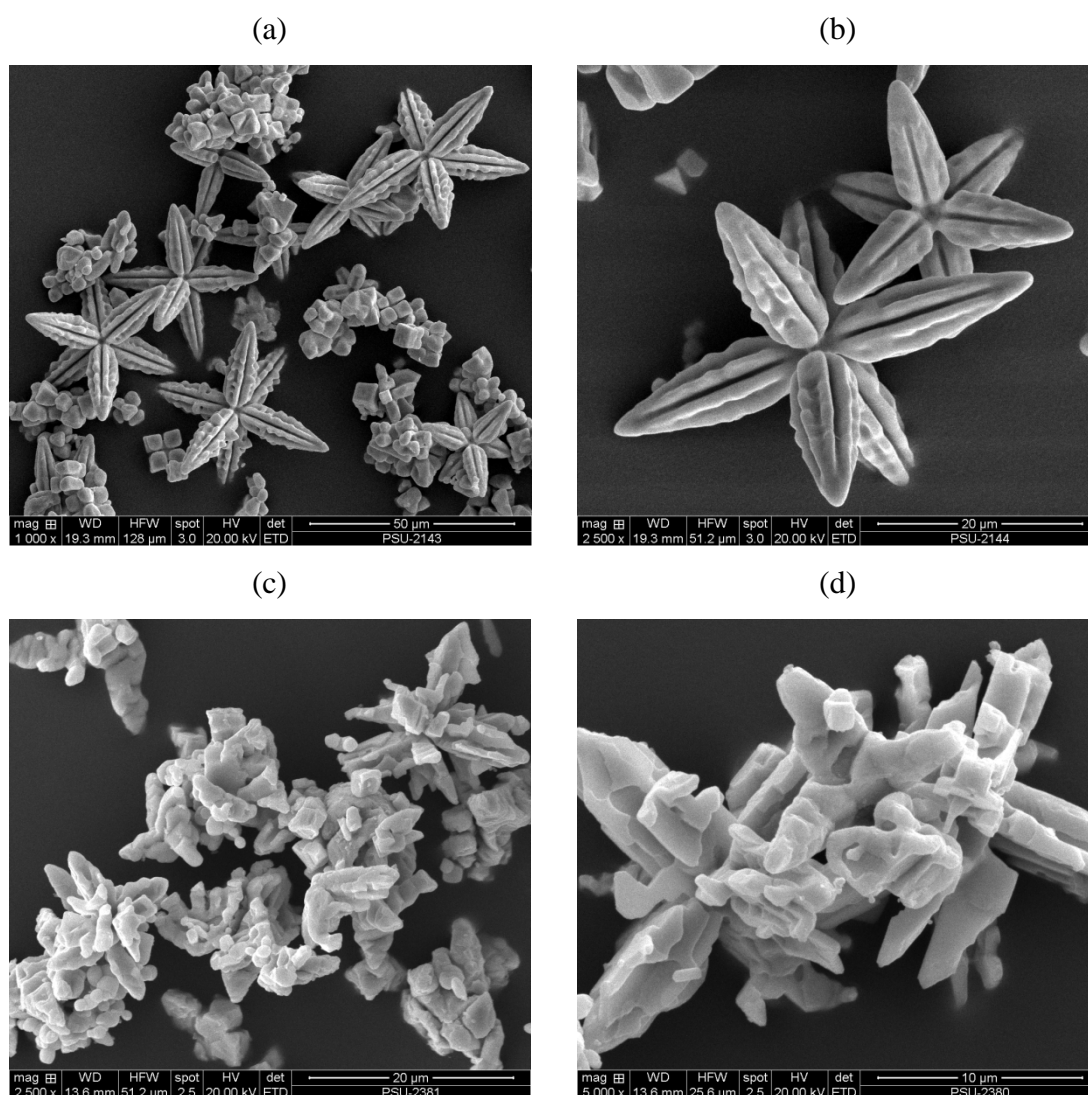
Figure 25 Hexapods with dagger-like pod and collapsed flower-like structures.

44

3.7 Octapod flower-like with leaf pods

    The amount of CH_3COOH was fixed at 80 mL of 8.72 M concentration, whereas VAM was reduced to 5 mL. The morphology still appeared like flower-like octapods with the crystal size of about 9 μm as shown in Figure 26. In this morphology, the eight petals inevitably grew out from the eight corners of cubic seed along the ⟨111⟩ directions (see Figure 26d).

(a)   (b)

(c)   (d)
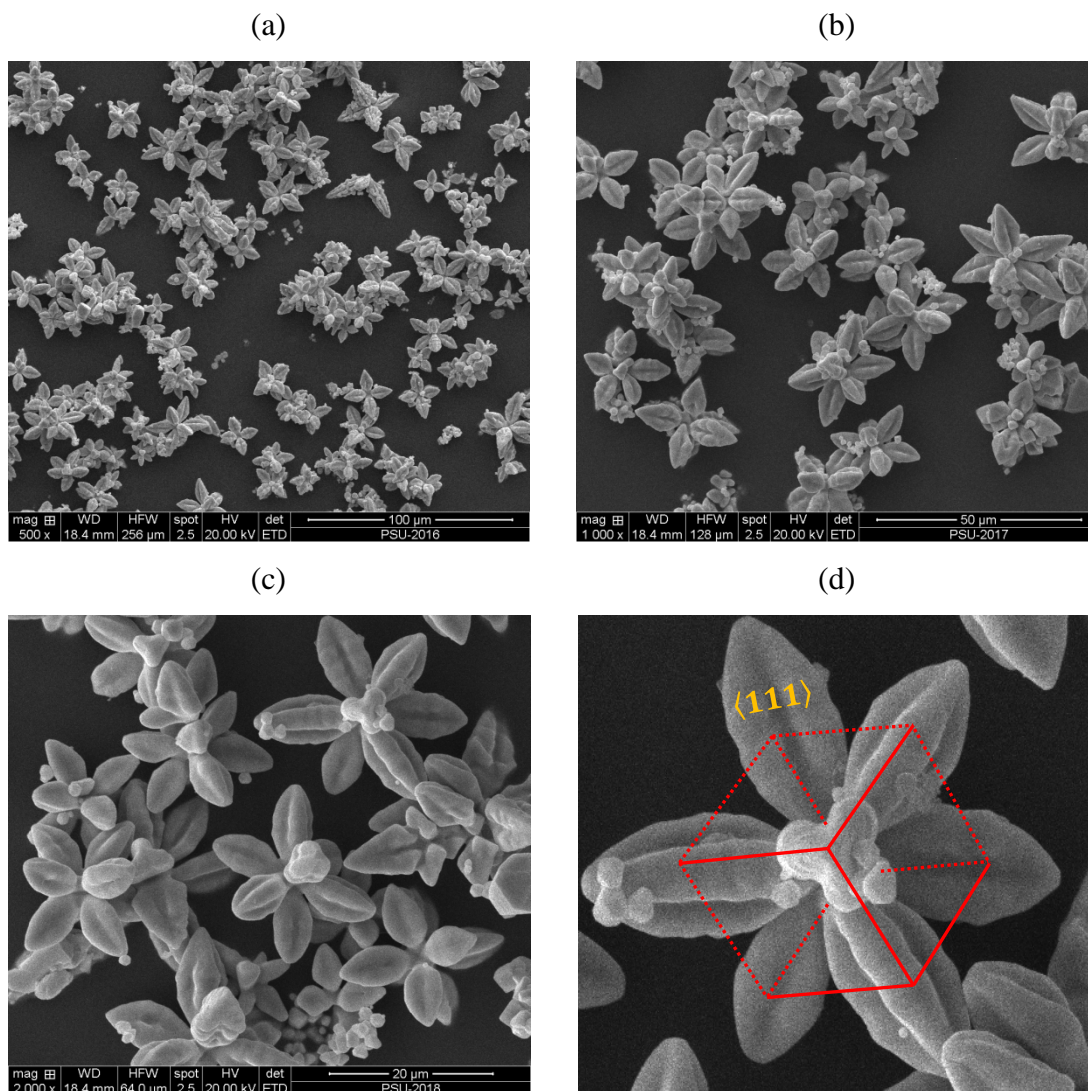
Figure 26 Octapod flower-like with leaf pods of different magnifications

3.8 Hexapod with large square pods

Hexapod with large {100} facet of square pods having an average pod length of *ca.* 6 μm and 2.5 μm of pod width was formed when increasing the amount of VAM to 15 mL as shown in Figure 27. Each pod has square top facet which shows the expected growth habit of six cubic {100} facets of cubic seed. This hexapod is very similar to-but the pod length and width are longer and larger than-those in Figure 24 above.

(a)   (b)

(c)   (d)
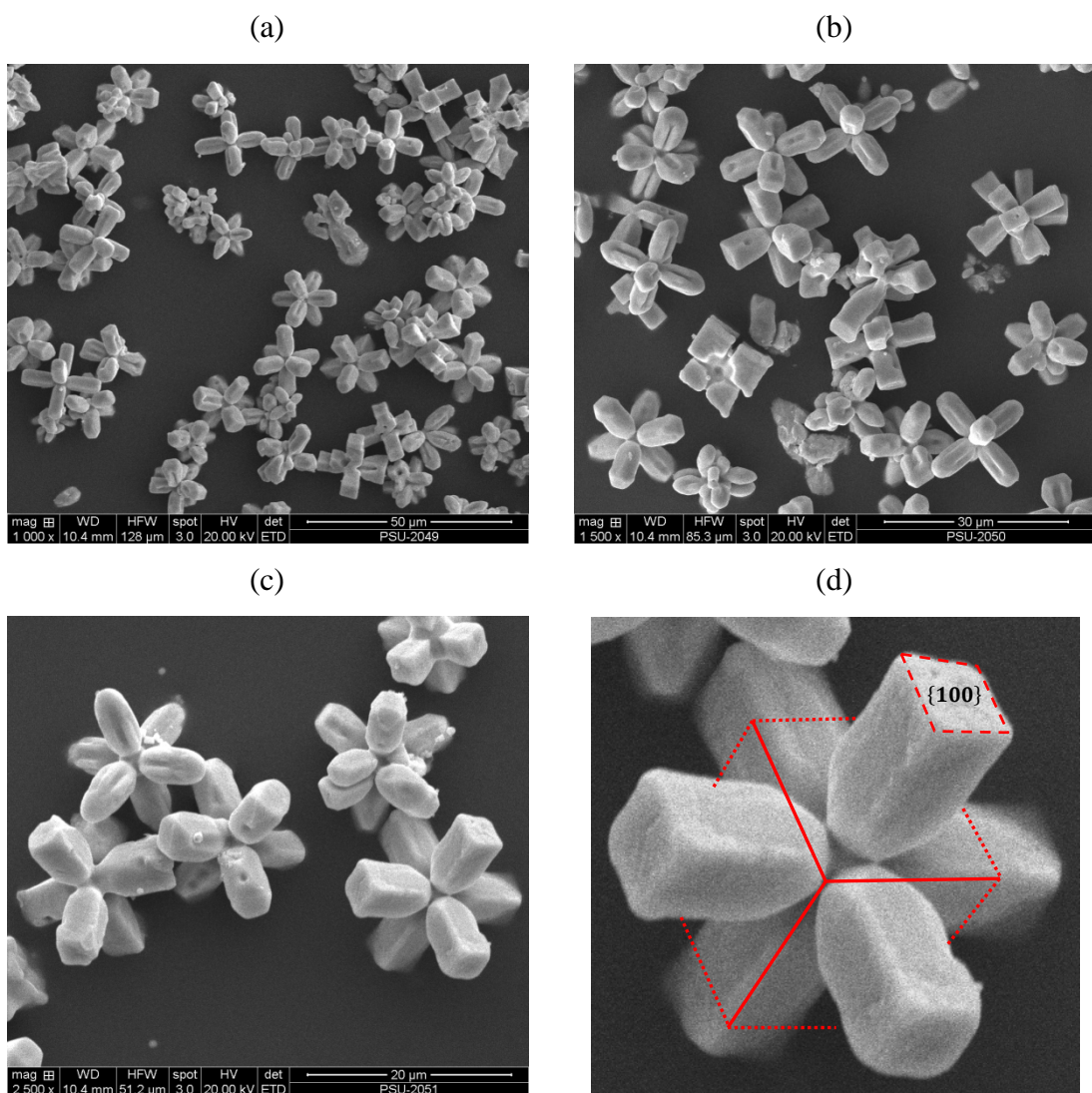
Figure 27 Hexapod with large square pods and growth habit of {100} facets of cubic seed

3.9 Flower–like with zeolite shape

The product appeared as the hierarchical flower–like particles with the average size about 17 μm, when 20 mL of VAM was used as shown by the SEM image in Figure 28. These flower-like displayed a noticeably transformed morphology, as the end of each pod now seemed to be capped with hollow structures of the zeolite shape.

(a)   (b)

(c)   (d)
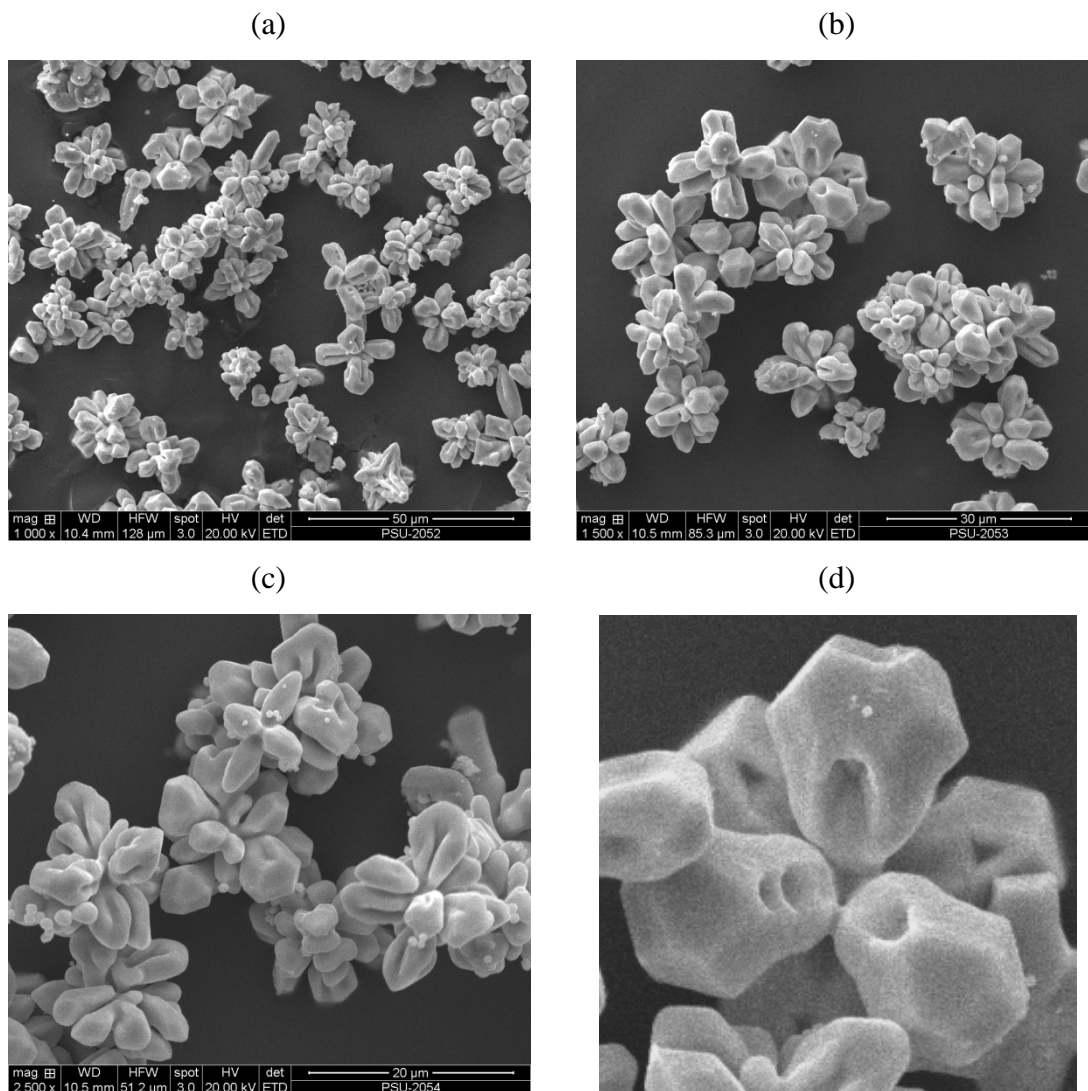
Figure 28 Flowerlike with zeolite shape of different magnifications.

3.10 Optical properties

Metallic Ag nanoparticles on the AgCl surface are able to absorb light in the visible range due to the absorption properties of surface plasmon resonance (SPR) (Xu et al., 2011). This absorption behavior corresponded with the observation reported by other researchers that it was originated from the characteristic absorption of surface plasmon resonance (SPR) of metallic Ag on the AgCl surface (Zhang et al., 2009; Han et al., 2011). Therefore, the absorption spectra in the visible range can be used to confirm the existence of metallic Ag (or Ag^0) in AgCl. The SPR band intensity and wavelength depend on the factors such as the metal type, shape, particle size, orientation, and contact area with the substrate (Pastoriza-santos et al., 2002; Mulvihill et al., 2010; Rycenga et al., 2011). In Table 3, the sample of urchin–like Ag/AgCl possesses two broad absorption peaks about 460 and 580 nm while the spherical shape of simple and cubic shape of commercial Ag/AgCl have one SPR absorption band around 550 nm. The samples of Rubik's cubes and irregular shape showed only one absorption peak located around 500 nm, which was attributed to SPR effect of Ag nanoparticles generated on the AgCl particle surfaces (Choi et al., 2010; J. Wang et al., 2009). Meanwhile, the octahedron one consisted of a strong absorption peak at 500 nm with a weak shoulder peak around 600 nm. For flower-like Ag/AgCl, a distinct peak at *ca*. 560 nm with a shoulder at *ca*. 470 nm was observed due to the relatively large sizes of these crystals. The positions of these bands exhibited a progressive red-shift of resonance peaks (from 470 to 560 nm) as particle size increases, which was caused by the growth of Ag particle size (Matsubara and Tatsuma, 2007; Zhang et al., 2011). In addition, metallic Ag nanoparticles on AgCl surface were clearly found in urchinlike and flower-like samples by XPS measurement. The binding energy of smaller doublet at 368.8 ($3d_{5/2}$), 374.8 ($3d_{3/2}$) of urchinlike sample and 368.5 ($3d_{5/2}$), 374.5 ($3d_{3/2}$) of flower-like powder were deconvoluted from the large area of Ag ion peak (Ag^I) could be assigned to the metallic Ag^0 (Dong et al., 2012; Zhu et al., 2012).

Table 3 Absorption peak and binding energy of metallic Ag in different AgCl morphologies.

Sample	Absorption peak[a] (nm)	Binding energy of Metallic Ag[b] (eV)
Urchinlike	460 (b), 580 (b)	368.8 ($3d_{5/2}$), 374.8 ($3d_{3/2}$)
Sphere (simple)	~ 550	NA
Cube (commercial)	~ 550	NA
Irregular	~ 500	–
Rubik's cube	~ 500	–
Octahedron	500 (s), 600 (w)	–
Flowerlike octapod	470 (w), 560 (s)	368.5 ($3d_{5/2}$), 374.5 ($3d_{3/2}$)

[a] is the data from DRS spectra, [b] the data from XPS spectra, – not measured, (b) broad, (s) strong, and (w) weak absorption peaks

The energy band gaps of different samples are calculated based on the optical absorption edge obtained from UV-vis DRS spectra by the Kubelka-Munk equation (Intarasuwan et al., 2013; Cao et al., 2011):

$$Rhv = A\left(hv - E_g\right)^{n/2} \qquad (35)$$

where R is the absorption coefficient, hv is the photon energy, A is a constant, E_g is band gap energy. Among them, n is determined by the type of optical transition of a semiconductor. The values of n for AgI, AgCl and TiO_2 are 1, 4 and 4 respectively (Liang et al. 2013). The absorption coefficient (R), at the corresponding wavelengths, can be calculated by the equation (Seoudi et al., 2010; Suwanboon et al., 2011):

$$R = \frac{A}{d'} \qquad (36)$$

Where A is the measured absorbance and d' is the path length of the quartz cuvette in a UV-vis cell which is equal to 0.4 cm.

According to Eq. (35) and (36), the indirect band gap energies were estimated from a plot of $(Rhv)^{1/2}$ versus hv. The curves with $(Rhv)^{1/2}$ as vertical axis and (hv) as horizontal axis can be obtained. The value of the intersection point where the tangent of the curve intersects with the (hv) axis is the band gap energy (Liang et al. 2013). Therefore, the estimated band gap energies of urchinlike and flower-like Ag/AgCl are 2.81 and 2.88 eV, respectively (Figure 29); this value agrees well with the reported band gap energy for AgCl (Hu et al. 2011). The investigated AgCl crystals showed a narrower band gap than that of the conventional AgCl crystals at 3.25 eV (Wang et al., 2014).

(a)   (b)
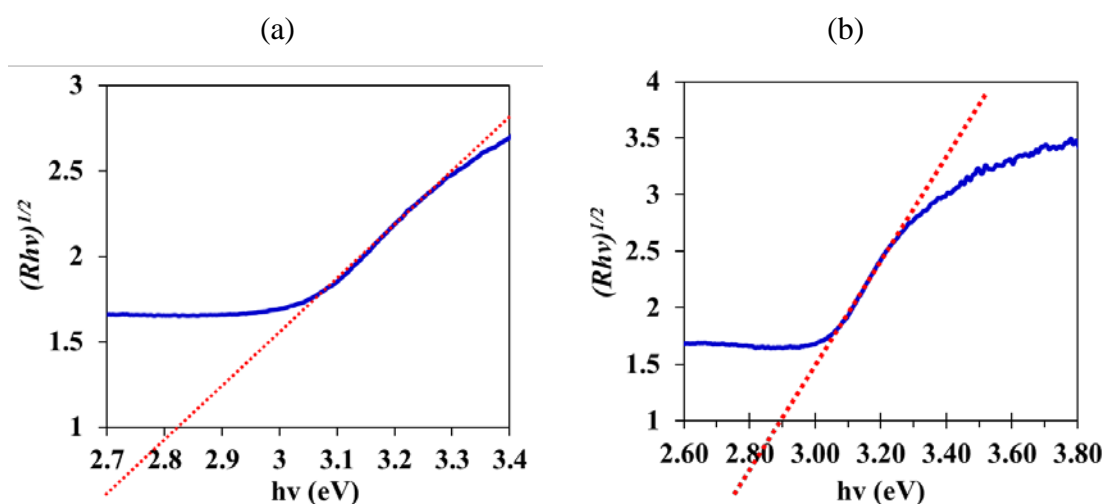
Figure 29 Determination of the band gap energy values for: (a) urchinlike and (b) flower-like Ag/AgCl samples.

3.11 AgCl photocatalyst

From the SEM and TEM images, urchinlike nanostructures showed the kernel covered with countless tiny nanohairs pointing outwardly. The peculiar hairy surface is useful to help adsorb the dye molecules. Meanwhile, flowerlike microstructures have a large number of atomic step, edges, and kinks generating larger reactive area. These characteristics exhibited higher the photocatalytic activity of urchinlike and flowerlike Ag/AgCl than that of commercial Degussa P25, commercial AgCl, and simple AgCl in discoloring orange G dye under UV and visible light irradiation as shown in Tables 4, 5, 6 of section 3.11.2.

3.11.1 Photocatalytic mechanism

The hypothesized pathways for the photocatalytic degradation of dye molecules (organic pollutants) by Ag/AgCl under UV and visible light irradiation were schematically illustrated in **Paper I** and reproduced as Figure 30. When AgCl absorbs photons from UV light with energy equal or greater than its band gap (3.25 eV), electrons in the valence band can be excited and jump up into the conduction band and leaving behind a hole in the valence band (Eq. (37)). The electron-hole pairs may recombine (Eq. (38)), or electron and hole may separate and finally be trapped as reduced Ag atom (Ag^0) (Eq. (39)), or Cl^0 atom (Eq. (41)). In general, the photogenerated electrons may also be trapped by O_2 in the solution to form superoxide ions (O_2^-) (Eq. (40)) which further transform to other reactive oxygen species. These active species also would degrade the dye molecules (Jiang and Zhang 2011). Despite this competing electron trapping reaction, however, the presence of metallic Ag atoms seem to indicate that the trapping of free electron by Ag^+ ions (Eq. (39)) located within the matrix may be the more favorable route. While the left over holes diffuse into the AgCl matrix to oxidize Cl^- ions to Cl atoms (Eq. (41)) which are very reactive for oxidizing species in the surrounding solution (Eq. (43)) (Dong et al., 2012).The hole may also oxidize the adsorbed OH^- at the interface to the powerful $^\bullet OH$ radical (Eq. (42)) which subsequently would undergo the dye degradation as well.

$$AgCl \xrightarrow{hv} AgCl + h^+ + e^- \tag{37}$$

$$h^+ + e^- \rightarrow kT \tag{38}$$

$$Ag^+ + e^- \rightarrow Ag^0 \tag{39}$$

$$O_2 + e^- \rightarrow O_2^- \tag{40}$$

$$Cl^- + h^+ \rightarrow Cl^0 \tag{41}$$

$$OH^- + h^+ \rightarrow OH^\bullet \tag{42}$$

$$Cl^0 + \text{organic compound} \rightarrow CO_2 + H_2O + Cl^- \tag{43}$$

$$OH^\bullet + \text{organic compound} \rightarrow CO_2 + H_2O \tag{44}$$
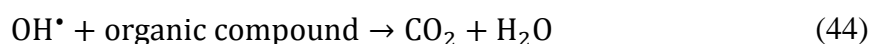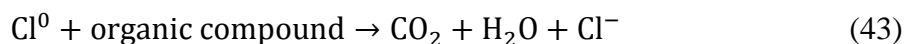
Under visible light irradiation, Ag metal nanoparticles absorb a photon from the visible light irradiation through the intrinsic SPR effect leading to electron-hole separation (Eq. (45)) (Xu et al. 2011; Calzaferri et al., 1999).
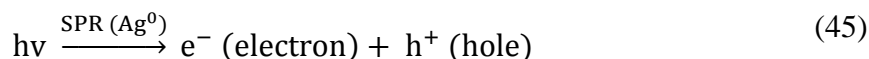
$$h\nu \xrightarrow{\text{SPR (Ag}^0)} e^- \text{ (electron)} + h^+ \text{ (hole)} \tag{45}$$

The holes eventually would react with Cl^- ions in the AgCl bulk leading to the formation of Cl^0 atoms (like Eq. (41) above) which go on to degrade the dye molecules (like Eq. (43) above) (Choi et al., 2010; Dong et al., 2012). Alternatively, the holes may also undergo the same fate as indicated in Eqs. (42) and (44). Simultaneously, the excited electrons are transferred to the conduction band of AgCl and trapped by the surface adsorbed molecular oxygen to form the active species of superoxide radical (Tang et al., 2013) (like Eq. (40) above). Another competing route is its trapping by Ag^+ in the matrix to form Ag^0 (like Eq. (39) above).

(a) Under UV light irradiation

(b) Under visible light irradiation
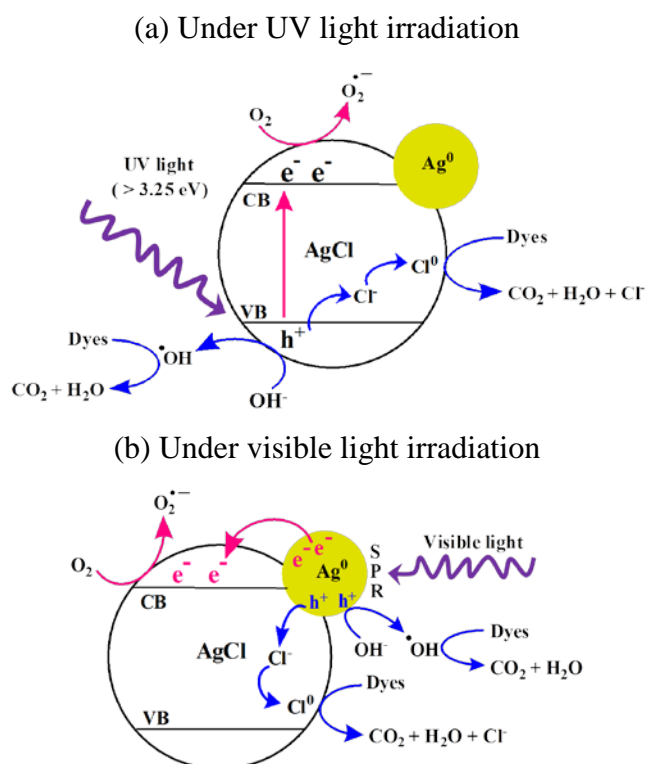
Figure 30 Schematic illustration of the Ag/AgCl photocatalytic degradation of organic pollutants under UV and visible light irradiation.

3.11.2 Kinetic study

The kinetics of photocatalytic degradation of organic compounds, or OG in our study, usually follows the Langmuir-Hinshelwood kinetic as

$$ln\left(\frac{C_0}{C_t}\right) = kt \tag{46}$$

where k is the apparent pseudo-first order rate constant given by the slope of the graph of ln C_0/C_t versus t and C_0 is the initial concentration of OG dye and C_t is the concentration of OG at time t (Liang et al., 2013; Gaya and Abdullah, 2008).

The observed rate constant and correlation coefficient of urchinlike, flowerlike, and their comparative sample are given in Table 4-6. The kinetic data of these samples were plotted using equation (46) showing good straight lines as shown in Appendix C mean that all samples showed pseudo-first order behavior. Under UV light photoreaction, the rate constant (k) of the urchinlike Ag/AgCl was determined as 0.0322 min^{-1}, which was almost four times and over ten times higher than those of simple Ag/AgCl (0.0088 min^{-1}) and commercial Ag/AgCl (0.0014 min^{-1}), respectively as shown in Table 4. Under visible light, the rate constant of both urchinlike and flower-like Ag/AgCl still larger than those of simple and commercial Ag/AgCl as shown in Table 5 and 6, respectively.

Table 4 The pseudo-first order kinetic apparent rate constant and correlation factor values for the photodegradation of orange G dye by UV light of the three catalysts, [Orange G]$_0$ = 5.0 ×10^{-5} M

Different AgCl samples	Orange G degradation, % (120 min)	Reaction constant, k (min^{-1})	Correlation coefficient, R^2
Urchinlike	100	0.0322	0.9678
Simple	63	0.0088	0.9799
Commercial	15	0.0014	0.9496

Table 5 The pseudo-first order kinetic apparent rate constant and correlation factor values for the photodegradation of orange G dye by visible light of the three catalysts, [Orange G]$_0$ = 5.0×10^{-5} M.

Different AgCl samples	Orange G degradation, % (5 h)	Reaction constant, k (h^{-1})	Correlation coefficient, R^2
Urchinlike	100	1.1380	0.9601
Simple	21	0.0498	0.9862
Commercial	4	0.0106	0.5923

Table 6 The pseudo-first order kinetic apparent rate constant and correlation factor values for the photodegradation of orange G dye by visible light of the three catalysts, [Orange G]$_0$ = 2.5×10^{-5} M.

Different AgCl samples	Orange G degradation, % (240 min)	Reaction constant, k (min^{-1})	Correlation coefficient, R^2
Flower–like	100	0.0206	0.9722
Simple	73	0.0060	0.9480
Commercial	47	0.0026	0.9870

3.11.3 Recyclability

In the recycle test, urchinlike Ag/AgCl catalyst powder was reused directly again (after separation without washing) with fresh dye solution. Meanwhile, the recovered flower-like Ag/AgCl had to be washed with DI water and dried at 40 ºC for about 6 h. From Table 7, the results of four times of recycle uses between the two methods were not significantly different. The degradation efficiencies of both catalysts gradually decreased in the recycle uses could be due to the increasing amount of metallic Ag^0 formation as evidenced in XRD of urchinlike (Daupor and Wongnawa, 2014). This means the catalyst can be used comfortably three times

before being replaced with new fresh catalyst. It should be pointed out that our results here correspond to both the number of uses and the trend of slightly decreasing in efficiency in the recycling uses of Ag/AgCl catalyst appearing in several reports (Lou et al., 2011; B. Ma et al., 2013; Tang et al., 2013; Zhu et al., 2011). The data in some of these reports (Lou et al., 2011; Ma et al., 2013) were clearly similar to the one shown in Table 7. It seems that if the concentration of metallic Ag is too high beyond its critical value it may give the negative effect. The drastic increase of Ag^0 may cover the surface of AgCl preventing it to receive UV light effectively or the layer of Ag^0 may become too thick such that the free electron and hole may not effectively reach the AgCl bulk to drive further reaction.

Table 7 Degradation efficiency variation with number of use

Sample	Degradation (%)			
	1st	2nd	3rd	4th
Urchinlike (UV light)	100	98	88	70
Urchinlike (visible light)	100	96	85	64
Flower–like (visible light)	100	98	86	70

4. Concluding remarks

In summary, urchinlike Ag/AgCl was successfully synthesized by forced hydrolysis of TiCl$_4$ precursor which has some effect on the growth of nanohairs. Although TiCl$_4$ did not show up in the final product, amorphous and rutile TiO$_2$ was obtained before AgCl precipitated. The countless tiny hairs surface is useful to help adsorb the dye molecules leading to the excellence photocatalytic activity. In addition, we have also successfully prepared flower-like Ag/AgCl with evidence that it directly grew along in the order: concave cube, octapod, and Rubik's cube structure, in which VAM acted as controlling agent by selective adsorption on the {100} facets leading to preferential addition of Ag and Cl atoms to the {111} facets. The flower-like octapod Ag/AgCl was grown as long as micrometer of petals and grew along ⟨111⟩ directions of cubic seed as shown in the Scheme 2a. The amount of reactants and temperature played an important role in the formation of different morphologies of AgCl microcrystals. The hexapod with sharp pods grew along ⟨100⟩ direction of octahedron seed (Scheme 2c), whereas the hexapod with square pods grew from cubic seed along the ⟨100⟩ direction as shown in Scheme 2b. In this present work, the Ag$^+$ ion was reduced to Ag^0 atom without any addition of reducing agents and calcination treatments as have been reported by other researchers. The obtained product, referred to as urchinlike and flower-like Ag/AgCl, exhibited higher photocatalytic activity than that of commercial Degussa P25, commercial AgCl, and simple AgCl in discoloring orange G dye under UV and visible light irradiation.

56
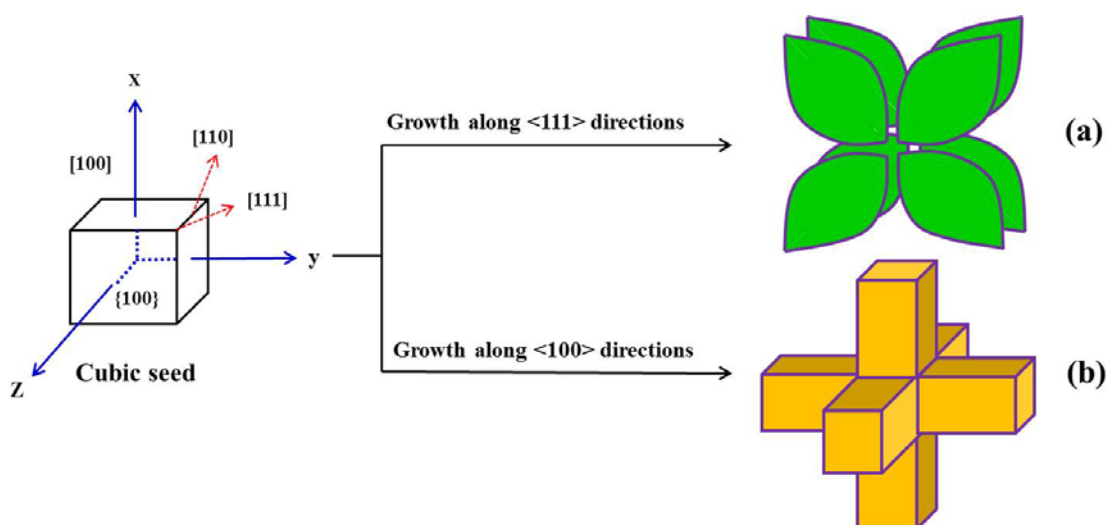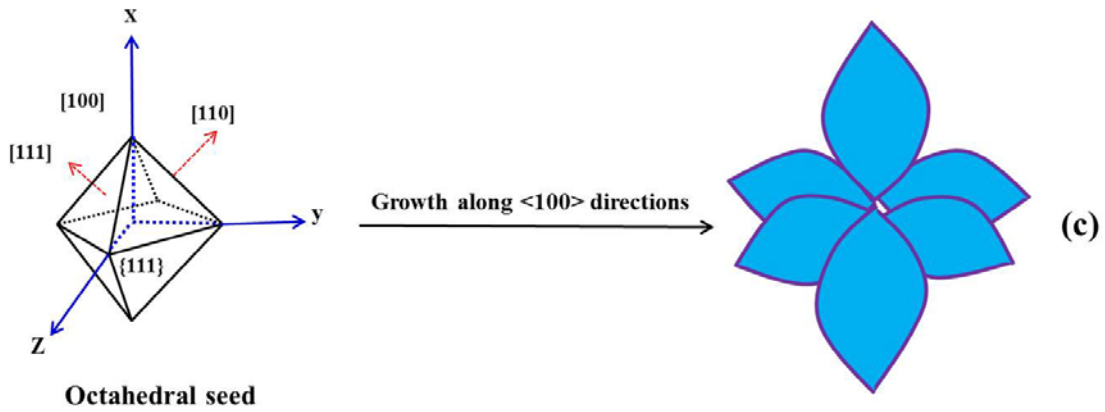
Scheme 2 Morphologies related to growth from different direction of crystal seed: (a) octapod growth along ⟨111⟩ direction of cubic seed, (b) hexapod growth from ⟨100⟩ direction of cubic seed, and (c) hexapod growth along ⟨100⟩ direction of octahedron seed.

REFERENCES

An, C., Wang, R., Wang, S., and Zhang, X. 2011. Converting AgCl nanocubes to sunlight-driven plasmonic AgCl : Ag nanophotocatalyst with high activity and durability. *Journal of Materials Chemistry*, **21**(31), 11532.

Akhmetov, N. S., and Rosinkin, A. 1983. General and Inorganic Chemistry. Moscow Mir Pub.

Baiju, K. V, Shukla, S., Sandhya, K. S., James, J., and Warrier, K. G. K. 2007. Photocatalytic Activity of Sol-Gel-Derived Nanocrystalline Titania, *The Journal of Physical Chemistry C*, **111**, 7612-7622.

Bi, Y., and Ye, J. 2009. In situ oxidation synthesis of Ag/AgCl core-shell nanowires and their photocatalytic properties. *Chemical Communications*, (43), 6551–6553.

Brandon, D., and Kaplan, W. D. 1999. Microstructural Characterization of Materials. John Wiley & Sons: England.

Burda, C., Chen, X., Narayanan, R., and El-Sayed, M. A. 2005. Chemistry and properties of nanocrystals of different shapes. *Chemical Reviews*, **105**, 1025-1102.

Calzaferri, G., Lanz, M., and Schu, D. 1999. Photocatalytic oxidation of water to O_2 on AgCl-coated electrodes, *Journal of Photochemistry and Photobiology A: Chemistry,* **120**, 105-117.

Cao, G. 2004. Nanostructures and Nanomaterials: Synthesis, Properties and Applications. Imperial College Press: London.

Cao, J., Xu, B., Luo, B., Lin, H., and Chen, S. 2011. Preparation, characterization and visible-light photocatalytic activity of AgI/AgCl/TiO_2. *Applied Surface Science*, **257**(16), 7083-7089.

58

Chen, D., Liu, M., Chen, Q., Ge, L., Fan, B., Wang, H., Lu, H., Yand, D., Zhang, R., Yan, Q., Shao, G., Sun, J., and Gao, L. 2014. Large-scale synthesis and enhanced visible-light-driven photocatalytic performance of hierarchical Ag/AgCl nanocrystals derived from freeze-dried PVP–Ag$^+$ hybrid precursors with porosity. *Applied Catalysis B: Environmental*, **144**, 394-407.

Chen, H., Xiao, L., and Huang, J. 2014. Template synthesis of Ag/AgCl microrods and their efficient visible light-driven photocatalytic performance. *Materials Research Bulletin*, **57**, 35-40.

Chiu, C.-K., Choi, Y.-J., and Luo, T.-J. M. 2012. Formation of AgCl Cubic Crystals Induced by Shrinkage of Sol–Gel Silica Film. *Crystal Growth & Design*, **12**(10), 4727-4732.

Choi, M., Shin, K.-H., and Jang, J. 2010. Plasmonic photocatalytic system using silver chloride/silver nanostructures under visible light. *Journal of Colloid and Interface Science*, **341**(1), 83-87.

Cotton, A. 1999. Advanced Inorganic Chemistry. 6th Ed. John Wiley & Sons: New York.

Cui, F., Yu, N., Wang, Z., Zhai, M., and Wu, K. 2014. Conversion of AgCl nanocubes to Ag/AgCl nanohybrids via solid–liquid reaction for surface-enhanced Raman scattering detection. *Micro & Nano Letters*, **9**(5), 297-301.

Daupor, H., and Sumpun, W. 2014. "Urchinlike Ag/AgCl Photocatalyst: Synthesis, Characterization, and Activity." *Applied Catalysis A: General*, **473**, 59-69.

Dong, L., Liang, D., and Gong, R. 2012. In Situ Photoactivated AgCl/Ag Nanocomposites with Enhanced Visible Light Photocatalytic and Antibacterial Activity. *European Journal of Inorganic Chemistry*, (19), 3200-3208.

Dong, R., Tian, B., Zeng, C., Li, T., Wang, T., and Zhang, J. 2012. Ecofriendly Synthesis and Photocatalytic Activity of Uniform Cubic Ag @ AgCl Plasmonic Photocatalyst. *The Journal of Physical Chemistry C*, **117**, 213-220.

Dong, X., Ji, X., Wu, H., Zhao, L., Li, J., and Yang, W. 2009. Shape Control of Silver Nanoparticles by Stepwise Citrate Reduction. *The Journal of Physical Chemistry C*, **113**(16), 6573-6576.

El-Sayed, M. A. 2001. Some interesting properties of metals confined in time and nanometer space of different shapes. *Accounts of Chemical Research*, **34**(4), 257-264.

Fahlman, B. D. 2007. Materials Chemistry. Springer: Dordrecht.

Fujishima, A., Rao, T. N., and Tryk, D. A. 2000. Titanium dioxide photocatalysis, *Journal of Photochemistry and Photobiology C: Photochemistry Reviews,* **1**, 1-21.

Gatemala, H., Thammacharoen, C., and Ekgasit, S. 2014. 3D AgCl microstructures selectively fabricated via Cl^--induced precipitation from $[Ag(NH_3)_2]^+$. *Cryst Eng Comm*, **16**(29), 6688.

Gaya, U. I., and Abdullah, A. H. 2008. Heterogeneous photocatalytic degradation of organic contaminants over titanium dioxide: A review of fundamentals, progress and problems. *Journal of Photochemistry and Photobiology C: Photochemistry Reviews*, **9**(1), 1-12.

Ghosh, S. K., and Pal, T. 2007. Interparticle coupling effect on the surface plasmon resonance of gold nanoparticles: from theory to applications. *Chemical Reviews*, **107**(11), 4797-862.

Glaus, S., and Calzaferri, G. 1999. Silver Chloride Clusters and Surface States. *The Journal of Physical Chemistry B*, **103**(27), 5622-5630.

60

Glusker, J. P., Lewis, M., and Rossi, M. 1994. Crystal Structure Ananlysis for Chemists and Biologists. VCH: Philadelphia.

Gomathi Devi, L., and Mohan Reddy, K. 2011. Photocatalytic performance of silver TiO$_2$: Role of electronic energy levels. *Applied Surface Science*, **257**(15), 6821-6828.

Hammond, C. 1990. Introduction to Crystallography. Oxford University Press: New York.

Han, L., Wang, P., Zhu, C., Zhai, Y., and Dong, S. 2011. Facile solvothermal synthesis of cube-like Ag@AgCl: a highly efficient visible light photocatalyst. *Nanoscale*, **3**(7), 2931-2935.

Hao, F., Nehl, C. L., Hafner, J. H., and Nordlander, P. 2007. Plasmon resonances of a gold nanostar. *Nano Letters*, **7**(3), 729-732.

Hoffmann, M. R., Martin, S. T., Choi, W., and Bahnemannt, D. W. 1995. Environmental Applications of Semiconductor Photocatalysis, *Chemical Reviews,* **95**, 69-96.

Hornyak, G. L., Tibbals, H. F., Dutta, J., and Moore, J. J. 2009. Introduction to Nanoscience & Nanotechnology. CRC Press: Boca Raton.

Hu, J., Jia, N., Jiang, J.-X., Ma, M.-G., Zhu, J.-F., Sun, R.-C., and Li, J.-Z. 2011. Hydrothermal preparation of boehmite-doped AgCl nanocubes and their characterization. *Materials Letters*, **65**(11), 1531-1534.

Huheey, J. E., Keiter, E. A., and Keiter, R. L. 1993. Inorganic Chemistry. 4th Ed. Harper Collins College: New York.

Intarasuwan, K., Amornpitoksuk, P., and Suwanboon, S. 2013. Effect of the mixing rate on the morphology and photocatalytic activity of ZnO powders prepared by a precipitation method. *Advanced Powder Technology*, **24**(6), 999-1005.

Jakob, M., Levanon, H., and Dame, N. 2003. Charge Distribution between UV-Irradiated TiO_2 and Gold Nanoparticles : Determination of Shift in the Fermi Level. *Nano Letters*, **3**, 353-358.

Jana, N. R., Gearheart, L., and Murphy, C. J. 2001. Wet Chemical Synthesis of High Aspect Ratio Cylindrical Gold Nanorods. *The Journal of Physical Chemistry B*, **105**(19), 4065-4067.

Jiang, J., and Zhang, L. 2011. Rapid microwave-assisted nonaqueous synthesis and growth mechanism of AgCl/Ag, and its daylight-driven plasmonic photocatalysis. *Chemical Europian Journal*, **17**(13), 3710-3717.

Jones, M. R., Osberg, K. D., Macfarlane, R. J., Langille, M. R., and Mirkin, C. a. 2011. Templated techniques for the synthesis and assembly of plasmonic nanostructures. *Chemical Reviews*, **111**(6), 3736-827.

Kanna, M. 2002. Adsorption Behavior of Some Metal Ions on Titanium Dioxide Surface. Master of Science Thesis, Prince of Songkla University, Songkhla, Thailand.

Kelsall, R. W., Hamley, I. W., and Geoghegan, M. 2005. Nanoscale Science and Technology. John Wiley & Sons: Chichester.

Kharissova, O. V., and Kharisov, B. I. 2010. Less-Common Nanostructures in the Forms of Vegetation. *Industrial & Engineering Chemistry Research*, **49**(22), 11142-11169.

Khataee, R., Pons, M. N., and Zahraa, O. 2009. Photocatalytic degradation of three azo dyes using immobilized TiO_2 nanoparticles on glass plates activated by UV light irradiation: influence of dye molecular structure. *Journal of Hazardous Materials*, **168**(1), 451-457.

62

Kim, S.-W., Chung, H.-E., Kwon, J.-H., Yoon, H.-G., and Kim, W. 2010. Facile Synthesis of Silver Chloride Nanocubes and Their Derivatives. *Bulletin of the Korean Chemical Society*, **31**(10), 2918-2922.

Klosek, S., and Raftery, D. 2001. Visible Light Driven V-Doped TiO_2 Photocatalyst and Its Photooxidation of Ethanol, *Journal of Physicals Chemistry: B*, **105**, 2815-2819.

Konstantinou, I. K., and Albanis, T. A. 2004. TiO_2-assisted photocatalytic degradation of azo dyes in aqueous solution: kinetic and mechanistic investigations. *Applied Catalysis B: Environmental*, **49**(1), 1-14.

Lachheb, H., Puzenat, E., Houas, A., Ksibi, M., Elaloui, E., Guillard, C., and Herrmann, J.-M. 2002. Photocatalytic degradation of various types of dyes (Alizarin S, Crocein Orange G, Methyl Red, Congo Red, Methylene Blue) in water by UV-irradiated titania. *Applied Catalysis B: Environmental*, **39**(1), 75-90.

Li, F. B., and Li, X. Z. 2002. The enhancement of photodegradation efficiency using Pt – TiO_2 catalyst, *Chemosphere,* **48**, 1103-1111.

Li, M., Yu, H., Huang, R., Bai, F., Trevor, M., Song, D., Jiang, B., and Li, Y. 2013. Facile one-pot synthesis of flower-like AgCl microstructures and enhancing of visible light photocatalysis. *Nanoscale Research Letters*, **8**(1), 442.

Li, Y., and Ding, Y. 2010. Porous AgCl/Ag Nanocomposites with Enhanced Visible Light Photocatalytic Properties. *The Journal of Physical Chemistry C*, **114**(7), 3175-3179.

Liang, Q., Shi, Y., Ma, W., Li, Z., and Yang, X. 2013. Large-scale preparation and morphology-dependent photodegradation performances of monodispersed AgBr crystals. *Applied Catalysis A: General*, **455**, 199-205.

Liao, J., Zhang, K., Wang, L., Wang, W., Wang, Y., Xiao, J., and Yu, L. 2012. Facile hydrothermal synthesis of heart-like Ag@AgCl with enhanced visible light photocatalytic performance. *Materials Letters*, **83**, 136-139.

Lim, B., and Xia, Y. 2011. Metal nanocrystals with highly branched morphologies. *Angewandte Chemie International Edition*, **50**(1), 76-85.

Logar, M., Jancar, B., Sturm, S., and Suvorov, D. 2010. Weak polyion multilayer-assisted in situ synthesis as a route toward a plasmonic Ag/TiO_2 photocatalyst. *Langmuir : The ACS Journal of Surfaces and Colloids*, **26**(14), 12215-12224.

Lou, Z., Huang, B., Ma, X., Zhang, X., Qin, X., Wang, Z., Dai, Y., and Liu, Y. 2012. A 3D AgCl hierarchical superstructure synthesized by a wet chemical oxidation method. *Chemical European Journal*, **18**(50), 16090-16096.

Lou, Z., Huang, B., Qin, X., Zhang, X., Cheng, H., Liu, Y., Wang, S., Wang, J., and Dai, Y. 2012. One-step synthesis of AgCl concave cubes by preferential overgrowth along <111> and <110> directions. *Chemical Communications*, **48**(29), 3488-3490.

Lou, Z., Huang, B., Wang, P., Wang, Z., Qin, X., Zhang, X., Cheng, H., Zheng, Z., and Dai, Y. 2011. The synthesis of the near-spherical AgCl crystal for visible light photocatalytic applications. *Dalton Transactions*, **40**(16), 4104-4110.

Lou, Z., Huang, B., Wang, Z., Qin, X., Zhang, X., Liu, Y., Zhang, R., Dai, Y., and Whangbo, M.-H. 2013. Interface kinetic diffusion reaction leading to fast and continuous generation of AgCl nanocubes in NaCl solution. *Dalton Transactions*, **42**, 15219-15225.

Lu, Y. H., Sit, P., Hung, T. F., Chen, H., Zhou, Z. F., Li, K. Y., and Shen, Y. G. 2005. Effects of B content on microstructure and mechanical properties of nanocomposite $Ti-B_x-N_y$ thin films. *Journal of Vacuum Science & Technology B: Microelectronics and Nanometer Structures*, **23**(2), 449-457.

64

Luo, X., Li, Z., Yuan, C., and Chen, Y. 2011. Polyol synthesis of silver nanoplates: The crystal growth mechanism based on a rivalrous adsorption. *Materials Chemistry and Physics*, **128**(1-2), 77-82.

Lyu, L.-M., Wang, W.-C., and Huang, M. H. 2010. Synthesis of Ag$_2$O nanocrystals with systematic shape evolution from cubic to hexapod structures and their surface properties. *Chemical European Journal*, **16**(47), 14167-14174.

Ma, B., Guo, J., Dai, W.-L., and Fan, K. 2013. Highly stable and efficient Ag/AgCl core–shell sphere: Controllable synthesis, characterization, and photocatalytic application. *Applied Catalysis B: Environmental*, **130-131**, 257-263.

Ma, X., Dai, Y., Lu, J., Guo, M., and Huang, B. 2012. Tuning of the Surface-Exposing and Photocatalytic Activity for AgX (X = Cl and Br): A Theoretical Study. *The Journal of Physical Chemistry C*, **116**(36), 19372-19378.

Matsubara, K., and Tatsuma, T. 2007. Morphological Changes and Multicolor Photochromism of Ag Nanoparticles Deposited on Single-crystalline TiO$_2$ Surfaces. *Advanced Materials*, **19**(19), 2802-2806.

Meetani, M. A., Rauf, M. A., Hisaindee, S., Khaleel, A., AlZamly, A., and Ahmad, A. 2011. Mechanistic studies of photoinduced degradation of Orange G using LC/MS. *RSC Advances*, **1**(3), 490.

Melghit, K., Al-Shukeili, O. S., and Al-Amri, I. 2009. Effect of M-doping (M=Fe, V) on the photocatalytic activity of nanorod rutile TiO$_2$ for Congo red degradation under the sunlight. *Ceramics International*, **35**(1), 433-439.

Mulvihill, M. J., Ling, X. Y., Henzie, J., Yang, P., V, S. Di, and Berkeley, L. 2010. Anisotropic Etching of Silver Nanoparticles for Plasmonic Structures Capable of Single-Particle SERS, *Journal of American Chemical Society*, **132**(19), 268-274.

Muthukumar, M., Karuppiah, M. T., and Raju, G. B. 2007. Electrochemical removal of CI Acid orange 10 from aqueous solutions. *Separation and Purification Technology*, **55**(2), 198-205.

Neamen, D. A. 2003. Semiconductor Physics and Devices. 3th Ed. McGraw-Hill: Boston.

Nguyen, V. K., and Vu, T. H. 2012. Synthesis of AgCl/Ag nanopowder and its application in photodegradation of methylene blue. *Advances in Natural Sciences: Nanoscience and Nanotechnology*, **3**(2), 025012.

Ni, Y., Liu, H., Wang, F., Liang, Y., Hong, J., Xiang Ma, X., and Xu, Z. 2004. PbS crystals with clover-like structure: Preparation, characterization, optical properties and influencing factors. *Crystal Research and Technology*, **39**(3) 200-206.

Niu, W., Li, Z.-Y., Shi, L., Liu, X., Li, H., Han, S., Chen, J., and Xu, G. 2008. Seed-Mediated Growth of Nearly Monodisperse Palladium Nanocubes with Controllable Sizes. *Crystal Growth & Design*, **8**(12), 4440-4444.

Noguez, C. 2007. Surface Plasmons on Metal Nanoparticles: The Influence of Shape and Physical Environment. *Journal of Physical Chemistry C*, **111**(10), 3806-3819.

Ohzeki, K., and Hosoya, Y. 2007. A study on the probability of twin plane formation during the nucleation of AgBr and AgCl crystals in the aqueous gelatin solution. *Journal of Crystal Growth*, **305**(1), 192-200.

Pastoriza-santos, I., and Liz-marza, L. M. 2002. Synthesis of Silver Nanoprisms in DMF, *Nano Letters*, **2**, 903-905.

Pinheiro, H. M., Touraud, E., and Thomas, O. 2004. Aromatic amines from azo dye reduction: status review with emphasis on direct UV spectrophotometric detection in textile industry wastewaters. *Dyes and Pigments*, **61**(2), 121-139.

Qi, X.-H., Wang, Z.-H., Zhuang, Y.-Y., Yu, Y., and Li, J.-L. 2005. Study on the photocatalysis performance and degradation kinetics of X-3B over modified titanium dioxide. *Journal of Hazardous Materials*, **118**(1-3), 219-25.

Rycenga, M., Cobley, C. M., Zeng, J., Li, W., Moran, C. H., Zhang, Q., Qin, D and Xia, Y. 2011. Controlling the synthesis and assembly of silver nanostructures for plasmonic applications. *Chemical Reviews*, **111**(6), 3669-712.

Sakthivel, S., Shankar, M. V, Palanichamy, M., Arabindoo, B., Bahnemann, D. W., and Murugesan, V. 2004. Enhancement of photocatalytic activity by metal deposition: characterisation and photonic efficiency of Pt, Au and Pd deposited on TiO$_2$ catalyst. *Water Research*, **38**(13), 3001-3008.

Samadi Khoshkhoo, M., Scudino, S., Thomas, J., Gemming, T., Wendrock, H., and Eckert, J. 2013. Size evaluation of nanostructured materials. *Materials Letters*, **108**, 343-345.

Seoudi, R., Kamal, M., Shabaka, A. A., Abdelrazek, E. M., and Eisa, W. 2010. Synthesis, characterization and spectroscopic studies of CdS/polyaniline core/shell nanocomposite. *Synthetic Metals*, **160**(5-6), 479-484.

Shukla, S., Seal, S., and Vanfleet, R. 2003. Sol-Gel Synthesis and Phase Evolution Behavior of Sterically Stabilized, *Jouranl of Sol-Gel Science and Technology*, **27**, 119-136.

Suwanboon, S., Amornpitoksuk, P., and Sukolrat, A. 2011. Dependence of optical properties on doping metal, crystallite size and defect concentration of M-doped ZnO nanopowders (M=Al, Mg, Ti). *Ceramics International*, **37**(4), 1359-1365.

Tang, Y., Jiang, Z., Xing, G., Li, A., Kanhere, P. D., Zhang, Y., Sum, T. C., Li, S., Chen, X., Dong, Z., and Chen, Z. 2013. Efficient Ag@AgCl Cubic Cage Photocatalysts Profit from Ultrafast Plasmon-Induced Electron Transfer Processes. *Advanced Functional Materials*, **23**, 2932-2940.

Tran, T. T., and Lu, X. 2011. Synergistic Effect of Ag and Pd Ions on Shape-Selective Growth of Polyhedral Au Nanocrystals with High-Index Facets. *The Journal of Physical Chemistry C*, **115**(9), 3638-3645.

Tseng, T. K., Lin, Y. S., Chen, Y. J., and Chu, H. 2010. A review of photocatalysts prepared by sol-gel method for VOCs removal. *International Journal of Molecular Sciences*, **11**(6), 2336-2361.

Turton, R. 2000. The Physics of Solids. Oxford University Press: New York.

Wang, C., Zhang, X., Shao, C., Zhang, Y., Yang, J., Sun, P., Liu, X., Liu, H., Liu, Y., Xie, T., and Wang, D. 2011. Rutile TiO$_2$ nanowires on anatase TiO$_2$ nanofibers: a branched heterostructured photocatalysts via interface-assisted fabrication approach. *Journal of Colloid and Interface Science*, **363**(1), 157-164.

Wang, H., Gao, J., Guo, T., Wang, R., Guo, L., Liu, Y., and Li, J. 2012. Facile synthesis of AgBr nanoplates with exposed {111} facets and enhanced photocatalytic properties. *Chemical Communications,* **48**(2), 275-7.

Wang, J., Zhao, H., Liu, X., Li, X., Xu, P., and Han, X. 2009. Formation of Ag nanoparticles on water-soluble anatase TiO$_2$ clusters and the activation of photocatalysis. *Catalysis Communications*, **10**(7), 1052-1056.

Wang, P., Huang, B., Lou, Z., Zhang, X., Qin, X., Dai, Y., Zheng, Z., and Wang, X. 2010. Synthesis of highly efficient Ag@AgCl plasmonic photocatalysts with various structures. *Chemical European Journal*, **16**(2), 538-44.

Wang, P., Huang, B., Qin, X., Zhang, X., Dai, Y., Wei, J., and Whangbo, M.-H. 2008. Ag@AgCl: a highly efficient and stable photocatalyst active under visible light. *Angewandte Chemie International Edition*, **47**(41), 7931-7933.

Wang, P., Ming, T., Wang, G., Wang, X., Yu, H., and Yu, J. 2014. Cocatalyst modification and nanonization of Ag/AgCl photocatalyst with enhanced

photocatalytic performance. *Journal of Molecular Catalysis A: Chemical*, **381**, 114-119.

Wang, W., Lu, W., and Jiang, L. 2009. AgCl and Ag/AgCl hollow spheres based on self-assemblies of a multi-amine head surfactant. *Journal of Colloid and Interface Science*, **338**(1), 270-275.

Wang, X., Li, S., Yu, H., and Yu, J. 2011. In situ anion-exchange synthesis and photocatalytic activity of $Ag_8W_4O_{16}$/AgCl-nanoparticle core–shell nanorods. *Journal of Molecular Catalysis A: Chemical*, **334**(1-2), 52-59.

Wang, Z. L. (2000). Transmission Electron Microscopy of Shape-Controlled Nanocrystals and Their Assemblies. *The Journal of Physical Chemistry B*, **104**(6), 1153-1175.

Weller, M. T. 1994. Inorganic Materials Chemistry. Oxford University Press: New York.

Westcott, S. L., Oldenburg, S. J., Lee, T. R., and Halas, N. J. 1999. Construction of simple gold nanoparticle aggregates with controlled plasmon-plasmon interactions, *Chemical Physics Letters*, **300**, 651-655.

West, A. R. 1984. Solid State Chemistry and its Applications. John Wiley & Sons: Chichester.

Willets, K. A, and Van Duyne, R. P. 2007. Localized surface plasmon resonance spectroscopy and sensing. *Annual Review of Physical Chemistry*, **58**, 267-297.

Xia, Y., Xiong, Y., Lim, B., and Skrabalak, S. E. 2009. Shape-controlled synthesis of metal nanocrystals: simple chemistry meets complex physics? *Angewandte Chemie International Edition*, **48**(1), 60-103.

Xu, H., Li, H., Xia, J., Yin, S., Luo, Z., Liu, L., and Xu, L. 2011. One-pot synthesis of visible-light-driven plasmonic photocatalyst Ag/AgCl in ionic liquid. *ACS Applied Materials & Interfaces*, **3**(1), 22-29.

Zeng, H. C. 2006. Synthetic architecture of interior space for inorganic nanostructures. *Journal of Materials Chemistry*, **16**(7), 649.

Zhang, F., Zheng, Y., Cao, Y., Chen, C., Zhan, Y., Lin, X., Zheng, Q., Wei, K., and Zhu, J. 2009. Ordered mesoporous Ag–TiO$_2$–KIT-6 heterostructure: synthesis, characterization and photocatalysis. *Journal of Materials Chemistry*, **19**(18), 2771.

Zhang, K., Wang, W., Yu, L., Liang, Y., Zhang, G., and Xiao, J. 2011. Tailoring optical properties of TiO$_2$ nanowires coated with Ag nanoparticles by plasmon coupling of Ag nanoparticles. *Solid State Communications*, **151**(24), 2008-2011.

Zhang, X., Chen, Y. L., Liu, R.-S., and Tsai, D. P. 2013. Plasmonic photocatalysis. *Reports on Progress in Physics*, **76**(4), 046401.

Zhao, X., and Yu, J. 2007. Morphology control of copper oxalate polycrystalline particles involving an etching process. *Journal of Crystal Growth*, **306**, 366-372.

Zhou, W., Liu, X., Cui, J., Liu, D., Li, J., Jiang, H., Wang, J., and Liu, H. 2011. Control synthesis of rutile TiO$_2$ microspheres, nanoflowers, nanotrees and nanobelts via acid-hydrothermal method and their optical properties. *Crystal Engineering Communications*, **13**(14), 4557.

Zhu, M., Chen, P., and Liu, M. 2011. Sunlight-driven plasmonic photocatalysts based on Ag/AgCl nanostructures synthesized via an oil-in-water medium: enhanced catalytic performance by morphology selection. *Journal of Materials Chemistry*, **21**(41), 16413.

Zhu, M., Chen, P., Ma, W., Lei, B., and Liu, M. 2012. Template-free synthesis of cube-like Ag/AgCl nanostructures via a direct-precipitation protocol: highly efficient sunlight-driven plasmonic photocatalysts. *ACS Applied Materials & Interfaces*, **4**(11), 6386-6392

Appendix A

To control the rate adjustment at the rate of 0.3 mL/min, the burett was equipped with an infusion set containing 20 mM $AgNO_3$ solution as shown in Figure A1.
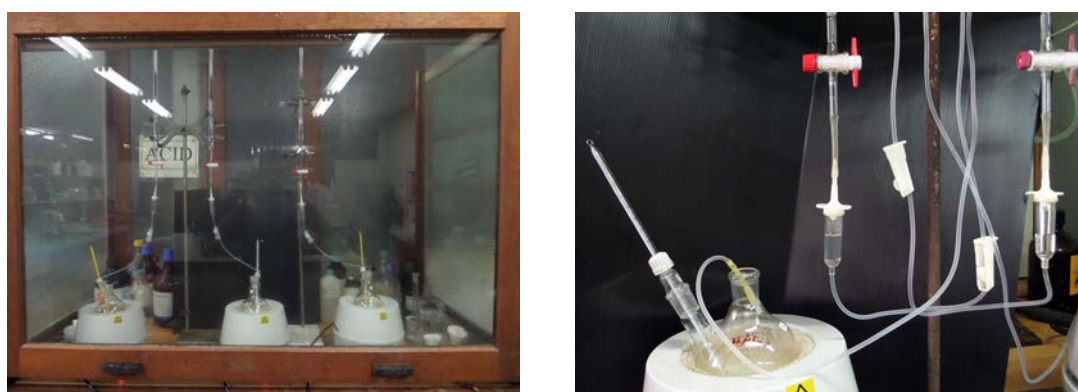
Figure A1 The experimental set–up for the synthesis method of flower–like Ag/AgCl powder.

Appendix B

The calibration graph of OG dye solution was constructed from five standard solutions: 1.0×10^{-5} M, 2.0×10^{-5} M, 3.0×10^{-5} M, 4.0×10^{-5} and 5.0×10^{-5} M. The obtained straight line with $R^2 = 0.9995$ is shown in Figure B1
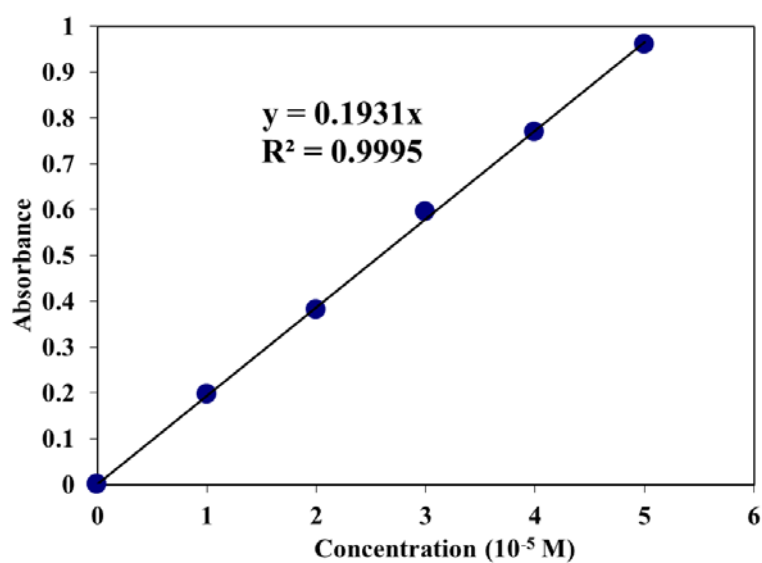
Figure B1 The standard calibration curve of OG dye solution in the range of 1.0×10^{-5} M to 5.0×10^{-5} M.

Appendix C

The plots of $\ln(C_0/C)$ versus time yielded straight lines for urchin–like Ag/AgCl and its comparative materials, indicating that the degradation of OG by these samples under UV and visible light are of pseudo–first order process as shown in Figure C1 (a) and (b), respectively.
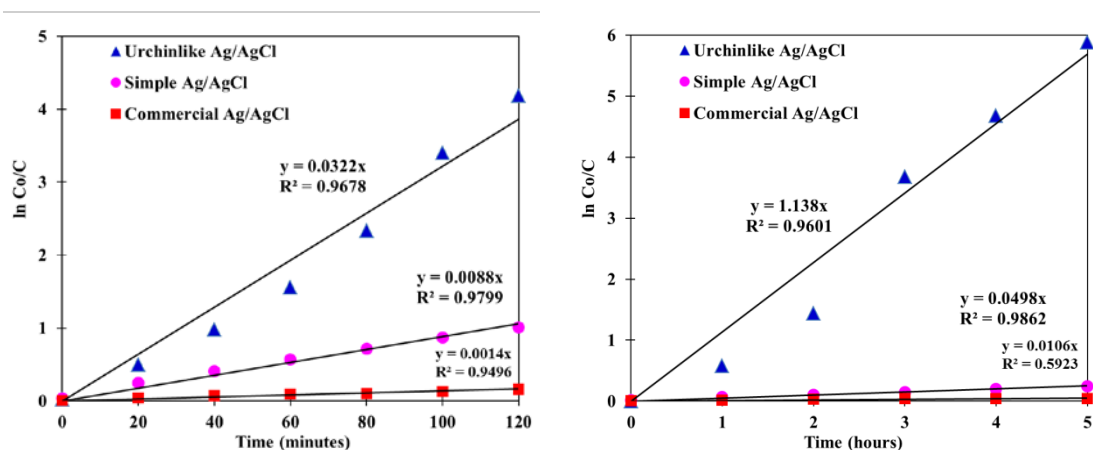
Figure C1 The kinetics plot of orange G using urchin–like Ag/AgCl under UV light (a) and visible light irradiation (b).

Appendix D

Table D1 The elemental analysis from SEM-EDX of flower–like Ag/AgCl sample

Elements	Weight %
C	59.70
Au	11.80
Ag	21.80
Cl	6.70

In 100 g of the sample, the amount of Ag and Cl are 21.80 and 6.70 g, respectively.

These amounts can be converted to number of moles as,

$$n_{Ag} = \frac{weight}{MW} = \frac{21.80 \text{ g}}{107.87 \text{ g/mol}} = 0.2021 \text{ mol}$$

$$n_{Cl} = \frac{weight}{MW} = \frac{6.70 \text{ g}}{35.45 \text{ g/mol}} = 0.1890 \text{ mol}$$

Then, the mole ratio for Ag: Cl is 0.2021: 0.1890 or 1.06: 1

Table D2 Elemental analysis from XPS spectra of flower–like Ag/AgCl sample

Elements	Weight %
O 1s	9.54
Ag 3d	55.83
C 1s	18.63
Cl 2p	16.00

In 100 g of the sample under measurement, the number of moles of Ag and Cl can be calculated as,

$$n_{Ag} = \frac{weight}{MW} = \frac{55.83 \text{ g}}{107.87 \text{ g/mol}} = 0.5176 \text{ mol}$$

$$n_{Cl} = \frac{weight}{MW} = \frac{16.00 \text{ g}}{35.45 \text{ g/mol}} = 0.4513 \text{ mol}$$

Hence, the mole ratio of Ag to Cl is $n_{Ag} : n_{Cl} = 0.5176 : 0.4513$ or $1.15 : 1$.

Therefore, the mole ratio between Ag and Cl is 1.15: 1

Table D3 Analysis of Ag^+ ion and metallic Ag from deconvoluted peak of XPS spectra

Elements	Binding energy (eV)	Oxidation state of Ag element	Weight %
Ag 3d$_{5/2}$	367.8	+1	52.3
Ag 3d$_{5/2}$	368.5	0	6.8
Ag 3d$_{3/2}$	373.8	+1	35.7
Ag 3d$_{3/2}$	374.5	0	5.3

In 100 g of total Ag under measurement, the number of moles of Ag^+ and Ag^0 can be calculate as,

$$n_{Ag^+} = \frac{weight}{MW} = \frac{52.3 + 35.7 \text{ g}}{107.87 \text{ g/mol}} = 0.8158 \text{ mol}$$

$$n_{Ag^0} = \frac{weight}{MW} = \frac{6.8 + 5.3 \text{ g}}{107.87 \text{ g/mol}} = 0.1122 \text{ mol}$$

Hence, the mole ratio of Ag^+ to Ag^0 is $Ag^+: Ag^0 = 0.8158: 0.1122 = 7.27: 1$.

Therefore, the mole ratio of Ag^+ and Ag^0 is 7.27: 1

Paper I

Urchinlike Ag/AgCl photocatalyst: Synthesis, characterization, and activity

Hasan Daupor and Sumpun Wongnawa*

*Corresponding author. Tel.: +66 74 288443. E-mail address: sumpun.w@psu.ac.th (S. Wongnawa).

Urchinlike Ag/AgCl photocatalyst: Synthesis, characterization, and activity

CrossMark

Hasan Daupor, Sumpun Wongnawa *

Department of Chemistry and Center of Excellence for Innovation in Chemistry, Faculty of Science, Prince of Songkla University, Hat Yai 90112, Songkhla, Thailand

ABSTRACT

In this paper, an extraordinary Ag/AgCl compound with surprisingly photocatalytic activity was synthesized. The synthesis route was straight forward involving hydrolysis followed by ion-exchange reactions without using strong reducing and dispersing agents. The starting materials were $TiCl_4$ and $AgNO_3$. The latter was dissolved in ammonia solution prior to the addition of $TiCl_4$. The morphology, composition, and phase structure of the as-prepared product were characterized by X-ray diffraction spectroscopy (XRD), X-ray photoelectron spectroscopy (XPS), transmission electron microscopy (TEM), scanning electron microscopy (SEM), UV–visible diffused reflectance spectroscopy (DRS), and surface area analysis. The striking feature of this product was its near spherical shape aggregation of AgCl particles whose surface was fully covered with nanohairs. The lengths of the nanohairs were about 30 to 50 nm. The product was found to contain traces of metallic Ag mixed with the parent compound AgCl. The optical absorption spectrum of this product exhibited a strong absorption in the visible region because of the surface plasmon resonance (SPR) effect of Ag metal nanoparticles. Under either UV or visible light irradiation, urchinlike Ag/AgCl showed higher photocatalytic activity than commercial AgCl, simple AgCl, and commercial Degussa P25 TiO_2. The possible photocatalytic mechanism is discussed based on the probable role of metallic Ag nanoparticles in enhancing the photocatalytic performance. The photocatalytic pathway was originated from the enhanced absorption for UV–visible light, electron–hole separation, and formation of Cl atoms in Ag/AgCl nanostructure.

© 2014 Elsevier B.V. All rights reserved.

1. Introduction

Environmental pollution especially those related with contaminated water and polluted air have been increasingly prominent and exerting their effects on the global warming and human health seriously. Many researches have been undertaken to avert this harmful-to-human issue. The promising applications of metal oxides such as TiO_2 and ZnO have been recognized as an active photocatalyst for environmental clean-up since they can decompose a large number of organic and inorganic pollutions [1–3]. However, due to the wide band gap of both TiO_2 and ZnO [4,5], the two popular photocatalysts work well with UV radiation. If day light is the main source of power, the two metal oxides are of little use since day light composes of only small fraction of UV light (*ca.* 3–5%). Another well known intrinsic problem of these two metal oxides is the rapid recombination of the electron and holes produced upon photon absorption and seriously affect their photocatalytic activities. Therefore, the ability to either change the band gap to allow

* Corresponding author. Tel.: +66 74 288443; fax: +66 74 212918.
E-mail address: sumpun.w@psu.ac.th (S. Wongnawa).

photoactivity on irradiation with visible light or to decrease the electron–hole recombination rate is being searched. Many efforts have been attempted by deposition of TiO_2 and ZnO with noble metals such as Au, Pt, Ru, Pd, and Ag, so as to efficiently extend photoresponse from UV to visible light [6,7]. The deposition of noble metals on the surface is not only act as a trap to capture the photoinduced electron and hole leading to the reduction of electron–hole recombination in photocatalytic process but also act to increase the absorption ability for visible range due to the surface plasmon resonance (SPR) effect of noble metal [8,9]. Some noble metals such as Pt, Pd, Rh, and Au may be too expensive to be useful in wide scale applications. Thus, the research on Ag modified photocatalyst shows more significant practical value.

Metal nanomaterials, especially, Ag and Au nanoparticles [10] have been extensively studied over the past decades due to their unique SPR properties in the visible region which are useful for catalysts, surface plasmonics, surface-enhanced Raman scattering, nonlinear optics, chemical and biological sensing, and cancer therapies [11,12]. The SPR can dramatically amplify the absorption of visible light which opens up new opportunities for the deployment of photocatalysts for environmental clean-up. The SPR effect of Ag metal was believed to be the main role in improving the

78

photocatalytic activity of silver halide by acting as the sites for the H_2 formation in the CH_3OH/H_2O solution in photocatalytic reaction under UV illumination (AgX, X = I, Br, Cl) [13,14].

Silver halides are photosensitive materials extensively used in photographic films and optical devices. On absorbing a photon, a silver halide particle generates an electron and a hole, and subsequently the photogenerated electron combines with an Ag ion to form an Ag metal atom. Ultimately, a cluster of silver atoms is formed within a silver halide particle upon repeated absorption of photons. Due to this instability under sunlight, which provides the very basis for chemical photography, silver halides are seldom used as photocatalysts. Nevertheless, there have been reports that under UV–visible illumination AgCl deposited on a conducting support photocatalyzed the oxidation of water to O_2 in the presence of a small excess of silver ions in solution [15,16]. Recently, the application in photocatalysis with plasmonic photocatalysts (Ag/AgCl) having stronger absorption and activity under visible light has attracted scientists' attention all over the world and becomes a hot spot in the field of photocatalysis [17]. Most of the researches about Ag/AgCl photocatalyst used the photon energy or reducing agent to reduce some part of Ag ions in AgCl to metallic Ag particles. In a research of Wang et al. [18] and Wang et al. [19], they synthesized AgCl by ion exchange reactions (between Ag_2MoO_4 and HCl). After AgCl precipitated completely, Ag ions were reduced by irradiating with a 300 W Xe arc lamp. The resulting precipitate consisted of Ag nanoparticles deposited on AgCl particles in the form of Ag/AgCl catalyst. Reports involving synthesis of Ag/AgCl and using UV illumination to reduce Ag ions have appeared recently [20,21]. On the other hand, the studies that used reducing agents such as ethylene glycol [22], sodium borohydride [23], ascorbic acid [24], to reduce Ag^+ ion to metallic Ag particles also appeared. In the latter these reducing agents were added during the synthesis process, partial AgCl could be converted to Ag metals through the reduction by these reducing agents.

Many physical properties of nanostructure are strongly dependent on morphologies, therefore, various kinds of nanostructures were developed to improve their physical properties such as, hollow sphere, chestnut-like, nanorod, nanoflower, nanotree, nanobelt, and nanobranch [25–28]. Nanostructures represent the useful applications in many fields due to their large specific surface area and interesting optical properties. Spherical Ag/AgCl nanoparticles were prepared using polyvinyl alcohol as dispersing agent followed by light irradiation. The as-synthesized plasmonic photocatalysts has been reported to exhibit the enhanced photocatalytic performance with methylene blue over pure AgCl [29]. Likewise, cubic Ag/AgCl nanoparticles, prepared by hydrothermal method using CH_2Cl_2 as chloride source, has been reported to have high acitivity in degradation of methyl orange under visible light [30]. Lou et al. [17] synthesized near-spherical AgCl microcrystals by hydrothermal method from which the plasmonic photocatalyst Ag/AgCl was obtained through the reduction with visible light irradiation. The near-spherical Ag/AgCl was collected and showed much higher photocatalytic activity with methyl orange dye than cubic Ag/AgCl. Zhu et al. [31], studied the cube-like Ag/AgCl nanostructures obtained *via* the direct-precipitation method as a photocatalyst and found that nearly 100% of methyl orange dye and 80% of 4-chlorophenol were decomposed under similar conditions. Meanwhile, when the spherical Ag/AgCl nanostructures, synthesized *via* a surfactant-assisted method, were used as a photocatalyst only 62.3% and 55% of methyl orange dye and 4-chlorophenol were photodecomposed, respectively. For comparison, the commercially available P25-TiO$_2$ could only slightly decompose these organic pollutants indicating the less photocatalytic efficiency of P25-TiO$_2$ than these plasmonic Ag/AgCl photocatalysts [31]. AgCl, AgBr, and AgI were used to improve the photocatalytic activity under visible light irradiation of TiO_2 by introducing silver halides

onto the surface of titanate nanowired honeycomb (TNHC) films. It was found that Ag/AgCl/TNHC exhibited higher photocatalytic activity than Ag/AgBr/TNHC and Ag/AgI/TNHC and showed strong visible light absorption around 400–700 nm [32]. In another work, to overcome the limited adsorption of dye on composite materials due to low surface area and weak electrostatic interactions with dye molecules, Tang et al. successfully incorporated silver halides onto the surface of titanate nanotube (P-TNT) to obtain high surface area. The nanohybrid plasmonic photocatalysts: Ag–AgCl-TNT, Ag–AgBr–TNT, and Ag–AgI–TNT showed the synergistic effect of adsorption and photodegradation leading to excellent performance in dye degradation [33].

In the present work, we report alternative method to synthesize Ag/AgCl using different reagents from those mentioned above. This method employed TiCl$_4$ which first acted as a chloride ion source and, second, it might have some effect on the growth of nano-hairs *via* forced hydrolysis of TiCl$_4$ precursors as found in the work by Wang et al. [34]. The Ag^+ ions are prone to easy reduction to Ag^0 under reaction condition, for example, Ag ions in AgCl were reduced during the hydrothermal process at temperature >60°C [35]. In this work, the obtained Ag/AgCl clusters possessed near spherical kernel covered with countless tiny hairs pointing outwardly. The physical appearance of this product resembles many metal oxides having sea urchin shape [36] making it comfortably fits into the "urchinlike" group of nanostructure shapes hence, hereinafter, it will be referred to as the *urchinlike Ag/AgCl*. The peculiar hairy surface should be very useful to help adsorb the dye molecules leading to the excellence photocatalytic activity to be discussed in the following sections.

2. Experimental

2.1. Materials

Titanium tetrachloride (TiCl$_4$, Merck), silver nitrate (AgNO$_3$, Merck), and ammonium hydroxide (NH$_4$OH, Baker) were of analytical grade. Other key chemicals were: commercial AgCl (Sigma–Aldrich), titanium dioxide P25 (Degussa AG, Frankfurt, Germany), and commercially available orange G dye (Fluka, $C_{16}H_{10}N_2Na_2O_7S_2$, 452.38 g/mol). All of chemical were used directly without further purification and deionized water was used in all experiments.

2.2. Synthesis of urchinlike Ag/AgCl nanostructure

The urchinlike Ag/AgCl nanostructure was synthesized by the two steps reaction as shown in Path A in Fig. 1: the first step involved the production of Ag ions and the second one was the reaction with neat TiCl$_4$. The solution of Ag ions was obtained by dissolving 1 g of AgNO$_3$ in 80 mL of diluted NH$_4$OH solution (conc. NH$_4$OH:H$_2$O = 1:1) and was refluxed at 100°C for 2 h under vigorously stirring. The resulting solution which had pH ≅ 10 was then slowly added to ice-water cooled neat TiCl$_4$ with vigorously stirring. The solution now turned to very acidic (pH < 1) with the occurrence of white powder of AgCl which was collected and washed with deionized water. The precipitate appeared as white powder in solution but it turned to purple–gray powder after filtering and rinsing. The powder was dried at 40°C for about 6 h to obtain the light purple–gray of urchinlike Ag/AgCl powder.

To compare other synthesis parameters two variations with the same procedure as above were carried out: (i) with un-refluxed AgNO$_3$ solution and (ii) only the NH$_4$OH solution was refluxed and used without AgNO$_3$ as shown in Fig. 1 (Path B and Path C, respectively).
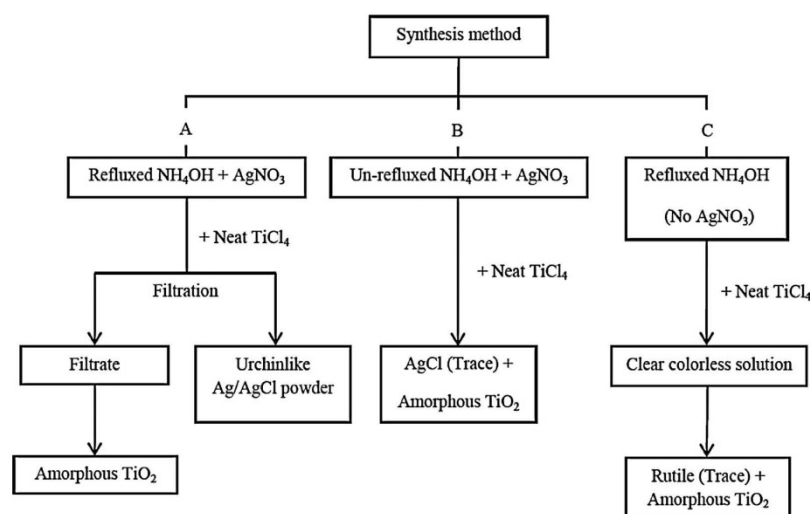
Fig. 1. Flow chart of the synthesis of urchinlike Ag/AgCl powder.

For the purpose of comprehensive comparison, conventional AgCl was prepared as precipitation from AgNO₃ solution with 1 M HCl solution. This precipitate was designated as 'simple AgCl' and was further used to produced 'simple Ag/AgCl' by photoreduction (using blacklight tube 20 W, 3 min) with continuously stirring. The resulting sample was collected and washed with deionized water, and dried at 40 °C. With similar procedure 'commercial Ag/AgCl' was also prepared from commercial AgCl powder. Both light purple powders were used in experiments in comparison with the titled urchinlike Ag/AgCl product.

2.3. Characterization of samples

Morphology and particle shape of the samples were studied by a JEM-2010 transmission electron microscope (TEM) and a JSM-5800 LV scanning electron microscope (SEM), JEOL Apparatus, Japan. The corresponding energy dispersive X-ray spectroscopy (EDS) was analyzed with Electron Microanalysis equipped on the SEM microscope. The specific surface area was measured by Quanta-chrome, Autosorb-1, Thermo Finnigan, Sorptomatic 1990, USA, employing the Brunauer–Emmett–Teller (BET) equation. The X-ray diffraction (XRD) analysis of AgCl powders was carried out on a Philips PW 3710 powder diffractometer (PHILIPS X'Pert MPD, The Netherlands), using Cu $K\alpha$ (Ni filtered) radiation $\lambda = 1.5406$ Å. The patterns were recorded in a range of 10–80° at room temperature. The chemical composition of sample surface was investigated by X-ray photoelectron spectrometer (XPS), AXIS ULTRADLD, Kratos Analytical, Manchester, UK. The spectra were calibrated to the binding energy of C 1s peak at 285.0 eV. The band gap energy of the samples were determined using UV–visible diffused reflectance spectroscopy (DRS) with a UV-2401 spectrophotometer (Shimadzu, Japan) equipped with an integrating sphere in the range of 200–800 nm using BaSO₄ as a reference. The band gap energy (E_g) of samples were calculated according to the equation:

$$E_g = h\frac{C}{\lambda} = \frac{1240}{\lambda}$$

where E_g is the band gap energy (eV), h is the Planck's constant, C is the light velocity (m s⁻¹), and λ is the absorption onset wavelength (nm).

2.4. Photocatalytic procedure

In the experimental set up for the photocatalytic studies, a portion of 100 mL of 5.0×10^{-5} mol dm⁻³ of orange G solution was placed in a beaker followed by addition of 0.5 g L⁻¹ of each catalyst (synthesized urchinlike Ag/AgCl, simple AgCl, commercial AgCl, simple Ag/AgCl, commercial Ag/AgCl, commercial Degussa P25). After adding the catalyst, the solution was stirred in the dark for 30 min to ensure the adsorption/desorption dye/catalyst equilibrium. The zero time readings were then taken and the solution was irradiated. An aliquot (4 mL) was taken at time intervals and centrifuged (4500 rpm for 5 min) to separate the catalyst from the solution prior to the absorbance measurements. The degradation percentage of orange G was followed by measuring absorbance at 480 nm using a UV–visible spectrophotometer (Specord S100, Analytik Jena GmbH, Germany). The degradation yield is defined as

$$\text{Degradation yield} = \frac{C_0 - C_t}{C_0} \times 100$$

where C_0 is the dye concentration at the beginning of illumination and C_t is the concentration after photodegradation.

The controlled experiments, without catalyst or light, were performed to confirm that the degradation of dye depended on the presence of both light and Ag/AgCl catalyst powder.

In the recyclability experiment, the used urchinlike Ag/AgCl catalyst was separated from the preceding reaction solution and was used with the new portion of fresh dye solution. The experimental setup was the same as that given above.

3. Results and discussion

3.1. Product formation

In the synthesis of urchinlike Ag/AgCl nanostructure (Path A, Fig. 1) when less than 5 mL of refluxed ammonia solution of AgNO₃ was slowly added to neat TiCl₄ liquid, a large amount of white solid formed with some small yellow area at the surface. [If let standing in air this solid would turn to white solid which, from the XRD pattern, was TiO₂. The peaks in this XRD pattern (Fig. 2a) were those
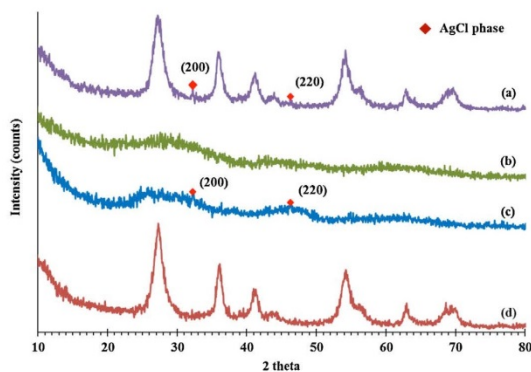
Fig. 2. XRD patterns of: (a) amorphous TiO_2 with some of rutile and AgCl phases, (b) amorphous TiO_2 from the clear colorless filtrate, (c) amorphous TiO_2 with trace amount of AgCl, and (d) amorphous TiO_2 with trace amount of rutile.

Fig. 3. XRD patterns of: (a) commercial AgCl, (b) urchinlike Ag/AgCl, and (c) simple AgCl.

of rutile and were rather broad indicating the amorphous nature with some small amount of rutile mixed in. In addition, the very small characteristic peaks of AgCl phase at 32.24° and 46.25° were also observed in this XRD spectrum.] If larger amount (ca. 7 mL) of ammonia solution of $AgNO_3$ was added, the light yellow colloid was obtained. If more than 7 mL (e.g. 10 mL) was added the colloid formed but rapidly dissolved and white powder of AgCl began to precipitate in the clear light yellow solution. When the addition reached 80 mL the clear light yellow solution completely disappeared and the clear colorless solution with white powder of AgCl was obtained. The color change of this AgCl product from white to purple–gray during the filtration and rinsing could be because of the presence of metallic Ag nanoparticles. The latter occurred possibly by the reduction ability of $TiCl_4$ [34]. [The clear colorless filtrate was left standing at room temperature for about 1 week and precipitated to give amorphous TiO_2 (Fig. 2b).]

While in the comparative synthesis (i) (Path B in Fig. 1) yielded different result as the amorphous TiO_2 was obtained as the major product with a trace amount of AgCl (Fig. 2c). In the comparative synthesis (ii) (Path C in Fig. 1), the first contact with neat $TiCl_4$ produced white precipitate which disappeared after adding more $TiCl_4$ to yield a clear colorless solution. On a long standing (about one week) this clear solution yielded amorphous TiO_2 as the major product but with trace amount of TiO_2 (rutile) (Fig. 2d).

3.2. Characterization of products

3.2.1. X-ray diffraction patterns

The XRD patterns of urchinlike Ag/AgCl, simple AgCl, and commercial AgCl are shown in Fig. 3. The pattern of 2θ peaks are: 27.82°, 32.24°, 46.25°, 54.82°, 57.45°, 67.42°, 74.44°, 76.72° and 85.67° corresponding to the crystal planes of face center cubic crystal of AgCl (1 1 1), (2 0 0), (2 2 0), (3 1 1), (2 2 2), (4 0 0), (3 3 1), (4 2 0) [19,37]. No characteristic peaks of other phases such as metallic Ag were observed. The characteristic strong diffraction peak at 32.2° (2θ) which is commonly assigned to the basal $d_{(2 0 0)}$ reflection of AgCl remained virtually unchanged [29,38]. Relevant parameters obtained from XRD data are given in Table 1. The presence of metallic Ag was not detected in the XRD spectra probably because of the amount of metallic Ag was too low to be detectable, however, it showed up in the TEM images as black area in the middle of urchinlike Ag/AgCl as well as by the XPS measurement.

On a closer inspection of the XRD patterns in Fig. 3, one can see that the (2 0 0) diffraction peak of urchinlike Ag/AgCl has higher
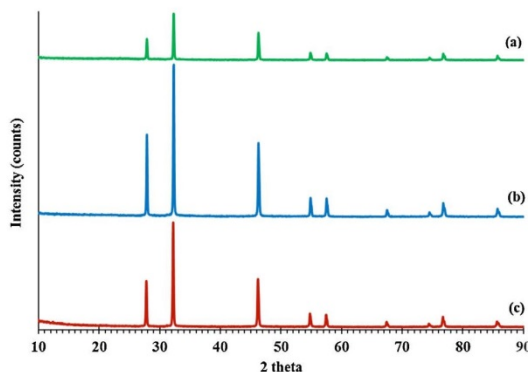
intensity than the commercial AgCl. This could arise from high crystallinity of AgCl abundantly assembled into nano-hair crystallines covering on the particle surface as shown in TEM images (vide infra). The crystallite size, shown in Table 1, was determined from the diffraction peak broadening using the Scherrer's equation:

$$D = \frac{K\lambda}{\beta \cos \theta}$$

where D is the crystallite size of the catalyst, λ is the X-ray wavelength, β is the full width at half maximum of strongest ling, $K = 0.89$ is a coefficient, and θ is the diffraction angle [39]. The crystallite size of urchinlike Ag/AgCl samples was smaller than commercial AgCl. The crystallite size estimated from the Scherrer's equation yields the smallest possible size compared with sizes determined by other means, e.g., by surface area or an SEM [40].

3.2.2. XPS analysis

The chemical states of Ag species in urchinlike Ag/AgCl aggregates were examined by XPS measurement. The survey spectrum of the sample confirmed that Ag and Cl were the main compositions as shown in Fig. 4a. The carbon peak at 285.0 eV was used as the reference. In Fig. 4b, the Ag 3d spectrum consists of two individual peaks at approximately 367.8 and 373.8 eV, which can be attributed to Ag $3d_{5/2}$ and Ag $3d_{3/2}$ binding energies, respectively. Each peak could be further deconvoluted into two peaks yielding two doublets. The first doublet at 367.8 and 373.8 eV, occupying the larger area of peaks, could be attributed to the Ag^I of AgCl while the smaller doublet at 368.8 and 374.8 eV could be assigned to the metallic Ag^0 [31,41]. The presence of small amount of metallic Ag^0 presumably came from the gradual reduction of Ag(I) in AgCl. For Cl 2p, two peaks were observed at binding energies 198.2 and 199.7 eV, which were assigned to the characteristic doublets of Cl $2p_{3/2}$ and Cl $2p_{1/2}$ [42], respectively (Fig. 4c). Altogether these results confirm that the obtained product consisted of metallic Ag and AgCl.

Table 1
XRD data of three types of AgCl studied in this work.

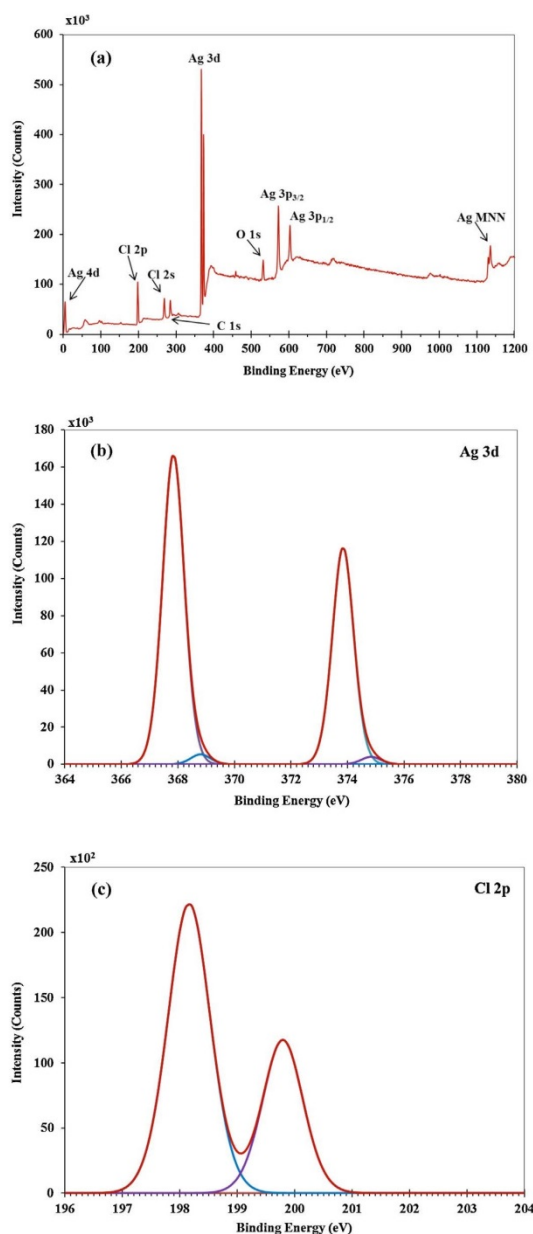| Parameters	Samples		
	Commercial AgCl	Simple AgCl	Urchinlike Ag/AgCl
2θ	32.31	32.30	32.24
d value (Å)	2.771	2.771	2.776
Crystallite size (nm)	56	56	42

Fig. 4. XPS spectra of the sample of urchinlike Ag/AgCl: (a) survey scan, (b) high resolution spectrum of Ag 3d, and (c) high resolution spectrum of Cl 2p.

3.2.3. UV–visible diffused reflectance spectroscopy (DRS)

The general physical appearance of simple AgCl is a white crystalline solid but upon illumination or heating converts it to metallic Ag and Cl_2 which is perceived by grayish or purplish coloration to some samples. In addition, it can be reduced over reducing agents such as ethylene glycol, sodium borohydride, and ascorbic
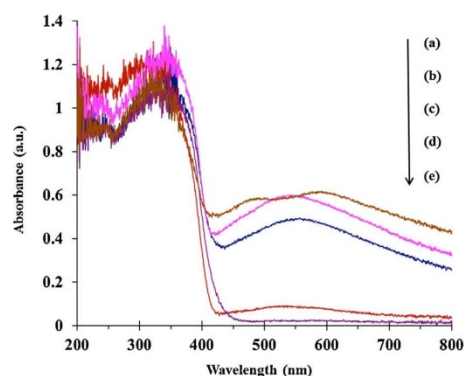

Fig. 5. DRS spectra of: (a) urchinlike Ag/AgCl, (b) simple Ag/AgCl, (c) commercial Ag/AgCl, (d) simple AgCl, and (e) commercial AgCl.

acid [22–24]. These results make some parts of AgCl to become metallic Ag co-existing with AgCl particles which displays the essential principle in the visible light absorption. Fig. 5 shows the DRS spectra of urchinlike Ag/AgCl obtained from the present synthesis method without using any specific reducing agents in comparison with simple AgCl, commercial AgCl, simple Ag/AgCl, and commercial Ag/AgCl. The absorption spectrum between 400 and 700 nm reflected the surface plasmon resonance (SPR) properties of Ag metal nanoparticles that is able to absorb light in the visible range. This absorption behavior corresponded with the observation reported by other researchers that it was originated from the characteristic absorption of surface plasmon resonance (SPR) of metallic Ag on the AgCl surface [43,44]. Therefore, the absorption spectra in the visible range can be used to confirm the existence of metallic Ag (or Ag^0) in AgCl. The sample of urchinlike Ag/AgCl possesses two broad absorption peaks about 460 and 580 nm (Fig. 5, line a) while the simple and commercial Ag/AgCl has one SPR absorption band around 550 nm (Fig. 5, line b and c). This difference could be realized since absorption properties of SPR was affected by shape, particle size, orientation, and contact area with the substrate [45–47]. As a result of this SPR absorption, all three metallic Ag containing samples exhibited light purple color. These metallic Ag nanoparticles can improve the light absorption of AgCl and increase its photocatalytic activity [48]. On the other hand, the simple and commercial AgCl which contain pure AgCl do not show the absorption band of metallic Ag (Fig. 5, line d and e). The urchinlike Ag/AgCl has absorption edge (λ_{onset}) around 440 nm corresponding to the band gap energy of 2.81 eV which is lower than that of commercial AgCl (2.95 eV) [49]. The lower band gap energy means less activation energy for electron–hole separation which enhances the photocatalytic activities of the urchinlike Ag/AgCl particles.

3.2.4. Transmission electron microscopy (TEM)

The transmission electron microscopy images of these samples are shown in Fig. 6. The titled AgCl nanoparticles synthesized from this work existed as a nano-haired particles with particle size around 70 to 120 nm as shown in Fig. 6a–d. The outer surface of the particles was densely covered with a lot of nano-hair crystals each of which had the size of approximately 2–4 nm and about 20–30 nm in length. The inner surfaces of the urchinlike Ag/AgCl particles appeared as black clusters about 10–20 nm which are physically similar to metallic Ag nanoclusters reported by Zhang et al. [50]. The hairy surface of this Ag/AgCl nanoparticles should be of great assistance for the adsorption of dye molecules on their surfaces and
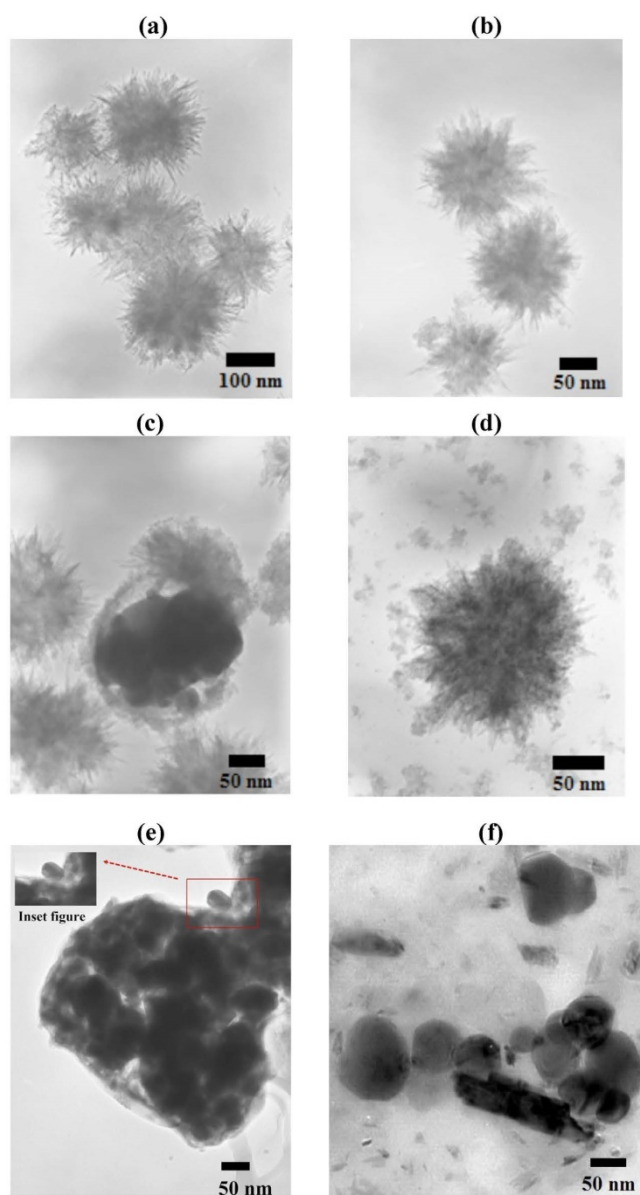
82

Fig. 6. TEM images of (a–d) urchinlike Ag/AgCl, (e) commercial AgCl, and (f) simple AgCl.

help increase the photodegradation efficiency. On the contrary, the commercial and the simple AgCl both have smooth hairless surfaces and both have particle sizes around 50–80 nm as shown in Fig. 6e–f, respectively.

3.2.5. Scanning electron microscopy–energy dispersive spectroscopy (SEM–EDS)

Fig. 7a–c show the SEM images of the overall morphology of the urchinlike Ag/AgCl particles which aggregated into a nearly spherical shape of diameter range 600–1000 nm. The sizes of these aggregates observed from SEM image were different from the sizes as seen from TEM images due to the disruption by ultrasonic during the sample preparation process for TEM technique. The nanohairs on the surface may play an important role here as "the hook and loop fastener" that helps binding small particles together to form the larger ones. The images of simple AgCl at different magnifications are shown in Fig. 7d–e. Here the particles of simple AgCl appear like poorly shaped spheres corroding from originally cubic

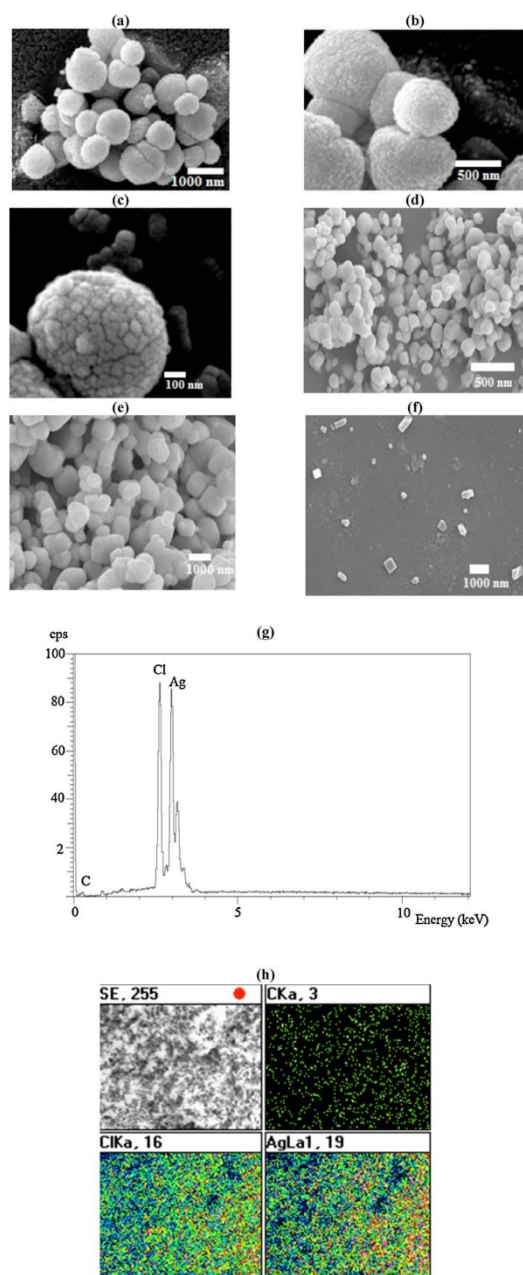Fig. 8. TGA curve (a) and DSC curve (b) of urchinlike Ag/AgCl nanoparticles.

Fig. 7. (a)–(c) SEM images of urchinlike Ag/AgCl with different magnification, (d)–(e) SEM images of simple AgCl with different magnification, (f) SEM image of commercial AgCl, (g) EDS elemental analysis, and (h) mapping analysis of urchinlike Ag/AgCl.
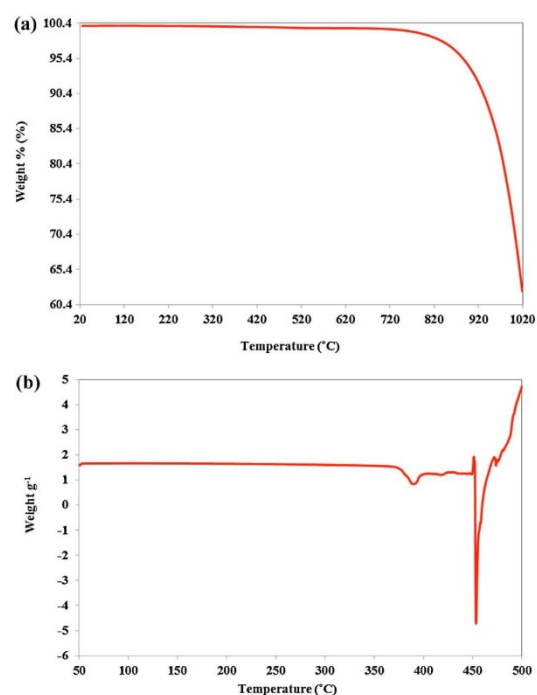
particles (while they look almost like sphere in TEM). The commercial AgCl particles appear more or less similar to the TEM image.

The EDS results (Fig. 7g–h) showed that Ag and Cl were the only two elements present in urchinlike Ag/AgCl particles. In the mapping analysis, the color points of Ag element were distributed evenly to the same degree as those of Cl supporting the co-existence as AgCl of the sample. In addition, the population of color point of Ag element is distinctly higher than the color point of Cl element which could be interpreted that the atomic ratio of Ag:Cl elements is higher than 1:1 suggesting the presence of metallic Ag coexisting with AgCl.

3.2.6. Thermal analysis (TGA-DSC)

Thermal stability of the as-prepared urchinlike Ag/AgCl particles was investigated with TGA and DSC to check for the presence/absence of volatile products in the composition of sample of which the results are shown in Fig. 8a–b, respectively. The almost non-loss of the weight of the sample from the TGA curve can be taken as an indication for the non-existence of volatile products in the composition of the urchinlike Ag/AgCl. The sharp exothermic peak at around 453.3 °C could be attributed to the decomposition of high purity AgCl during the thermal process [17].

3.3. Photocatalytic degradation of orange G dye

The photocatalytic activity of urchinlike Ag/AgCl powder was investigated with orange G dye which is anionic dye. The maximum absorption at 480 nm was used to follow the degradation caused by the Ag/AgCl catalyst (9a and 10a). For comparison, the photodegradation by five other catalysts: commercial AgCl, commercial Ag/AgCl, commercial Degussa P25, simple AgCl, and simple
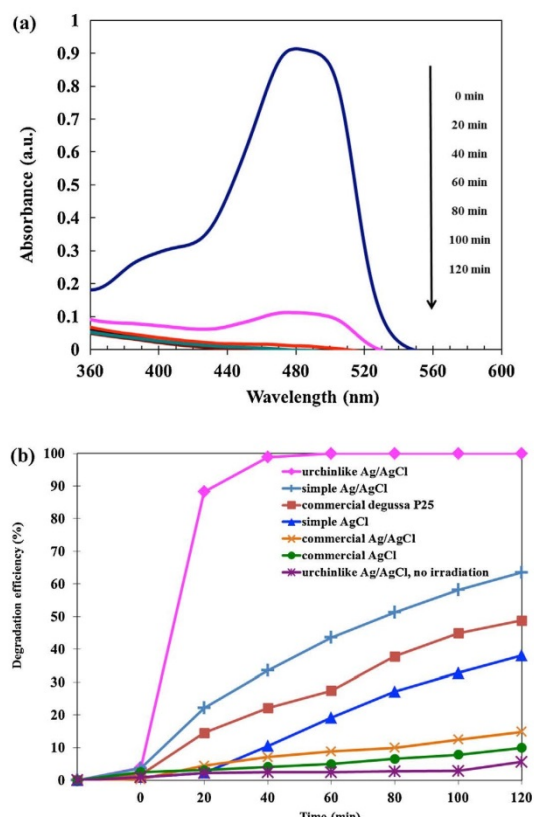
Fig. 9. (a) The changes in absorption of orange G dye under studied with UV irradiation and (b) photodegradation efficiency of orange G dye with different AgCl catalysts.

Fig. 10. (a) The changes in absorption of orange G dye under studied with visible light irradiation and (b) photodegradation efficiency of orange G dye with different AgCl catalysts.

Ag/AgCl were also carried out under the same conditions with both UV and visible light irradiations.

3.3.1. With UV light

Under UV light irradiation the urchinlike Ag/AgCl showed the highest photocatalytic activity toward orange G dye over other catalysts under studied in this work. Orange G dye molecules could be completely destroyed by the urchinlike Ag/AgCl within 40 min while only 10% was destroyed by the simple AgCl under the same period of time as shown in Fig. 9b. The photodegradation took place rather quick in the first 20 min.

3.3.2. With visible light

Under visible light irradiation the urchinlike Ag/AgCl catalyst was also the top performer among all catalysts in this study. The orange G dye was almost completely degraded by the urchinlike Ag/AgCl catalyst (> 97%) in 3 h under visible light as shown in Fig. 10b. On the contrary, the simple AgCl degraded the dye only about 20% with longer illumination time (5 h).

From these results, we can see that the as-synthesized urchinlike Ag/AgCl catalyst exhibited higher photocatalytic activity than that of commercial AgCl and simple AgCl in discoloration of orange G dye under UV and visible light irradiations. In addition, the comparison was also extended to that of Degussa P25 even though
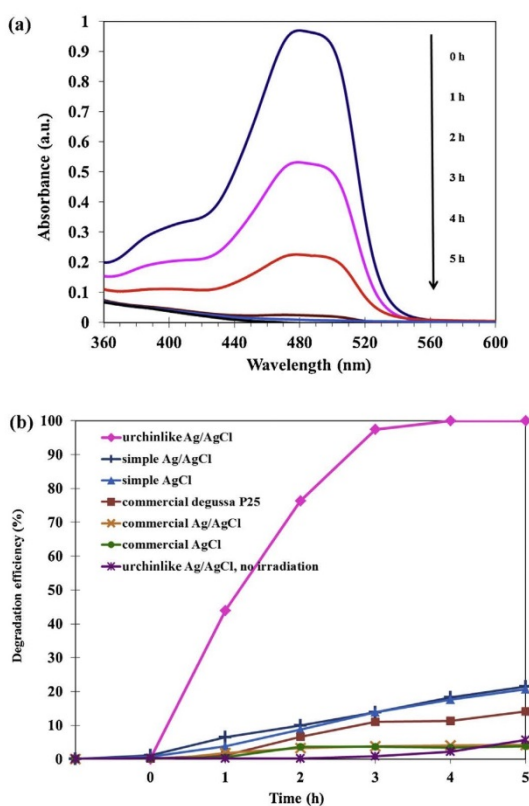
it does not contain silver but it is the best known photocatalyst to date. The urchinlike Ag/AgCl catalyst still showed much higher activity in degradation of orange G dye than Degussa P25. The better performance of urchinlike Ag/AgCl catalyst may be attributed to its two most prominent features: the hairy surface and the presence of metallic Ag nanoparticles. The former led to enhancing the dye adsorption on the catalyst surface and hence increased the photocatalytic efficiency. The BET specific surface areas of the urchinlike Ag/AgCl and the commercial AgCl are 1.58 and 1.14 $m^2\,g^{-1}$, respectively, and are not considered as the decisive factor in this case since they both are similar and low. The effect from surface morphology, however, can be very significant for the particles of irregular shapes. Similar result was found in the case of nanobranched TiO$_2$ array on TiO$_2$ nanorods which enhanced dye adsorption on the TiO$_2$ nanobranched [51]. While the latter, the presence of metallic Ag nanoparticles, helped improve the light absorption efficiency by the SPR effect of the metallic Ag particles situated on its surface [52]. As a result, the urchinlike Ag/AgCl acted as the best photocatalyst in our studies.

From the photocatalytic results we can see that simple AgCl showed lower activity than urchinlike Ag/AgCl in discoloring orange G dye under UV and visible light irradiation. However, when it was doped with Ag metal nanoparticles, e.g. depositing on the material surfaces, it turned to be an excellent catalyst which could effectively degrade organic dyes [53]. In an attempt to understand
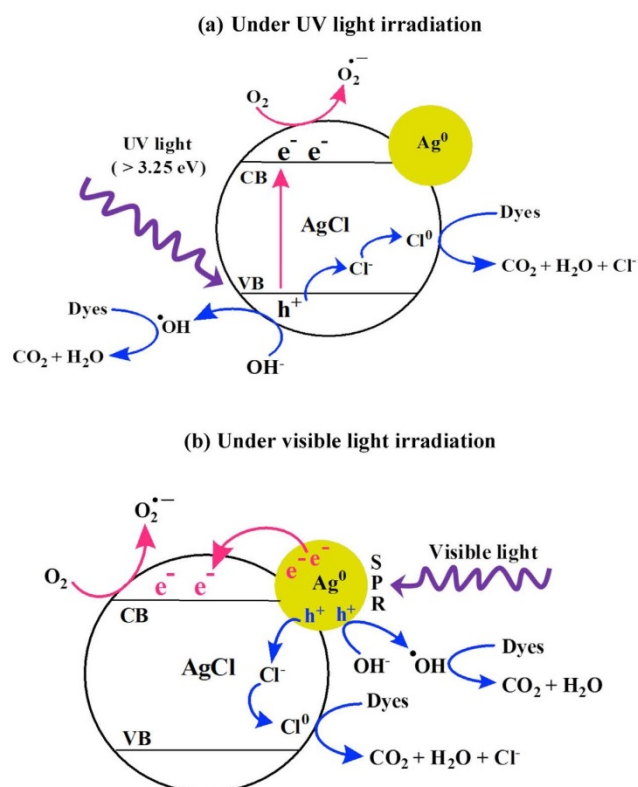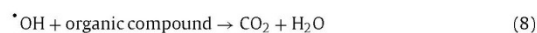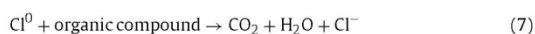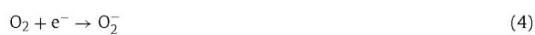
(a) Under UV light irradiation

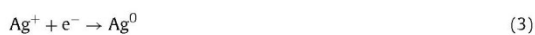### (b) Under visible light irradiation

Fig. 11. Schematic illustration of the Ag/AgCl photocatalytic degradation of organic pollutants under UV and visible light irradiations.

the photodegradation pathway of Ag/AgCl particles under both light sources like what had happened in this work we propose the steps involved as follows.

3.3.2.1. Under UV light. The intrinsic light response of AgCl locates in the UV region, the direct and indirect bandgaps at 5.15 eV (241 nm) and 3.25 eV (382 nm), respectively [30]. The electron–hole pairs are also created in AgCl particles under UV light irradiation (Eq. (1)). The electron–hole pairs may recombine (Eq. (2)), or electron and hole may separate and finally be trapped as reduced Ag atom (Ag^0) (Eq. (3)), or Cl^0 atom (Eq. (5)) [49,54].

$$AgCl \xrightarrow{h\upsilon} AgCl + h^+ + e^- \tag{1}$$

$$h^+ + e^- \rightarrow kT \tag{2}$$

$$Ag^+ + e^- \rightarrow Ag^0 \tag{3}$$

$$O_2 + e^- \rightarrow O_2^- \tag{4}$$

$$Cl^- + h^+ \rightarrow Cl^0 \tag{5}$$

$$OH^- + h^+ \rightarrow {}^{\cdot}OH \tag{6}$$

$$Cl^0 + organic\ compound \rightarrow CO_2 + H_2O + Cl^- \tag{7}$$

$${}^{\cdot}OH + organic\ compound \rightarrow CO_2 + H_2O \tag{8}$$

In general, the photogenerated electrons may also be trapped by O_2 in the solution to form superoxide ions ($O_2{}^-$) (Eq. (4)) which further transform to other reactive oxygen species. These active species also would degrade the dye molecules [22]. Despite this
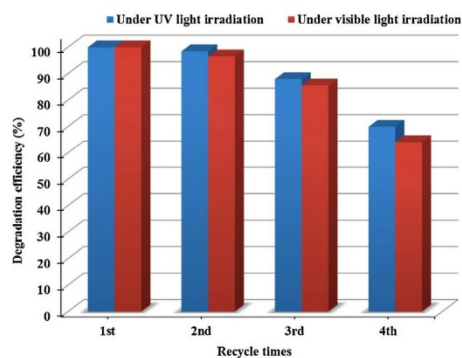

Fig. 12. Recyclability test of urchinlike Ag/AgCl under UV light irradiation (blue), and visible light irradiation (red). (For interpretation of the references to color in this figure legend, the reader is referred to the web version of this article.)
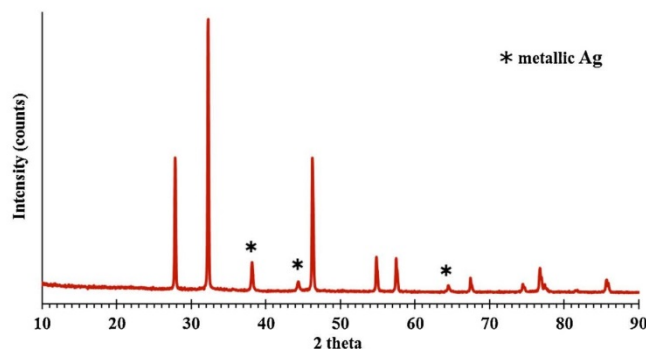
Fig. 13. XRD pattern of urchinlike Ag/AgCl after using four times.

competing electron trapping reaction, however, the presence of metallic Ag atoms seems to indicate that the trapping of free electron by Ag^+ ions (Eq. (3)) located within the matrix may be the more favorable route. While the left over holes diffuse into the AgCl matrix to oxidize Cl^- ions to Cl atoms (Eq. (5)) which are very reactive for oxidizing species in the surrounding solutions (Eq. (7)) [42]. The hole may also oxidize the adsorbed OH^- at the interface to the powerful $^\bullet OH$ radical (Eq. (6)) which subsequently would undergo the dye degradation as well.

The number of metallic Ag atom grows upon going through several repeating cycles of light absorption leading to the formation of clusters of Ag atoms adhered to AgCl aggregates. Hence, the color of AgCl changed during the irradiation process [14].

3.3.2.2. Under visible light. Ag metal nanoparticles absorb a photon from the visible light irradiation through the intrinsic SPR effect leading to electron–hole separation (Eq. (9)) [35,48].
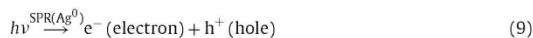
$$h\nu \overset{SPR(Ag^0)}{\longrightarrow} e^- \text{ (electron)} + h^+ \text{ (hole)} \tag{9}$$

The holes eventually would react with Cl^- ions in the AgCl bulk leading to the formation of Cl^0 atoms (like Eq. (5) above) which go on to degrade the dye molecules (like Eq. (7) above) [29,42]. Alternatively, the holes may also undergo the same fate as indicated in Eqs. (6) and (8).

Simultaneously, the excited electrons are transferred to the conduction band of AgCl and trapped by the surface adsorbed molecular oxygen to form the active species of superoxide radical [55] (like Eq. (4) above). Another competing route is its trapping by Ag^+ in the matrix to form Ag^0 (like Eq. (3) above).

The hypothesized pathways for the photocatalytic degradation of dye molecules (organic pollutants) by Ag/AgCl under UV and visible light irradiation are schematically illustrated in Fig. 11a–b, respectively.

3.4. Recyclability test

The urchinlike Ag/AgCl catalyst was subjected to the robustness test in the form of four recycling uses. In the recycle test, the used catalyst was separated and used directly again with fresh dye solution. As shown in Fig. 12, the performances under UV light and visible light were identical in the first use but that of the visible light was slightly lower than the UV light in the subsequent recycling uses. The efficiencies of degradation by both lights gradually decreased in the second use onwards. The color of the used catalyst became darker after each use. The treated water from the first and second uses were clear and colorless while that from the

third use showed very faint color. This means the catalyst can be used comfortably three times before regeneration or being replaced with new fresh catalyst. It should be pointed out that our results here correspond to both the number of uses and the trend of slightly decreasing in efficiency in the recycling uses of Ag/AgCl catalyst appearing in several reports [17,24,55,56]. The data in some of these reports [17,24] were clearly similar to the one shown in Fig. 12. The used catalyst powder was checked with XRD which revealed that it has higher concentration of metallic Ag since the characteristic peaks of metallic Ag was clearly discernible in Fig. 13 as compared to the fresh catalyst in Fig. 3(b). The accumulation of Ag^0 took place (Eq. (3)) as a result from AgCl being irradiated repeatedly over a long time in the recycle test. It seems that if the concentration of metallic Ag is too high beyond its critical value it may give the negative effect. The rationale here could be that since Ag and AgCl have to work in harmony, as shown in Fig. 11, the drastic increase of Ag^0 may cover the surface of AgCl preventing it to receive UV light effectively (Fig. 11(a)) or the layer of Ag^0 may become too thick such that the free electron and hole may not effectively reach the AgCl bulk to drive further reaction (Fig. 11(b)).

4. Conclusions

In summary, we reported a new synthesis method for fabricating nano-haired morphology of AgCl nanostructures by refluxing ammonia solution of $AgNO_3$ followed by $Cl^-–NO_3^-$ exchange. $TiCl_4$ was used as one of the reactant but did not show up in the final product. The product was simply AgCl but with metallic Ag^0 particles mixed in. In this present work, the Ag^+ ion was reduced to Ag^0 atom without any addition of controlling agents or hydrothermal and calcination treatments as have been reported by others. The obtained product, referred to as urchinlike Ag/AgCl nanoparticles from its hairy surfaces, exhibited higher photocatalytic activity than that of commercial Degussa P25, commercial AgCl, and simple AgCl in discoloring orange G dye under UV and visible light irradiation. The electron–hole pairs were created in AgCl lattices under UV irradiation and in metallic Ag bulk under visible light irradiation. These two charged species then react further to the destruction of organic (or dye) molecules resembling those found in TiO_2 photocatalyst.

References

[1] M.R. Hoffmann, S.T. Martin, W. Choi, D.W. Bahnemannt, Chem. Rev. 75 (1995) 69–96.
[2] A. Fujishima, N.T. Rao, D.A. Tryk, J. Photochem. Photobiol., C 1 (2000) 1–21.
[3] S. Klosek, D. Raftery, J. Phys. Chem. B 105 (2001) 2815–2819.
[4] R. Georgekutty, M.K. Seery, S.C. Pillai, J. Phys. Chem. C 112 (2008) 13563–13570.
[5] M. Logar, B. Jancar, S. Sturm, D. Suvorov, Langmuir 26 (2010) 12215–12224.
[6] F.B. Li, X.Z. Li, Chemosphere 48 (2002) 1103–1111.
[7] X.-H. Qi, Z.-H. Wang, Y.-Y. Zhuang, Y. Yu, J.-L. Li, J. Hazard. Mater. B 118 (2005) 219–225.
[8] A. Dawson, P.V. Kamat, J. Phys. Chem. B 105 (2001) 960–966.
[9] S. Sakthivel, M.V. Shankar, M. Palanichamy, B. Arabindoo, D.W. Bahnemann, V. Murugesan, Water Res. 38 (2004) 3001–3008.
[10] M. Jakob, H. Levanon, Nano Lett. 3 (2003) 353–358.
[11] S.K. Ghosh, T. Pa, Chem. Rev. 107 (2007) 4797–4862.
[12] C. Noguez, J. Phys. Chem. C 111 (2007) 3806–3819.
[13] N. Kakuta, N. Goto, H. Ohkita, T. Mizushima, J. Phys. Chem. B 103 (1999) 5917–5919.
[14] H. Cheng, B. Huang, Y. Dai, X. Qin, X. Zhang, Langmuir 26 (2010) 6618–6624.
[15] D. Schurch, A. Currao, S. Sarkar, G. Hodes, G. Calzaferri, J. Phys. Chem. B 106 (2002) 12764–12775.
[16] B.E. Kahn, J. Chem. Educ. 81 (2004) 694–697.
[17] Z. Lou, B. Huang, P. Wang, Z. Wang, X. Qin, X. Zhang, H. Cheng, Z. Zheng, Y. Da, Dalton Trans. 40 (2011) 4104–4110.
[18] P. Wang, B. Huang, X. Qin, X. Zhang, Y. Dai, J. Wei, M.H. Whangbo, Angew. Chem. Int. Ed. 47 (2008) 1–4.
[19] W. Wang, W. Lu, L. Jiang, J. Colloid Interface Sci. 338 (2009) 270–275.
[20] L. Kuai, B. Geng, X. Chen, Y. Zhao, Y. Luo, Langmuir 26 (2010) 18723–18727.
[21] B. Ma, J. Guo, L. Zou, W.L. Dai, K. Fan, Chin. J. Chem. 29 (2011) 857–859.
[22] J. Jiang, L. Zhang, Chem. Eur. J. 17 (2011) 3710–3717.
[23] C. An, R. Wang, S. Wang, X. Zhang, J. Mater. Chem. 21 (2011) 11532–11536.
[24] B. Ma, J. Guo, W.L. Dai, K. Fan, Appl. Catal., B 130–131 (2013) 257–263.
[25] M.A. Kanjwal, N.A.M. Barakat, F.A. Sheikh, W.I. Baek, M.S. Khil, H.Y. Kim, Fibers Polym. 11 (2010) 700–709.
[26] S. Ding, J. Guo, X. Yan, T. Lin, K. Xuan, J. Cryst. Growth 284 (2005) 142–148.
[27] Y. Tian, H.-B. Lu, L. Liao, J.-C. Li, Y. Wu, Q. Fu, Physica E 41 (2009) 729–7337.
[28] J. Ng, X. Wang, D.D. Sun, Appl. Catal., B 110 (2011) 260–272.
[29] M. Choi, K-H. Shin, J. Jang, J. Colloid Interface Sci. 341 (2010) 83–87.
[30] L. Han, P. Wang, C. Zhu, Y. Zhai, S. Dong, Nanoscale 3 (2011) 2931–2935.
[31] M. Zhu, P. Chen, W. Ma, B. Lei, M. Liu, ACS Appl. Mater. Interfaces 4 (2012) 6386–6392.
[32] Y. Tang, Z. Jiang, J. Deng, D. Gong, Y. Lai, H.T. Tay, I.T.K. Joo, T.H. Lau, Z. Dong, Z. Chen, ACS Appl. Mater. Interfaces 4 (2012) 438–446.
[33] Y. Tang, Z. Jiang, Q. Tay, J. Deng, Y. Lai, D. Gong, Z. Dong, Z. Chen, RSC Adv. 2 (2012) 9406–9414.
[34] C. Wang, X. Zhang, C. Shao, Y. Zhang, J. Yang, P. Sun, X. Liu, H. Liu, Y. Liu, T. Xie, D. Wang, J. Colloid Interface Sci. 363 (2011) 157–164.
[35] H. Xu, H. Li, J. Xia, S. Yin, Z. Luo, L. Liu, L. Xu, ACS Appl. Mater. Interfaces 3 (2011) 22–29.
[36] B.I. Kharisov, O.V. Kharissova, M. Jose-Yacaman, Ind. Eng. Chem. Res. 49 (2010) 8289–8309.
[37] L. Song, Q. Gaowu, P. Wenli, Z. Liang, Rare Met. 30 (2011) 157–160.
[38] J. Rogez, A. Garnier, P. Knauth, J. Phys. Chem. Solids 63 (2002) 9–14.
[39] S.A. Amin, M. Pazouki, A. Hosseinnia, Powder Technol. 196 (2009) 241–245.
[40] K.V. Baiju, S. Shukla, K.S. Sandhya, J. James, K.G.K. Warrier, J. Phys. Chem. C 111 (2007) 7612–7622.
[41] R. Dong, B. Tian, C. Zeng, T. Li, T. Wang, J. Zhang, J. Phys. Chem. C 117 (2013) 213–220.
[42] L. Dong, D. Liang, R. Gong, Eur. J. Inorg. Chem. (2012) 3200–3208.
[43] F. Zhang, Y. Zheng, Y. Cao, C. Chen, Y. Zhan, X. Lin, Q. Zheng, K. Weia, J. Zhu, J. Mater. Chem. 19 (2009) 2771–2777.
[44] L. Han, P. Wang, C. Zhu, C. Zhai, S. Dong, Nanoscale 3 (2011) 2931–2935.
[45] I. Pastoriza-Santos, L.M. Liz-Marzan, Nano Lett. 2 (2002) 903–905.
[46] M.J. Mulvihill, X.Y. Ling, J. Henzie, P. Yang, J. Am. Chem. Soc. 132 (2010) 268–274.
[47] M. Rycenga, C.M. Cobley, J. Zeng, W. Li, C.H. Moran, Q. Zhang, D. Qin, Y. Xia, Chem. Rev. 111 (2011) 3669–3712.
[48] M. Lanz, D. Schuĕrch, G. Calzaferri, J. Photochem. Photobiol., A 120 (1999) 105–117.
[49] J. Cao, B. Xu, B. Luo, H. Lin, S. Chen, Appl. Surf. Sci. 257 (2011) 7083–7089.
[50] N. Zhang, S. Liu, X. Fu, Y.-J. Xu, J. Phys. Chem. C 115 (2011) 9136–9145.
[51] H. Wang, Y. Bai, Q. Wu, W. Zhou, H. Zhang, J. Li, L. Guo, Phys. Chem. Chem. Phys. 13 (2011) 7008–7013.
[52] G. Tian, Y. Chen, W. Zhou, K. Pan, C. Tian, X.R. Huang, H. Fu, Cryst. Eng. Commun. 13 (2011) 2994–3000.
[53] H. Huang, X. Li, Z. Kang, Y. Liu, H. Li, X. He, S. Lian, J. Liu, S.-T. Lee, Dalton Trans. 39 (2010) 10593–10597.
[54] Z. Yan, G. Compagnini, D.B. Chrisey, J. Phys. Chem. C 115 (2011) 5058–5062.
[55] Y. Tang, Z. Jiang, G. Xing, et al., Adv. Funct. Mater. (2014), http://dx.doi.org/10.1002/adfm.201203379.
[56] M. Zhu, P. Chen, M. Liu, J. Mater. Chem. 21 (2011) 16413–16419.

Paper II

Flower-like Ag/AgCl microcrystals: Synthesis and photocatalytic activity

Hasan Daupor and Sumpun Wongnawa*

# Flower-like Ag/AgCl microcrystals: Synthesis and photocatalytic activity

Hasan Daupor, Sumpun Wongnawa[*]

Department of Chemistry and Center of Excellence for Innovation in Chemistry, Faculty of Science, Prince of Songkla University, Hat Yai, Songkhla 90112, Thailand

HIGHLIGHTS

- Interesting transformation of microcrystals Ag/AgCl from concave cube via Rubik's cube to flower-like shape.
- The first to use VAM as morphology control reagent.
- High photocatalytic activity under visible light irradiation.

GRAPHICAL ABSTRACT
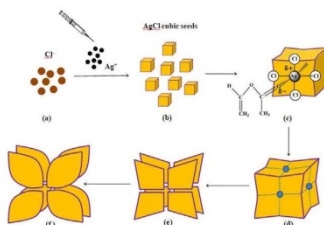
ABSTRACT

Silver/silver chloride (Ag/AgCl) composites with a novel flower-like morphology were prepared via a hot precipitation assisted by the vinyl acetate monomer (VAM) route. An aqueous solution of $AlCl_3$ was mixed with the vinyl acetate monomer and acetic acid before adding a $AgNO_3$ solution at a temperature of 100 °C. The octapod shaped flower-like Ag/AgCl particles (or *"flower-like Ag/AgCl" hereinafter*) has eight petals each of which was about 7–11 μm in length. The flower-like octapods were formed by preferential overgrowth along the <111> directions of the cubic seeds. Detailed studies of the growth process at different $AlCl_3$ concentrations revealed that the concave cube developed into a Rubik's cube where eight corners grew further into the flower-like structures. The VAM and acetic acid concentration strongly affected the growth of the Ag/AgCl to the flower-like structure and their optimum concentrations were determined. The morphologies of these particles were carefully examined by scanning electron microscopy (SEM). The crystal structures and orientation relationship were characterized by X-ray diffraction (XRD), X-ray photoelectron spectroscopy (XPS), and UV–visible diffused reflectance spectroscopy (DRS). The flower-like Ag/AgCl microcrystals were tested for their photocatalytic degradation of orange G dye (OG) catalyzed by visible light. From comparative test runs, the flower-like Ag/AgCl exhibited better photocatalytic activity than simple and commercial Ag/AgCl particles.

© 2015 Elsevier B.V. All rights reserved.

1. Introduction

Synthetic control of morphology has been an important 'magic' in the field of materials chemistry to help fine tune several properties such as the electronic, optical, and catalytic properties of semiconductor nanocrystals [1,2]. The intrinsic properties of

* Corresponding author.
  E-mail address: sumpun.w@psu.ac.th (S. Wongnawa).

90

semiconductor nanostructures can be tailored by controlling their size, shape, composition, crystallinity, and structures. Particular emphasis has recently been placed on the control of shape, because in many cases it has allowed for the creation of a greater versatility [3]. Shape control has recently been in the limelight for researches into noble metals and other inorganic materials. The shape also controls the facets and thus the surface structure of a metal nanocrystal as well as its catalytically active sites, such as, its corners, edges, steps, etc. [4,5]. Several shapes of metals have been reported thus far, for example, Au spheres [6], Ag plates [7], Pd cubes [8], and Ag rods [9]. In addition to these simple shapes, classes of flower-like or star-shaped structures have also been synthesized, such as, an Au star [10], and nanoflowers of Pd, Pt, and Ag [11]. Of even more interest, were Ag nanoparticles that ranged in size from 2 to 20 nm and exhibited unique optical properties of quantum dots (QDs) that could strongly absorb and scatter light through the collective oscillations of conduction band electrons confined within a metallic Ag quantum dot (AgQD). This oscillation was called surface plasmon resonance (SPR) [12,13]. Tuning the nanostructure size, shape, dielectric medium, and surface adsorbed species strongly affected this SPR [14]. Quantum dot semiconductors not only cover noble metals but also include elements of groups II–VI, IV–VI, or III–V in the periodic table such as ZnS quantum dots doped with Fe^{3+} that found applications as a photocatalyst for the removal of malachite green and victoria blue R [15,16]. All of this research work has been essential for applications in heterogeneous catalysis.

Among the inorganic materials, Ag/AgCl is attractive because of its SPR characteristics inherited from its metallic Ag nanoparticles that exhibit a high absorption coefficient over a broad visible range [17,18]. It has found potential applications in visible light-driven catalytic oxidation reactions and in the photodegradation of organic pollutants. A variety of morphologies of AgCl have been reported recently. For example, Ag/AgCl core–shell nanowires were synthesized from the oxidation reaction of Ag nanowires and $FeCl_3$ at room temperature. The oxidation reaction was explained based on the lower redox potential of Fe^{3+} ions compared to that of the Ag species so that electrons migrated from the Ag nanowires to the Fe^{3+} ions to form the AgCl nanowires. This oxidation process was also attempted with other metal chlorides such as a $CuCl_2$ solution to fabricate a novel nanoplate/nanowire Ag/AgCl [19]. Uniform heart-shaped AgCl was fabricated in the presence of ethylene glycol (EG) and polyvinyl pyrrolidone (PVP) during heating at 140 °C for 7 h. The heart-like morphology arose from the merging of four cubes by oriented-attachment [20]. The ion-exchange reaction between NaCl with Ag_2WO_4 microrods (as the template) produced the rod-like morphology of Ag/AgCl with a rough surface [21].

Many recent efforts have focused on the 3-dimensional structures of AgCl semiconductor materials. Lou and co-workers presented a wet chemical oxidation approach to synthesize AgCl as a concave cube using $NaClO_2$ as an oxidizer for an Ag plate immersed in a NaCl solution at room temperature. (NaCl was the source of Cl ions.) The AgCl concave cube with high-index facets has been shown to exhibit a higher photocatalytic activity than the regular cube that had smooth {001} facets in the decomposition of methyl orange (MO) under visible light because of the existence of a large number of atomic steps, edges, and kinks that accompanied the high-index facets. An AgCl concave cube was formed by preferential overgrowth along the <111> and <110> directions when the reaction time or NaCl concentration was increased. It was of interest, that the concave cube grew only along the <111> direction while the {100} facets disappeared to form a flower-like AgCl at a high NaCl concentration [22]. Furthermore, at an even higher concentration of $NaClO_4$, NaCl, and citric acid, a 3D AgCl hierarchical

superstructure was formed by preferential growth along the <111> direction of the cubic seeds [23].

At present the flower-like octagonal AgCl microstructures with preferential growth along the <111> directions has been synthesized only via the hydrothermal method. A branch-breaking phenomenon of large dendrite crystal, that was composed of a sub-branch, generated their fragmentation, assembly, dissolution, and recrystallization to form small flower-like octagonal crystals [24]. However, the report of a flower-like Ag/AgCl with a more exotic morphology has not yet appeared. In this communication, we report a new efficient strategy for the direct synthesis of highly monodispersed AgCl particles with the assistance of vinyl acetate molecules. In a typical synthesis, the Rubik's cube shape of the AgCl was obtained by using a precipitation process during heat treatment using $AlCl_3$ as a Cl source. To the best of our knowledge, this is the first report of a Rubik's cube shaped AgCl. By changing the experimental conditions, octahedrons, hexapods, and octapods were also obtained.

2. Experimental

2.1. Materials

The main chemicals were: aluminum chloride ($AlCl_3$ anh., AR, Merck), silver nitrate ($AgNO_3$, AR, Merck), glacial acetic acid (CH_3COOH, AR, BDH), vinyl acetate monomer (VAM, AR, Merck), and orange G dye (Fluka, $C_{16}H_{10}N_2Na_2O_7S_2$, MW 452.38 g/mol). All the chemicals were used directly without further purification. Deionized (DI) water was used in all experiments.

2.2. Synthesis of the flower-like Ag/AgCl microstructures

The preparation of flower-like Ag/AgCl is described as follows.

A yellowish solution of 10 g of solid anhydrous $AlCl_3$ (2.50 M) was prepared in 30 mL of DI water and placed in a water bath (at room temperature) to help dissipate heat during dissolution. To this solution, 10 mL of VAM was added and transferred to a 250 mL three-necked flask for refluxing for 3 h at 75 °C. Acetic acid solution (8.72 M CH_3COOH, 80 mL) was then added to this homogenous solution and stirred at room temperature for 1 h to obtain a clear colorless solution.

The above solution was heated to 100 °C with stirring and maintained at this temperature for 5–10 min. Then, 30 mL of 20 mM $AgNO_3$ solution was added to this solution held at 100 °C at the rate of 0.3 mL/min from a burette equipped with an infusion set to help control the flow rate. When the product began to appear it became dispersed in the hot solution. The reaction mixture was maintained at 100 °C with vigorous stirring for another 30 min until all the $AgNO_3$ was added. At the end of reaction, the product was collected and washed thoroughly with ethanol and DI water to remove VAM. After drying at 40 °C for about 6 h, the bluish purple powder of flower-like Ag/AgCl was obtained. (See photograph of this powder in the Supplementary Material.)

Various key parameters were then varied, i. e., the concentrations of $AlCl_3$, CH_3COOH, the amount of VAM, and the reaction temperatures, while the rest of the procedure remained unchanged (see Table 1).

2.3. Characterization of samples

The morphology and crystalline structure of the samples were examined by a scanning electron microscope (SEM, Quanta 400, FEI). The elemental composition was analyzed by an energy dispersive spectrometer (EDS) equipped with the SEM microscope system. The phase constitution of the samples was characterized by

3

Table 1
Summary of the experimental conditions used.

No.	CH_3COOH (M)	VAM (mL)	Temperature (°C)	Morphology and characteristics	Products	Compounds of similar morphology [Ref.]
1	8.72	10	25	Irregular	Fig. 7a	
2	8.72	10	50	Irregular	Fig. 7b	
3	8.72	10	70	Some hexapods	Fig. 7c	Ag_2O [25]
4	0	0	100	Octahedron	Fig. 8a	
5	0	10	100	Flower-like hexapod	Fig. 8b	Cu_2O and Au/Cu_2O [26]
6	4.36	10	100	Hexapod with square tips	Fig. 9a	ZnO [27]
7	8.72	10	100	Octapod flower-like	Figs. 2d and 3	
8	13.07	10	100	Hexapod with dagger-like pods	Fig. 9c	Cu_2O [28]
9	16.34	10	100	Disorderedly growth and loss of flower-like form	Fig. 9d	
10	8.72	5	100	Octapod flower-like with floral leaf	Fig. 10a	
12	8.72	15	100	Hexapod with large square tips	Fig. 10b	
13	8.72	20	100	Transformation from flower-like to hollow structure like zeolite	Fig. 10d	Cu_2O [28]

No. 7 shows the main conditions used in this work.

X-ray diffraction (XRD) using a Philips PW 3710 powder diffractometer (PHILIPS X'Pert MPD, The Netherlands), Cu Kα (Ni filtered) radiation $\lambda = 1.5406$ Å. The diffractograms were recorded in the 2θ range of 5–90° with a 2θ step of 0.05° and a step time of 1 s. X-ray photoelectron spectroscopy (XPS) analysis was carried out using the AXIS ULTRADLD, Kratos Analytical, Manchester, UK. All binding energies were referred to the C 1s peak at 285.0 eV of the surface adventitious carbon. The diffused reflectance spectra (DRS) were measured by a UV 2401 spectrometer (Shimadzu, Japan) over the range of 200–800 nm using $BaSO_4$ as the reflectance standard material.

2.4. Evaluation of photocatalytic activity

The photocatalytic degradation of the orange G dye (OG) was conducted under visible light at room temperature with a mixture of 0.1 g Ag/AgCl powder and 100 mL of 2.5×10^{-5} mol/L OG dye in a 150 mL beaker. The solution was kept in the dark for 30 min to allow an adsorption–desorption equilibration before irradiation with visible light in a reaction chamber (75 × 75 × 75 cm) fitted with five 18 W fluorescence tubes as a visible light source for the photocatalytic reaction. The concentration of OG was determined by a UV–visible spectrophotometer (UV 2600, Shimadzu, Japan). After every 30 min of irradiation, 3 mL of the mixture was collected and centrifuged. Some of the clear liquid was removed to measure the concentration change of the OG, monitored at λ_{max} 480 nm. The controlled experiments, without catalyst or light, were also performed to confirm that the degradation of dye depended on the presence of both light and the Ag/AgCl catalyst powder.
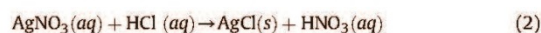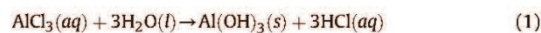
3. Results and discussion

3.1. Growth process of the flower-like Ag/AgCl

In order to study the growth process of the flower-like Ag/AgCl from its concave cubic form through Rubik's cube, a series of experiments were performed with 30 mL of differing concentrations of $AlCl_3$ while keeping the concentration of the VAM and CH_3COOH solutions unchanged (10 mL of VAM and 80 mL of 8.72 M CH_3COOH), ($AlCl_3$ was used as the source of Cl⁻ ions). All facet structures and growth directions were confirmed by crystallographic orientation of the AgCl as shown in Fig 1. Starting from a 0.75 M $AlCl_3$ solution in Fig. 2a, some 2.4–2.7 μm sized cubic crystals were formed with a concave face at the center of six {100} facets. When the 1.25 M $AlCl_3$ solution was used the concave faces became more distinct and the cube looked as though it was about to be partitioned into eight smaller cubes by three perpendicular

intersecting planes. The intersecting point at the center of the concave face now appeared as a tiny cavity (Fig. 2b). The size of the crystals at this point was about 5.0–6.5 μm. Fig. 2c shows that when 1.75 M $AlCl_3$ was used, each side face – the {100} face – of the concave cubic AgCl looked as though it was marked and partitioned by a saw into four pieces. In the 3D view, the concave cubic now turned into a shape like the Rubik's cube – the first to be reported here. The size of the Rubik's cube was about 7.0–7.5 μm. At the highest concentration of $AlCl_3$ solution (2.5 M), the AgCl crystals grew only along <111> directions to form the flower-like AgCl structures and {100} facets diminished completely as shown in Fig. 2d. The size of the 3D microflowers were about 15–22 μm. The effect of increasing the concentration of $AlCl_3$ as displayed in Fig. 2 indicated that the Cl⁻ ion played a critical role in controlling the morphologies of the AgCl growth to form the flower-like octapod AgCl structure. The product obtained with 2.5 M $AlCl_3$ was chosen for further studies because of its intricate shape that seemed to be fully developed. During the growth process, the disappearance of the mass at the center of the {100} facets of the Rubik's cube (Fig. 2c) was possibly due to the presence of VAM, that could interact more strongly with the {100} sides than with the {111} ends. The VAM could serve to reduce the driving force for the cubic formation through its selective interaction with the {100} planes. The selective adsorption of VAM on the {100} facets would lead to the preferential addition of Ag and Cl atoms to the {111} facets. Therefore, the Rubik's cube could readily grow into a longer petal that were as long as tens of micrometers because its side surfaces were tightly restricted by the VAM molecules, similar to that previously found with PVP [29,30].

The possible reactions for the precipitation of AgCl microcrystals can be described by the Equations (1)–(2). The assembling of the Ag⁺ and Cl⁻ ions into the flower-like shape as assisted by VAM is illustrated as in Scheme 1.

$$AlCl_3(aq) + 3H_2O(l) \rightarrow Al(OH)_3(s) + 3HCl(aq) \qquad (1)$$

$$AgNO_3(aq) + HCl(aq) \rightarrow AgCl(s) + HNO_3(aq) \qquad (2)$$

The combination of Ag⁺ and Cl⁻ produced AgCl cubic seeds (Scheme 1: a → b). This cubic seed then grew into the concave cubic shape with a molecule of VAM associated on the {100} facet via an electrostatic interaction (Scheme 1c). The presence of VAM blocked further growth along the {100} facet but not in other directions – especially the <111> direction (Scheme 1: c → d). At a still higher $AlCl_3$ concentration, the growth in the <111> direction was immense and swelled into a 3D shape but the growth along the <100> was completely halted, as a result, a Rubik's cube was
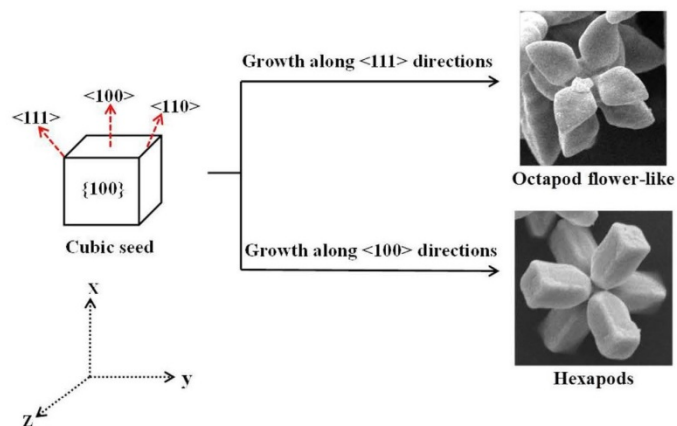
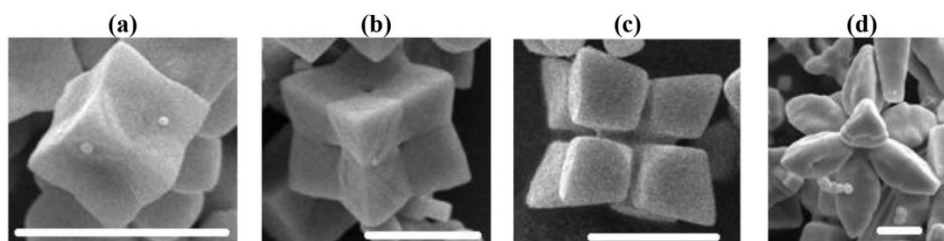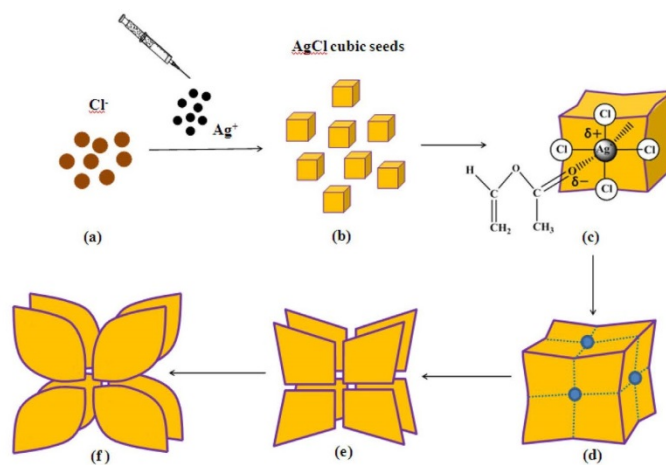**Fig. 1.** Crystallographic orientation of the cubic seeds of AgCl.

Fig. 2. SEM images of samples synthesized using 10 mL VAM, 8.72 M CH$_3$COOH with different AlCl$_3$ concentrations: (a) 0.75 M, (b) 1.25 M, (c) 1.75 M, and (d) 2.50 M at 100 °C. (All scale bars ~ 5 μm).

Scheme 1. Crystal growth of the flower-like AgCl in the presence of VAM.

formed (Scheme 1: d → e), and was finally converted into the flower-like shape (Scheme 1f).

3.2. EDX-mapping analysis

The elemental composition of the flower-like Ag/AgCl was determined using EDX the spectrum of which is shown in Fig. 3a. Only the peak of the Ag and Cl elements was detected in the sample, and this result was in good agreement with the XRD analysis. Fig. 3b and c shows the distribution and relative proportions (intensity) of the Ag and Cl elements over the investigated area. Elemental semi-quantitative analysis revealed that the atomic ratio of Ag:Cl was approximately 1.06:1, similar to that in the literature [31]. (The appearance of the Au and C peaks in the spectrum was due to the Au coating and the substrate, respectively, that was used for the preparation of the SEM sample.)

3.3. XRD

The X-ray diffraction patterns indicated two distinct growth patterns in the AgCl crystallites that were a function of the $AlCl_3$ concentration (Fig. 4). All diffraction peaks matched with the face-centered cubic structure of AgCl (JCPDS Card file no. 31-1238). The diffraction peaks of different morphologies hardly changed but their intensities were enhanced. Similar results had been observed by other research groups [32]. This result was useful for examining the relative intensities of the diffraction peaks that were relevant to the measures of the degree of orientation. In the cubic AgCl crystal system, generally, the XRD intensity of (111) was lower than that of the (220) peak [33]. The relative intensities between (111) and (220) was calculated in
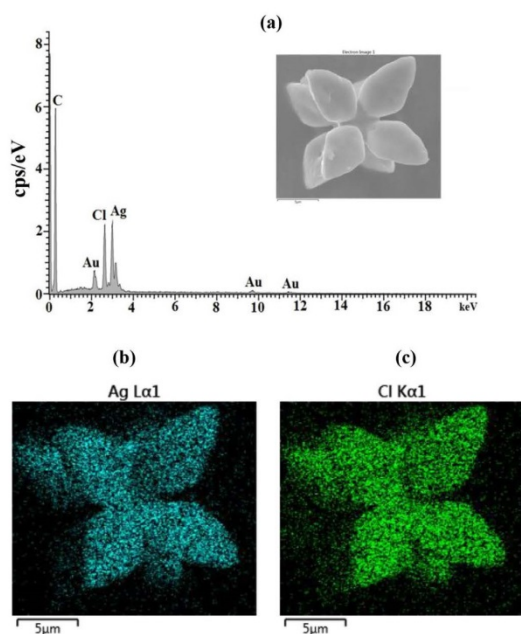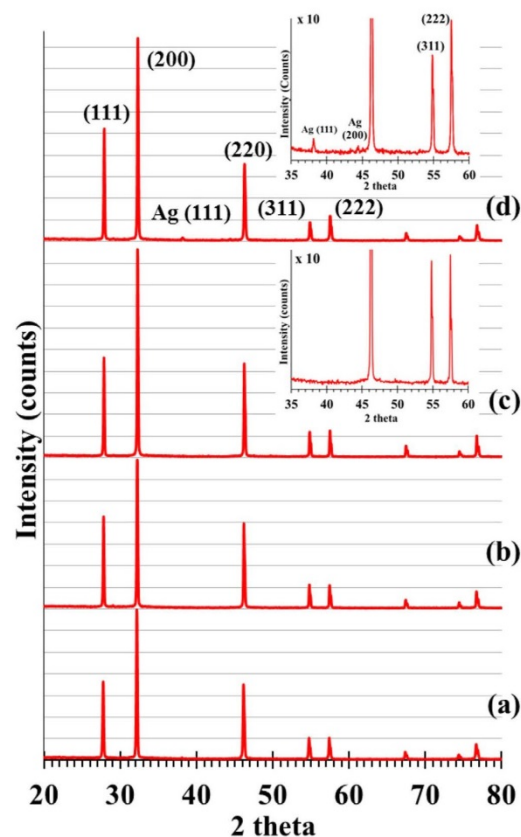

Fig. 4. The XRD patterns of samples: (a) the concave cubic AgCl with flat {100} facets, (b) the octapod AgCl, (c) the Rubik's cube AgCl, and (d) the flower-like Ag/AgCl. (Insets in panel c and d show the expanded XRD patterns.)

Fig. 3. (a) EDX spectrum of the flower-like Ag/AgCl, (b)–(c) mapping analyses of Ag and Cl.

order to study their relationships among the different AgCl microstructures. The ratios the I_{111}/I_{220} of the concave cubes, octapod, Rubik's cube, and flower-like AgCl were 1.03, 1.23, 1.23, and 1.49, respectively, which were all greater than the value of 0.86 for the standard powder sample of a face centered cubic AgCl (JCPDS Card file no. 31-1238). It is worth noting, that this value of the AgCl concave cubes (Fig. 4a) was the smallest among all the microstructures and indicated the lowest value of I_{111}. Referring to Figs. 1 and 2, one can see that the concave cube has not yet started to grow along <111> directions. The population along <111> directions was still low. When the cubics grew into octapods and the Rubik's cubes (Fig. 2b and c, and their respective Fig. 4b and c), all eight corners or the {111} facets gradually grew but not for the edges of cube or the {110} facets. This observation of the {111} facet was clear in the flower-like Ag/AgCl samples (Fig. 2d) where the (111) peak intensity of the flower-like Ag/AgCl became obviously stronger than the intensity of the (220) peak. These observations implied that the AgCl microstructures grew along the <111> direction very well and might have generated overgrowth directions [34]. The I_{111}/I_{220} value of the flower-like AgCl was the largest due to the extra growth along this direction. In conclusion, the conversion from
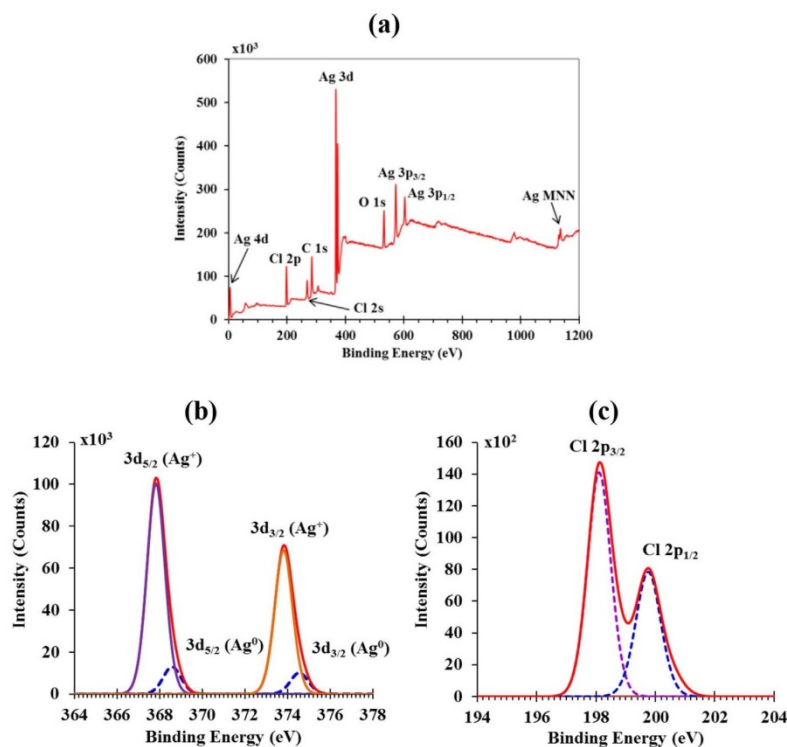
Fig. 5. XPS spectra of the flower-like Ag/AgCl: (a) survey scan, (b) Ag 3d, and (c) Cl 2p.

the concave cubes to the flower-like AgCl could be visualized as occurring through the dissolution and overgrowth of the relevant crystal planes [35]. To form the flower-like octapods, the required conditions were: overgrowth on the {111} facet and a simultaneous dissolution of both the {110} and {100} facets. As the crystals grew larger, other high-index facets would be similarly affected. Therefore, as shown in the insets to Fig. 4c and d, the relatively slightly stronger (222) reflection than for the (311) could be seen and this was attributed to the abundance of the {222} facet that had a stepped surface composed of {111} terrace [36]. For a comparison, under normal conditions, the peak intensity of the (222) facet was lower than that of the (311) facet of the face centered cubic AgCl (JCPDS Card file no. 31-1238).

In addition, two very weak diffraction peaks at 38.1° and 44.4° (the inset of Fig. 4d) were identified (JCPDS Card file no 65-2871) as the (111) and (200) planes, respectively, of metallic Ag present on the surface of AgCl [37]. The content of metallic Ag, very likely produced by the heat treatment during the process, but was very low due to its very weak peak. The diffraction peaks of the metallic Ag, however, were not detected in the other three samples (Fig. 4a–c), possibly, because the Ag content was below the detection limit of the XRD equipment.

From the XRD data, the crystallite size can be estimated from the Debye-Scherrer formula, $D = K\lambda/\beta\cos\theta$, where K is a constant with an accepted value of 0.9, λ is X-ray wavelength (0.154 nm), β is FWHM, θ is the half diffraction angle, and D is the crystallite size. From this calculation, the crystallite size of the flowerlike octapod Ag/AgCl samples was *ca.* 41 nm.

3.4. XPS

The X-ray photoelectron spectroscopy study (XPS) was used to study the atomic state of the silver (Ag) in the produced flower-like Ag/AgCl microstructures, as shown in Fig. 5. The instrument was calibrated with C 1s (285.0 eV). The wide survey spectrum is shown in Fig. 5a. The Ag 3d peaks (Fig. 5b) of the flower-like Ag/AgCl microstructures consisted of two peaks at *ca.* 367.8 and 373.8 eV that were ascribable to the Ag $3d_{5/2}$ and Ag $3d_{3/2}$ binding energies, respectively. These bands, on a closer examination, were slightly less than a perfect symmetrical shape and could be further deconvoluted into two peaks, corresponding to Ag^0 and Ag^+, respectively. The peaks at 368.5 and 374.5 eV can be attributed to Ag^0, whereas the peaks at 367.8 and 373.8 eV were attributed to the Ag^+ of AgCl [38]. Based on the deconvoluted results of the Ag 3d spectra, the semi-quantitatively surface atomic ratio between the Ag^0 and Ag^+ was calculated to be 1:7.26. These results further indicated the existence of Ag^0 species in the obtained flower-like microstructures. It clearly indicated that some of the Ag^+ was gradually transformed to metallic Ag (Ag^0) because of the heat treatment. That is, AgCl was transformed to be an Ag/AgCl composite photocatalyst with no need for a light reduction treatment before photocatalysis. Metallic Ag particles were important parameters for the materials to exhibit a good photocatalytic activity under irradiation with visible light. Fig. 5c shows the Cl species with the binding energy of Cl $2p_{3/2}$ and Cl $2p_{1/2}$ at about 198.1 and 199.8 eV, respectively [39]. Hence, the XPS analysis combined with the results from the XRD and EDX verified the formation of the Ag/
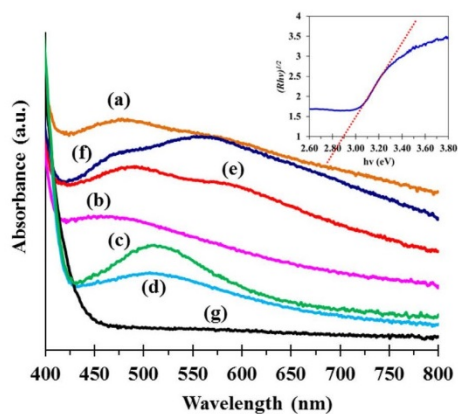
AgCl composite containing a trace of metallic Ag (Ag^0) in the bulk of the AgCl.

3.5. DRS

The absorption in the visible-light region of the Ag/AgCl in Fig. 6 can be attributed to the plasmonic absorption of the metallic Ag nanoparticles or the surface plasmon resonance (SPR) [40]. The SPR band intensity and wavelength depended on factors such as the metal type, particle size, shape, structure, composition, and the dielectric constant of the surrounding medium [41]. The samples of Rubik's cubes (Fig. 6a), had an irregular shape (Fig. 6b), the spherical shape of the simple Ag/AgCl (Fig. 6c), and the cubic shape of the commercial Ag/AgCl (Fig. 6d) showed only one absorption peak located at around 500 nm, that was attributed to the SPR effect of the Ag nanoparticles generated on the AgCl particle surfaces [42,43]. Meanwhile, the octahedron (Fig. 6e) consisted of a strong absorption peak at 500 nm with a weak shoulder peak around 600 nm. For the flower-like Ag/AgCl (Fig. 6f), there was a distinct peak at *ca.* 560 nm with a shoulder at *ca.* 470 nm due to the relatively large sizes of these crystals. The positions of these bands exhibited a progressive red-shift of the resonance peaks (from 470 to 560 nm) as the particle size increased, that was caused by the growth of the Ag particle size [44]. The indirect band gap energies of the flower-like Ag/AgCl were estimated from a plot of $(Rh\nu)^{1/2}$
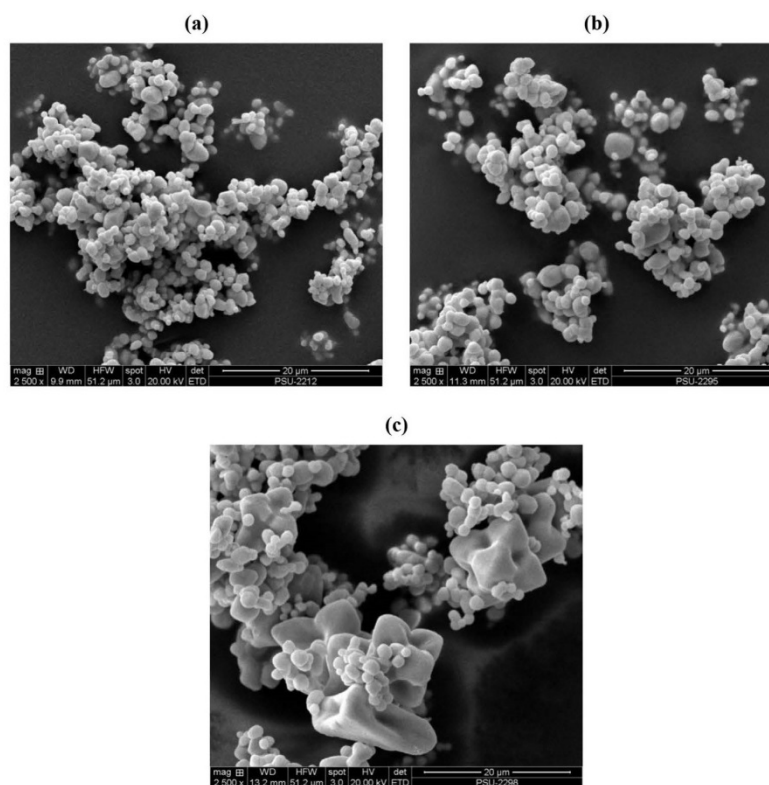

Fig. 6. UV–vis diffused reflectance spectra of the as-synthesized AgCl with different morphologies: (a) Rubik's cubes, (b) irregular, (c) sphere, (d) cube, (e) octahedron, (f) flower-like Ag/AgCl, and (g) pure commercial AgCl. (Inset: plot of $(Rh\nu)^{1/2}$ versus the $h\nu$ of the flower-like Ag/AgCl sample).

Fig. 7. SEM images of the AgCl samples in the presence of 2.5 M AlCl$_3$, 10 mL VAM, and 8.72 M CH$_3$COOH with different reaction temperatures: (a) 25 °C, (b) 50 °C, and (c) 70 °C.
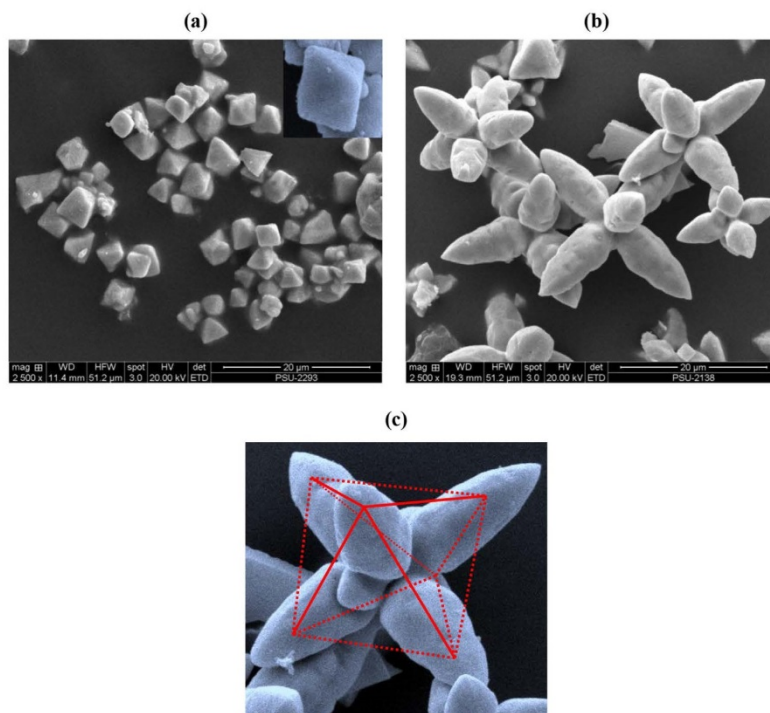
(a)   (b)

(c)

Fig. 8. SEM images of the AgCl samples prepared from 2.5 M AlCl₃ and: (a) 0 mL, (b) 10 mL (b) of VAM at 100 °C. In (c) showing the matching octahedron with a crystal from (b).

versus $h\nu$ according to the Kubelka-Munk function (inset of Fig. 6), where R was the absorption coefficient and $h\nu$ was the associated photon energy [45]. The estimated band gap energy was 2.88 eV; this value agreed with the reported band gap energy for AgCl [46]. The investigated AgCl crystals showed a narrower band gap than that of the conventional AgCl crystals at 3.25 eV [47].

3.6. The effects of heat treatment

In order to clarify the morphology during the evolution of the AgCl flower-like octapod structures, temperature-dependent experiments were performed in the presence of VAM (10 mL) and CH₃COOH solution (80 mL, 8.72 M) without changing other experimental parameters. Typical SEM images of the products prepared at various temperatures are shown in Fig. 7. At room temperature and 50 °C, similar irregular particles were obtained (Fig. 7a and b). At 70 °C, some hexapods began to appear (Fig. 7c) that were possibly produced with a depressing of the {111} facets of the octahedron similar to the systematic evolution of the Ag₂O nanocrystals from the cubic to the hexapod structures [25]. (See Table 1 for the summary of the synthesized morphologies of other materials.) Upon increasing the reaction temperature to 100 °C in the absence of both VAM and CH₃COOH this led to the formation of complete octahedron shapes with an average size of 3.5–5.0 μm (Fig. 8a). It was of interest that, the microflowers were not formed because there was no VAM around to intervene in the growth process. Further experiments showed that with 10 mL of VAM but without the CH₃COOH solution, the octahedron shapes developed to the hexapod flower-like structures with an average size of

10–12 μm as shown in Fig. 8b. Hexapods of the flower-like AgCl grew from the octahedron seeds along the <100> directions [48]. Each leg of the hexapod pointed to the vertex of an octahedron as shown in Fig. 8c. This indicated that the morphologies of the AgCl crystals were controlled under the cooperation of the heat treatment and the additive reagents. These observations indicated that VAM has an interesting ability to control the growth morphology and orientation.

3.7. The influence of the acetic acid solution

In the above paragraph, we found that both the VAM and acetic acid solution helped to induce the morphological transformation of the irregular AgCl shape to the flower-like shape during heat treatment. To distinguish the role of the VAM and CH₃COOH solution, these two chemicals were varied individually and the results are shown in Fig. 9 with the enlarged inset view.

The first experiment used 10 mL of VAM and 80 mL of 4.36 M CH₃COOH solution. The hexapods with square tips had an average pod length of 5 μm and a width of about 1 μm (Fig. 9a). These hexapods might transform from hexapods with the sharp pointed tips displayed in Fig. 8b. The top facet of the pod was square as shown in Fig. 9b and this supported the expected growth habit of the six cubic {100} facets of the cubic seed. Some of the hexapods (in red circles, Fig. 9a) had several pods growing from the same site that were similar to the shape of the flower- and the cactus-like nanostructures found in ZnO and CdS [27]. In this case, each pod had a smooth surface so it better matched the flower-like type.

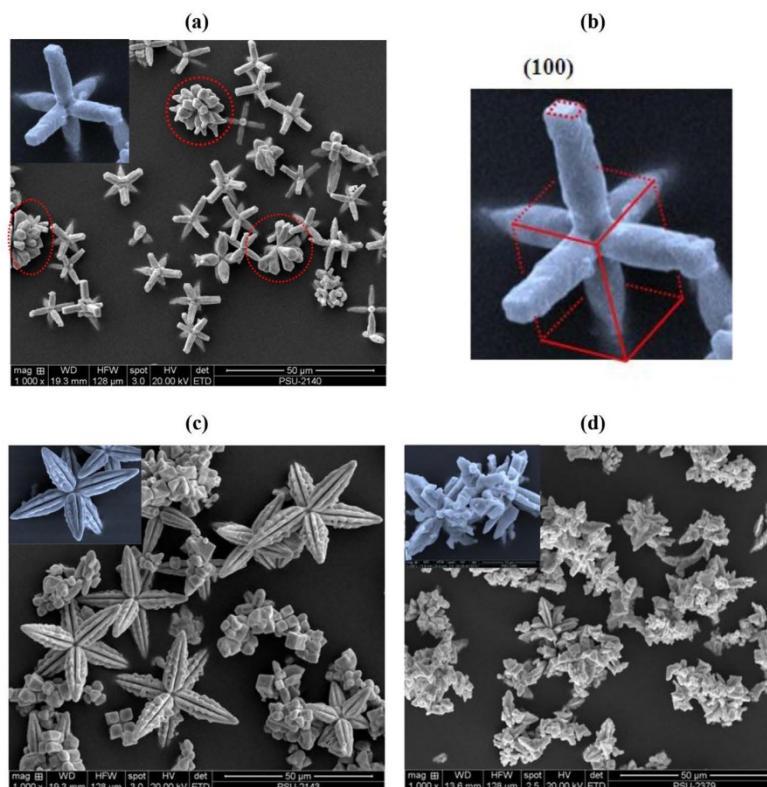In the second experiment, 10 mL of VAM and 80 mL of 13.07 M

Fig. 9. SEM images of the AgCl samples prepared with different concentrations of CH₃COOH: (a) 4.36 M, (b) enlarged view of (a) matched with the cubic crystal plane, (c) 13.07 M, and (d) 16.34 M.

CH₃COOH solution were used to yield hexapods with dagger-like pods with a mean diameter of 7 μm and a length of 21 μm as shown in Fig. 9c. In addition, a small amount of the Rubik's cube-shapes coexisted with these hexapods. When the CH₃COOH concentration was increased to 16.34 M, the morphology of the products changed remarkably. As shown in Fig. 9d, these hexapod microstructures began to grow in almost every direction and the state of being highly ordered and controllable shape was lost. More dagger-like shapes appeared at the expense of the microflowers. Clearly, this condition led to the collapse and breaking apart of the flower-like microstructures.

3.8. The role of the vinyl acetate monomer

Having kept the VAM constant in the above section, in this section the VAM was varied while the CH₃COOH content was constant. The amount of CH₃COOH was fixed at 80 mL of 8.72 M concentration, whereas the VAM was reduced to 5 mL. The morphology still appeared as a flower-like octapod with a crystal size of about 9 μm as shown in Fig. 10a (also compare to Fig. 3). In this morphology, the eight petals inevitably grew out from the eight corners of the cubic form along the <111> directions. To the best of our knowledge, this morphology has never been found in AgCl or any other materials. Increasing the amount of VAM to 15 mL led to the formation of hexapods with large {100} facets of square pods

and an average pod length of *ca.* 6 μm and a width of 2.5 μm, as shown in Fig 10b. Each pod has a square top facet (Fig. 10c) that shows the expected growth habit of the six cubic {100} facets of the cubic seed. This hexapod was very similar to — but the pod length and width were longer and larger than — those in Fig. 9a above.

When 20 mL of VAM was used, the product appeared as the hierarchical flower-like particles with an average size of about 17 μm as shown by the SEM images in Fig. 10d. These flower-like particles displayed a noticeably transformed morphology, as the end of each pod now seemed to be capped with a hollow structure of the zeolite shape.

3.9. Photocatalytic activity

To assess the potential applicability of the as-prepared flower-like Ag/AgCl microstructures in photocatalysis, its photocatalytic activity was investigated and compared with that of the simple Ag/AgCl and commercial Ag/AgCl powders. Orange G (OG) was chosen as the model pollutant dye. The absorption spectra along with the color disappearance are shown in Fig. 11a and b, respectively. Fig. 11c shows the degradation curves of the as-prepared flower-like octapod Ag/AgCl particles, the simple Ag/AgCl, and a commercial Ag/AgCl powder. The latter two Ag/AgCl samples were prepared by the method reported in our previous work [49]. From Fig. 11b and c, one can see that the photodegradation time was
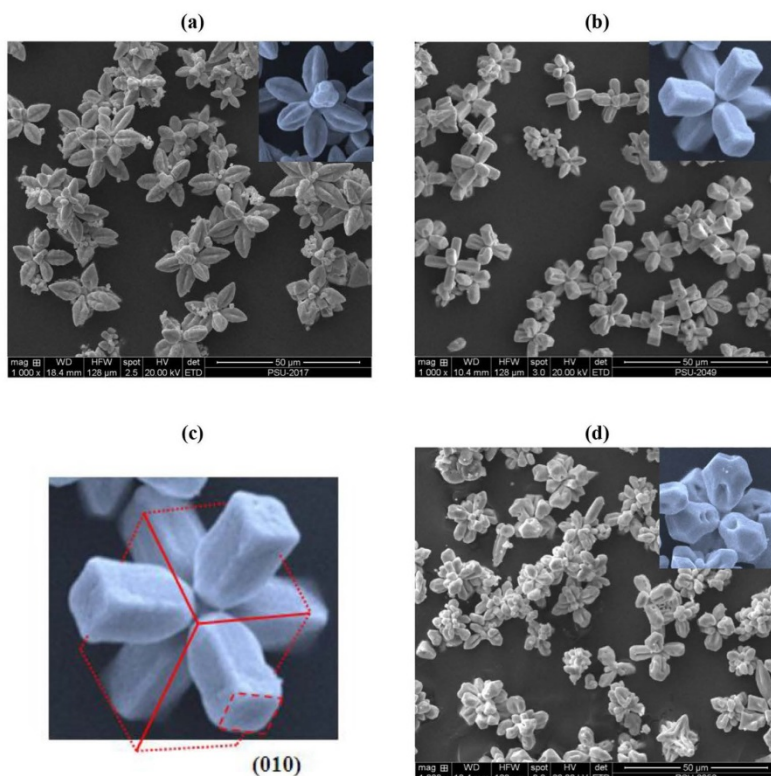
98

Fig. 10. SEM images of the AgCl samples prepared with different VAM additions: (a) 5 mL, (b) 15 mL, (c) enlarged view of (b) matched with cubic crystal plane, and (d) 20 mL.

about 180 min to reduce the colored solution to colorless. The flower-like Ag/AgCl samples, clearly, possessed a higher photocatalytic activity than that of both the simple and commercial Ag/AgCl powders in the order: flower-like Ag/AgCl > simple Ag/AgCl > commercial Ag/AgCl. The superior photodegradation property of the flower-like Ag/AgCl particles relative to the simple and commercial Ag/AgCl powders might be attributed to its larger reactive area that originated from the highly active facets having a large number of atomic steps, edges, and kinks [50]. Fig. 11d shows the linear relationship of $ln\ C_0/C$ *vs. time* and indicated that the photocatalytic degradation of OG followed pseudo-first-order kinetics. In the equation, $ln\ C_0/C = kt$, C is the concentration of the OG, C_0 the concentration of the OG at the beginning of the photocatalytic reaction, t the reaction time, and k the pseudo-first-rate constant [45]. The rate constant k of the flower-like Ag/AgCl was determined to be 2.06×10^{-2} min^{-1}, which was almost four times and ten times higher than those of the simple Ag/AgCl $(6.00 \times 10^{-3}$ min$^{-1})$ and commercial Ag/AgCl $(2.60 \times 10^{-3}$ min$^{-1})$, respectively. This result showed that the flower-like Ag/AgCl was another high-performance photocatalyst for the degradation of the OG dye under visible light irradiation. Recently, we published our work on another form of Ag/AgCl, the urchin-like Ag/AgCl, and showed that it had a higher photocatalytic activity than P25 TiO$_2$ [49]. The activity of the flower-like Ag/AgCl in this paper is on par with the urchin-like Ag/AgCl with respect to the decomposition of OG under visible light. (The k value of the urchin-like Ag/AgCl was

1.90×10^{-2} min^{-1} with the same dye, as it was not provided in Ref [49].) The presence of metallic Ag in Ag/AgCl helped to generate electron–hole pairs efficiently with its SPR capability and supplied the free electrons to the AgCl conduction band. So the photocatalytic ability of the catalyst was enhanced with the increasing plasmonic absorbance of Ag^0 in addition to maintaining its stable photocatalytic activity [51].

To the best of our knowledge, Ag/AgCl has never been used to photodegrade the OG dye, however, at least four reports were found to use AgCl or Ag/AgCl to degrade methyl orange using visible light from a filtered Xe lamp. Morphologies were also different from this work, they were: core–shell Ag/AgCl, heart-like Ag/AgCl, concave cubic AgCl, and hierarchical AgCl [19,20,22,23]. Photodegradation of the OG dye with other catalysts, therefore, were compiled in Table 2 for comparison. From Table 2, two chemical methods worked slightly faster than they did under UV light while the biological methods used required much longer times.

During the photodegradation experiments, the flower-like octapod Ag/AgCl catalyst remained stable and well dispersed throughout the reaction media and were recovered easily at the end of the reaction. The recovered catalyst powder was washed with DI water and dried at 40 °C for about 6 h Fig. 11e shows the use of the recycled catalyst for up to 4 cycles. The efficiency of the catalyst decreased noticeably in the 3rd and 4th reuses.
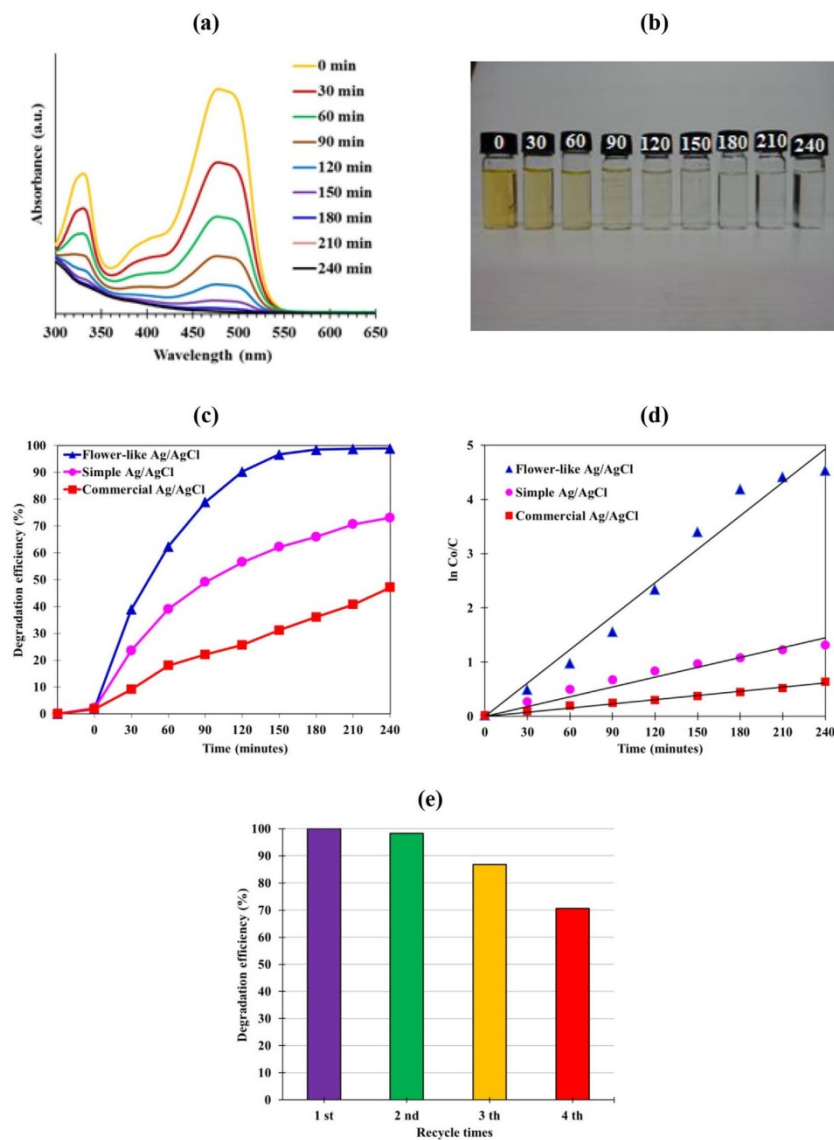
Fig. 11. (a) Time-dependent UV–vis absorbance spectra of the OG solution in the presence of the flower-like Ag/AgCl, (b) color changes of the dye, (c) comparative photodegradation efficiency, (d) pseudo-first order kinetics plots, and (e) recycle test. (For interpretation of the references to colour in this figure legend, the reader is referred to the web version of this article.)

4. Conclusions

In summary, by means of the proper control of the reaction conditions and with the use of VAM, we have successfully prepared AgCl microflowers with evidence that they grew directly from the Rubik's cube structures. Results revealed that the relative growth rate in the <111> direction compared to that in the <110> direction was responsible for the obtained morphologies. The temperature and amount of the reactants played an important role in the formation of the different morphologies of the AgCl microcrystals. VAM proved to be one of the more interesting reagents for the synthesis in controlling the morphology. In this work, we used VAM for such a purpose instead of similar reagents such as polyvinyl pyrolidone (PVP) [20,30,39] and polyvinyl alcohol (PVA) [42]. The flower-like Ag/AgCl microcrystals had a strong visible light absorption *ca.* 500 nm and 600 nm that was useful for applications in

Table 2
Comparison of the photodegradation of the OG dye by different photocatalysts.

Catalysts	Method or light source	Time of decolorization (%)	Refs.
Flowerlike Ag/AgCl	Visible	180 min	This work
TiO_2/H_2O_2	UV	180 min	[52]
Anatase TiO_2	UV	130 min	[53]
Fe(III)-Oxalate Complex	UV	150 min (40%)	[54]
$ZnO/ZnCr_2O_4$	Visible	180 min	[55]
$S_2O_8^{2-}/Fe^{2+}/EDTA$	Microbial fuel cell	12 h	[56]
ZnO doped Dy_2O_3	UV	~200 min	[57]
Bacillus fusiformis KMK5	Biodegradation	36 h	[58]

photodegradation. The presence of the metallic Ag nanoparticles helped to reduce the time for recombination of the electron–hole pairs and, in conjunction with its own SPR property, gave rise to the observed enhancement in their photocatalytic activity.

Appendix A. Supplementary data

Supplementary data related to this article can be found at http://dx.doi.org/10.1016/j.matchemphys.2015.03.054.

References

[1] M.A. El-Sayed, Acc. Chem. Res. 34 (2001) 257–264.
[2] P.V. Kamat, J. Phys. Chem. B 106 (2002) 7729–7744.
[3] S.L. Westcott, S.J. Oldenburg, T.R. Lee, N. Halas, J. Chem. Phys. Lett. 300 (1999) 651–655.
[4] B. Lim, M. Jiang, J. Tao, P.H.C. Camargo, Y. Zhu, Y. Xia, Adv. Funct. Mater. 19 (2009) 189–200.
[5] B. Lim, Y. Xia, Angew. Chem. Int. Ed. 50 (2011) 76–85.
[6] X. Dong, X. Ji, H. Wu, L. Zhao, J. Li, W. Yang, J. Phys. Chem. C 113 (2009) 6573–6576.
[7] X. Luo, Z. Li, C. Yuan, Y. Chen, Mater. Chem. Phys. 128 (2011) 77–82.
[8] W. Niu, Z.-Y. Li, L. Shi, X. Liu, H. Li, S. Han, J. Chen, G. Xu, Cryst. Growth Des. 8 (2008) 4440–4444.
[9] N.R. Jana, L. Gearheart, C.J. Murphy, J. Phys. Chem. B 105 (2001) 4065–4067.
[10] F. Hao, C.L. Nehl, J.H. Hafner, P. Nordlander, Nano Lett. 7 (2007) 729–732.
[11] Y. Xia, Y. Xiong, B. Lim, S.E. Skrabalak, Angew. Chem. Int. Ed. 48 (2009) 60–103.
[12] R. Das, D. Chakdar, G. Gope, S.S. Nath, R. Bhattacharjee, Assam Univ. J. Sci. Technol.: Phys. Sci. Technol. 5 (2010) 123–125.
[13] G. Maduraiveeran, V. Tamilmani, R. Ramaraj, Curr. Sci. India 100 (2011) 199–204.
[14] T.K. Sau, A.L. Rogach, F. Jackel, T.A. Klar, J. Feldmann, Adv. Mater. 22 (2010) 1805–1825.
[15] H.R. Rajabi, O. Khani, M. Shamsipurc, V. Vatanpour, J. Hazard. Mater. 250–251 (2013) 370–378.
[16] M. Shamsipur, H.R. Rajabi, O. Khani, Mat. Sci. Semicond. Process. 16 (2013) 1154–1161.
[17] Q. Zhang, J. Ge, T. Pham, J. Goebl, Y. Hu, Z. Lu, Y. Yin, Angew. Chem. Int. Ed. 48 (2009) 3516–3519.
[18] A. Tao, P. Sinsermsuksakul, P. Yang, Angew. Chem. Int. Ed. 45 (2006) 4597–4601.
[19] Y. Bi, J. Ye, Chem. Commun. (2009) 6551–6553.
[20] J. Liao, K. Zhang, L. Wang, W. Wang, Y. Wang, J. Xiao, L. Yu, Mater. Lett. 83 (2012) 136–139.
[21] H. Chen, L. Xiao, J. Huang, Mater. Res. Bull. 57 (2014) 35–40.
[22] Z. Lou, B. Huang, X. Qin, X. Zhang, H. Cheng, Y. Liu, S. Wang, S.J. Wang, Y. Dai, Chem. Commun. 48 (2012) 3488–3490.
[23] Z. Lou, B. Huang, X. Ma, X. Zhang, X. Qin, Z. Wang, Y. Dai, Y. Liu, Chem. Eur. J. 18 (2012) 16090–16096.
[24] M. Li, H. Yu, R. Huang, F. Bai, M. Trevor, D. Song, B. Jiang, Y. Li, Nanoscale Res. Lett. 8 (2013) 442, http://dx.doi.org/10.1186/1556-276X-8-442.
[25] L.-M. Lyu, W.-C. Wang, M.H. Huang, Chem. Eur. J. 16 (2010) 14167–14174.
[26] Y.-H. Won, L.A. Stanciu, Sensors 12 (2012) 13019–13033.
[27] O.V. Kharissova, B.I. Kharisov, Ind. Eng. Chem. Res. 49 (2010) 11142–11169.
[28] Y. Chang, H.C. Zeng, Cryst. Growth Des. 4 (2004) 273–278.
[29] Z.L. Wang, J. Phys. Chem. B 104 (2000) 1153–1175.
[30] D. Chen, M. Liu, Q. Chen, L. Ge, B. Fan, H. Wang, H. Lu, D. Yang, R. Zhang, Q. Yan, G. Shao, J. Sun, L. Gao, Appl. Catal. B 144 (2014) 394–407.
[31] L. Ai, C. Zhang, J. Jiang, Appl. Catal. B 142–143 (2013) 744–751.
[32] W. Zhou, X. Liu, J. Cui, D. Liu, J. Li, H. Jiang, J. Wang, H. Liu, Cryst. Eng. Comm. 13 (2011) 4557–4563.
[33] M. Zhu, P. Chen, W. Ma, B. Lei, M. Liu, ACS Appl. Mater. Interfaces 4 (2012) 6386–6392.
[34] H. Wang, J. Gao, T. Guo, R. Wang, L. Guo, Y. Liu, J. Li, Chem. Comm. 48 (2012) 275–277.
[35] H. Zhang, M. Jin, Y. Xia, Angew. Chem. Int. Ed. 51 (2012) 7656–7673.
[36] T.T. Tran, X.J. Lu, Phys. Chem. C 115 (2011) 3638–3645.
[37] J. Shu, Z. Wang, G. Xia, Y. Zheng, L. Yang, W. Zhang, Chem. Eng. J. 252 (2014) 374–381.
[38] R. Dong, B. Tian, C. Zeng, T. Li, T. Wang, J. Zhang, J. Phys. Chem. C 117 (2013) 213–220.
[39] D. Chen, S.H. Yoo, Q. Huang, G. Ali, S.O. Cho, Chem. Eur. J. 18 (2012) 5192–5200.
[40] H. Xu, H. Li, J. Xia, S. Yin, Z. Luo, L. Liu, L. Xu, Appl. Mater. Interfaces 3 (2011) 22–29.
[41] S. Linic, P. Christopher, D.B. Ingram, Nat. Mater. 10 (2011) 911–921.
[42] M. Choi, K.-H. Shin, J.J. Jang, Colloid Interf. Sci. 341 (2010) 83–87.
[43] J. Wang, H. Zhao, X. Liu, X. Li, P. Xu, X. Han, Catal. Commun. 10 (2009) 1052–1056.
[44] K. Matsubara, T. Tatsuma, Adv. Mater. 19 (2007) 2802–2806.
[45] Q. Liang, Y. Shi, W. Ma, Z. Li, X. Yang, Appl. Catal. A 455 (2013) 199–205.
[46] J. Hu, N. Jia, J.-X. Jiang, M.-G. Ma, J.-F. Zhu, R.-C. Sun, J.-Z. Li, Mater. Lett. 65 (2011) 1531–1534.
[47] P. Wang, T. Ming, G. Wang, X. Wang, H. Yu, J. Yu, J. Mol. Catal. A: Chem. 381 (2014) 114–119.
[48] H. Gatemala, C. Thammacharoen, S. Ekgasit, Cryst. Eng. Comm. (2014), http://dx.doi.org/10.1039/c4ce00639a.
[49] H. Daupor, S. Wongnawa, Appl. Catal. A 473 (2014) 59–69.
[50] Z. Lou, B. Huang, P. Wang, Z.W. Xiaoyan, Q. Xiaoyang, Z. Hefeng, C.Z. Zhenga, Y. Dai, Dalton Trans. 40 (2011) 4104–4110.
[51] J. Tian, R. Liu, G. Wang, Y. Xu, X. Wang, H. Yu, Appl. Surf. Sci. (2014) http://dx.doi.org/10.1016/j.apsusc.2014.04.178.
[52] N. Divya, A. Bansal, A.K. Jana, Int. J. Biol. Chem. Sci. 3 (2009) 54–62.
[53] A.R. Khataeea, M.R. Pons, O. Zahraa, J. Hazard. Mater. 168 (2009) 451–457.
[54] X. Ou, F. Zhang, C. Wang, C. Wuyunna, Asian J. Chem. 24 (2012) 3314–3318.
[55] G. Thennarasu, A. Sivasamy, J. Chem. Technol. Biotechnol. (2014), http://dx.doi.org/10.1002/jctb.4343.
[56] C.-G. Niu, Y. Wang, X.-G. Zhang, X.-M. Zeng, D.-W. Huang, M. Ruan, X.-W. Li, Bioresour. Technol. 126 (2012) 101–106.
[57] G.A. Suganya Josephine, A. Sivasamy, Environ. Sci. Technol. Lett. 1 (2014) 172–178.
[58] Y.M. Kolekar, S.P. Pawar, K.R. Gawai, P.D. Lokhande, Y.S. Shouche, K.M. Kodam, Bioresour. Technol. 99 (2008) 8999–9003.

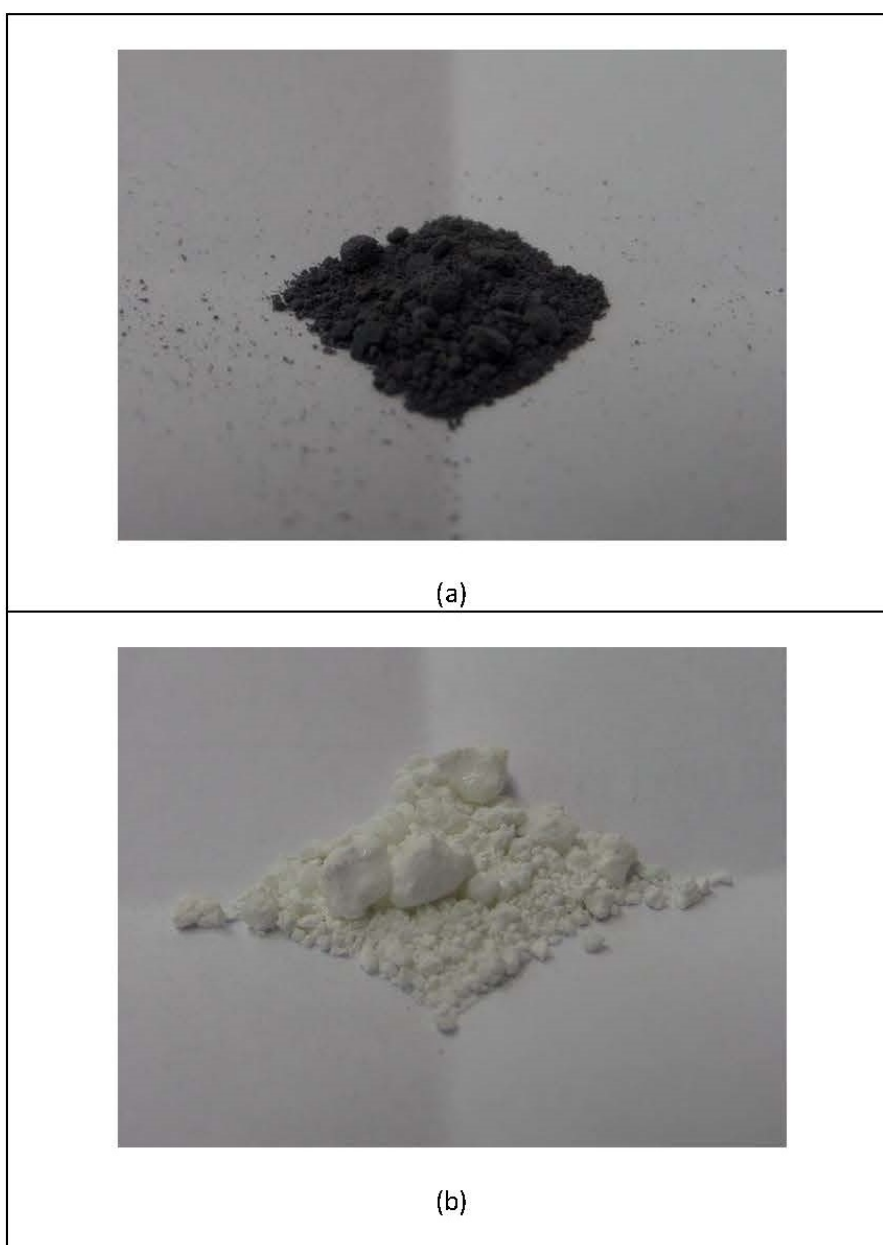# Color of flower-like octapod Ag/AgCl microcrystals

(a)

(b)

Fig. S1 (a) Flower-like octapod Ag/AgCl, (b) commercial AgCl

VITAE

Name	Mr. Hasan Daupor
Student ID	5110230042

Education Attainment

Degree	Name of institution	Year of Graduation
B. Sc. (Chemistry)	Yala Rajabhat University	2006

Scholarship Awards during Enrolment

1. The Strategic Scholarships for Frontier Research Network for the Ph.D. Program Thai Doctoral degree, Office of the Higher Education Commission, Thailand

2. The Center of Excellence for Innovation in Chemistry (PERCH-CIC), Office of the Higher Education Commission, Ministry of Education

3. The Thesis Research Fund through the Graduate School, Prince of Songkla University

List of Publications and Proceedings

Publications

1. **Hasan Daupor** and Sumpun Wongnawa, "Urchinlike Ag/AgCl photocatalyst: Synthesis, characterization, and activity" *Applied Catalysis A: General*, 473 (2014) **59–69**.

2. **Hasan Daupor** and Sumpun Wongnawa, "Flower-like Ag/AgCl microcrystals: Synthesis and photocatalytic activity" *Materials Chemistry and Physics*, xxx, (2015) **1-12**.

3. **Hasan Daupor** and Sumpun Wongnawa, "*Ag/AgCl photocatalytic activity on orange G dye under visible light irradiation*" Pure and Applied Chemistry International Conference (PACCON 2014), Centara Hotel and Convention Centre, Khon Kean, Thailand, January 8–10, 2014, 393–396. (Proceeding)

4. **Hasan Daupor** and Sumpun Wongnawa, "*Metal ion doped TiO$_2$: preparation, characterization and photocatalytic study*" The Sixth Thailand Material Science and Technology Conference (MSAT 6), Miracle Grand Convention Hotel, Bangkok, Thailand, August 26–27, 2010, 298–300. (Proceeding)

Presentation

Oral presentation

1. **Hasan Daupor** and Sumpun Wongnawa, "*Synthesis of AgCl nanoparticles and photodegradation of dyes*" The International Congress for Innovation in Chemistry (PERCH-CIC Congress VIII), Jomtien Palm Beach Hotel and Resort, Chon Buri, Thailand, May 4–7, 2013.

2. **Hasan Daupor** and Sumpun Wongnawa, "*Near spherical AgCl synthesis and photodegradation of dyes*" The Commission on Higher Education Congress V: University Staff Development Consortium (CHE–USDC congress V), Ambassador City Jomtien Hotel, Chon Buri, Thailand, November 14–16, 2012.

Poster presentation

1. **Hasan Daupor** and Sumpun Wongnawa, "*Photocatalytic degradation of dye using Ag-TiO$_2$ catalyst*" The International Congress for Innovation in Chemistry (PERCH-CIC Congress VII), Jomtien Palm Beach Hotel and Resort, Chon Buri, Thailand, May 4–7, 2011.